

AD-A271 034



12

2
DTIC
ELECTE
OCT 20 1993
S A D

**RADAR BACKSCATTER MEASUREMENTS
FROM SIMULATED SEA ICE
DURING CRRELEX'90**

S. G. Beaven, S. P. Gogineni

Radar Systems and Remote Sensing Laboratory
Department of Electrical Engineering and Computer Science, University of Kansas
2291 Irving Hill Road, Lawrence, Kansas 66045-2969
TEL: 913/864-4835 * FAX: 913/864-7789 * OMNET: KANSAS.U.RSL

A. Gow, A. Lohanick

U. S. Army Cold Regions Research and Engineering Laboratory
72 Lyme Road, Hanover NH 03755-1290 TEL 603/646-4256

K. Jezek

Byrd Polar Research Center, 108 Scott Hall, The Ohio State University
1090 Carmack Road, Columbus OH 43210-1002 TEL 614/292-7973

June 1993

This document has been approved
for public release and sale; its
distribution is unlimited

RSL Technical Report 8243-2

Sponsored by:

Office of Naval Research, Arlington VA 22217-5000
Grant N00014-89-J-1456

93-24354



93 1015 078

Table of Contents

0. Sea Ice Remote Sensing	5
1. The 1990 US Army Cold Regions Research and Engineering Laboratory Experiment (CRRELEX '90)	9
2. Step-Frequency Radar Systems Description	13
3. CRRELEX '90 Experiment Description	21
3.1 Radar backscatter measurements	22
3.2 In-situ snow and ice measurements	23
4. Vector Calibration and Measurements of Radar Backscatter	35
4.1 Step-frequency radar principles	35
4.2 Complex vector calibration technique	36
4.3 Implementation of the complex vector calibration algorithm	40
4.4 Narrow-beam approximation to σ^0	45
4.5 Beamwidth correction	46
5. CRRELEX '90 Results	49
5.1 Calibration target results	49
5.2 Polarimetric responses	53
5.3 Polarimetric responses for the calibration targets	54
5.4 Simulated sea ice results	65
6. Comparison of Backscatter Measurements from Simulated Sea Ice to Rough Surface Scattering Theory	69
6.1 Random rough surface scattering	69
6.2 Small perturbation method	72
6.3 Cross-polarization calculations with second-order small perturbation method	74

6.4 Comparisons of measurements with theory	69
7. CRRELEX '90 Conclusions	75
7.1 Conclusions	85
7.2 Limitations and Constraints	86
8. References	89
Appendix A: Scalar-calibrated results without beamwidth correction....	95
Appendix B: Vector-calibrated results without beamwidth correction...	105
Appendix C: Scalar-calibrated results with beamwidth correction.....	115
Appendix D: Vector-calibrated results with beamwidth correction.....	125

Accession For	
NTIS CRA&I	<input checked="" type="checkbox"/>
DTIC TAB	<input type="checkbox"/>
Unannounced	<input type="checkbox"/>
Justification:	
By A 261843	
Distribution /	
Availability Codes	
Dist	Avail and/or Special
A-1	

DTIC QUALITY INSPECTED 2

Abstract

Radar backscatter measurements were performed on artificially grown sea ice on an outdoor pond at the US. Army Cold Regions Research and Engineering Laboratory (CRREL) during the 1990 winter season. Measurements of microwave backscatter from simulated sea ice demonstrate that the dominant backscatter mechanism is the surface scatter. Both the co-polarized and cross-polarized measurements compare favorably with the predictions of surface scattering models at two frequencies. The surface parameters used in the models were measured directly from photographs of cross sections of the saline ice. Therefore, since two frequencies of backscatter measurements were predicted accurately by surface scatter models, the predominate backscatter must be from the surface.

These measurements were carefully calibrated using a complex vector error correction scheme to remove polarization coupling and other systematic effects. The dynamic range of polarimetric measurements made by scatterometers is limited by coupling and polarization leakage in the antenna system and RF section. These effects must be accounted for and corrected if one is to obtain accurate characterization of the polarimetric response of distributed targets.

This demonstrates the need for careful calibration in experiments of this type, especially when cross-polarized backscatter measurements are performed. The systematic effects on the cross-polarized backscatter introduce significant error and may lead to misinterpretation of the results. This is a vital consideration in the study of radar backscatter from sea ice using fully polarimetric systems.

0. Sea Ice Remote Sensing

Ice-covered oceans have been the subject of extensive research due to their importance in global climate change and their hindrance to shipping traffic for northern ports. The sea ice extent in the Arctic is extremely dynamic. At its maximum in March the Arctic ocean is covered by about 14.8 million km² of sea ice and the minimum extent is about 7.8 million km² in September [Parkinson, et al., 1987]. The variation in sea ice cover itself is roughly equivalent to an area the size of the 48 contiguous states of the US.

In global climate models the predicted warming of the globe due to increase in greenhouse gases is most dramatic in the polar regions. For example, the high resolution models of the Canadian Climate Centre, the Geophysical Fluids Dynamics Laboratory at Princeton, and the United Kingdom Meteorological Office all show more dramatic temperature changes in the Arctic than for the rest of the world [Houghton, 1990]. While all three models predict a global temperature increase of between 3.5° and 4° C, they predict an increase in the summer temperature in the Arctic of between 6° and 16° C. All three models are equilibrium models based on the instantaneous doubling of carbon dioxide in the atmosphere.

The albedo of the surface of the earth plays an important role in the amount of total energy absorbed by the earth. The albedo feedback effect concerns the amount of incoming solar radiation that is reflected back into space by the earth's surface and atmosphere.

The albedo of the ice affects the amount of short-wave radiation absorbed at the surface. If the extent of sea ice decreases and is replaced by open ocean, which has a lower albedo, there will be more absorption at the earth's surface. This warming will lead to a further retreat of sea ice and an increase in the amount of radiation absorbed. This is effectively a positive feedback effect in a global warming scenario.

In addition to being a possible indicator of climate change, sea ice cover also modulates energy exchange between the warm ocean and the cold atmosphere. Sea ice cover acts as an insulator between them. Different sea ice types may also affect this interaction. Areas of pancake ice, for example, may allow for more energy exchange between the air and ocean than an area containing a multiyear floe.

In addition to the active roles mentioned above sea ice also has been postulated as a measure of the changing climate. Both the extent of sea ice over a period of time and its thickness may be a signal of the onset of global climate change, much like the amount of CO₂ in the atmosphere and surface temperatures are pointed to today as indicators of global warming.

Because of these effects it is essential in studying our planet that sea ice is monitored on a global scale. The only way to achieve this is by looking at the earth's surface by remote sensing from satellites. The primary problem in the Arctic regions for other remote sensing techniques (visible, optical, infrared) is that the polar regions are dark for half of the year. In the other half of the year cloud cover and fog reduce the effectiveness of these techniques. The only methods for consistently monitoring the Arctic through darkness, fog and cloud are by active and passive microwave remote sensing. Of these two methods, the active microwave remote sensors, usually

Synthetic Aperture Radar (SAR), have much better spatial resolution. Therefore SAR is more capable of monitoring finer structure and sea ice dynamics than passive microwave devices.

Because of the importance of sea ice in the global climate and in its impediment to ship traffic in the Arctic, and the capability of active microwave sensors to characterize sea ice, the radar backscatter signatures of sea ice have been of intense interest over the last two decades.

This report concentrates on the understanding of the backscatter mechanisms for simulated sea ice. The emphasis of the simulated sea ice work is to produce high quality measurements to be used in the validation of scattering models for use in the study of sea ice. The measurements for this study were taken at the US Army Cold Regions Research and Engineering Laboratory (CRREL) during the Winter of 1990. The results of this study show that the backscatter coefficient is dominated by surface scatter.

1. The 1990 US Army Cold Regions Research and Engineering Laboratory Experiment (CRRELEX'90)

1.0 Introduction

Controlled radar backscatter measurements were performed by researchers from the University of Kansas Radar Systems and Remote Sensing Laboratory (RSL) at the US Army Cold Regions Research and Engineering Laboratory (CRREL) in early 1990 to investigate the scattering characteristics of sea ice. Measurements were performed at an outdoor saline ice facility using two network analyzer-based stepped-frequency radar systems. These systems were developed at RSL and operated at C band (5.3 GHz) and Ku band (13.4 GHz). These systems allowed for measurement of backscatter in amplitude and phase at four linear polarizations: VV, HH, VH, and HV. Saline ice with varying degrees of roughness was investigated with and without snow cover at angles ranging from 0° to 60°. The CRREL experiments were performed to study the relation of physical properties of simulated sea ice to the measured backscatter under somewhat controlled laboratory conditions. The simulated sea ice grown at the CRREL facility has physical properties which closely model thin Arctic ice grown under quiescent conditions, [Swift, et al., 1992]. The physical properties of simulated sea ice have been shown to closely resemble sea ice found in the Arctic [Arcone, et al., 1986]. Since the ice properties can be monitored closely in this type of situation, the physics of microwave backscatter from saline ice can be studied in greater detail than in field expeditions where there is no control over the environment.

These measurements, like all radar measurements, are limited by the polarization purity of the antenna and RF section as well as coupling between transmit and receive antennas. The accuracy of cross-polarized measurements is especially vulnerable to these systematic effects imposed by the radar system. Recently, emphasis has been placed on utilizing the scattering information from all four linear polarizations in studying the nature of scattering mechanisms [Kwok, et al., 1991], [Drinkwater, et al., 1991]. In particular, the polarization ratio, usually defined as the ratio of co-polarized σ^0 divided by cross-polarized σ^0 , is often used to categorize sea ice. Also the polarization "signature", or more correctly, polarization response, has been used recently in the study of radar backscatter from ice. This requires information from all four linear polarizations, thus the need for accurate cross-polarized measurements. To obtain high quality measurements for comparison with theory, the calibration of the scatterometers must take these effects into account. To accomplish this a complex vector error calibration was performed based on techniques described by [Riegger, et al. 1989], [Wiesbeck and Riegger, 1991], and [Chen, et al., 1991], but applied to returns from a distributed target (artificial sea ice) as opposed to simple targets.

This technique allows one to quantitatively reduce the effects of polarization leakage of the antennas to improve the dynamic range of the scatterometer data. This technique was applied to both C-band and Ku-band data taken during CRRELEX'90. The effectiveness of the technique is verified by applying it to several calibration targets. These results show that the vector calibration leads to at least a 15 dB improvement in the dynamic range of the backscatter measurements. The vector calibration was then applied to returns from artificial sea ice. The resulting measurements of scattering coefficient from saline ice show a much greater difference between co-polarized and cross-polarized returns than for the usual scalar calibration

technique [Ulaby, et al., 1982] in which only a single non-depolarizing target such as the Luneburg lens or metal sphere is used.

After careful calibration to remove system effects, the backscatter measurements were compared to the small perturbation model for scattering from a random rough surface. These results demonstrate that the experimental values correspond fairly closely with the scattering theory. In particular the levels of the cross-polarized measurements are significantly lower than measurements of the cross-polarized backscatter that are not corrected for systematic effects of the radar system. The ratio of like-polarized return to the cross-polarized return also increases when systematic errors are removed.

In this report the results of the scatterometer measurements are presented for both the case before and after the systematic calibration is applied. The details of the calibration technique as well as limitations due to assumptions made and the measurement setup are presented. The vector calibrated results are then compared to rough surface scattering models.

2. Step-Frequency Radar Systems Description

Two stepped-frequency radar systems were used to measure backscatter from an outdoor saline pond at the CRREL facility in Hanover, New Hampshire. The measurements were performed at C band and Ku band with network-analyzer based systems. Each system contains an HP 8753 Network Analyzer as the core. The intermediate frequency (IF) sections for both systems are housed in a single box as are the radio frequency (RF) portions of the system.

The RF sections provided the up-conversion of the network analyzer output from 2 GHz center frequency (IF) to a center frequency of 5.3 GHz for the C-band system and 13.9 GHz for the Ku-band system. They also performed the down-conversion of the received signal to IF for measurement by the network analyzer. Figure 2.1 shows the block diagram for both the C-band and Ku-band systems, with particular emphasis on the RF section. The network analyzer played the role of the signal generator and processor for each radar system. It was used to coherently measure the amplitude and phase of the return signal (i.e. the S_{21} scattering parameter) at IF, for a set of discrete frequencies. The frequency of the network analyzer is stepped through 1000 MHz of bandwidth for the Ku-band radar and 500 MHz of bandwidth for the C-band radar in 2.5 MHz steps. The network analyzer is used to measure the return independently at each frequency and these measurements are stored on disk. Table 2.1 describes the important parameters of the systems used. Photograph 2.1 (a) and (b) show the radar system setup at the lower pond.

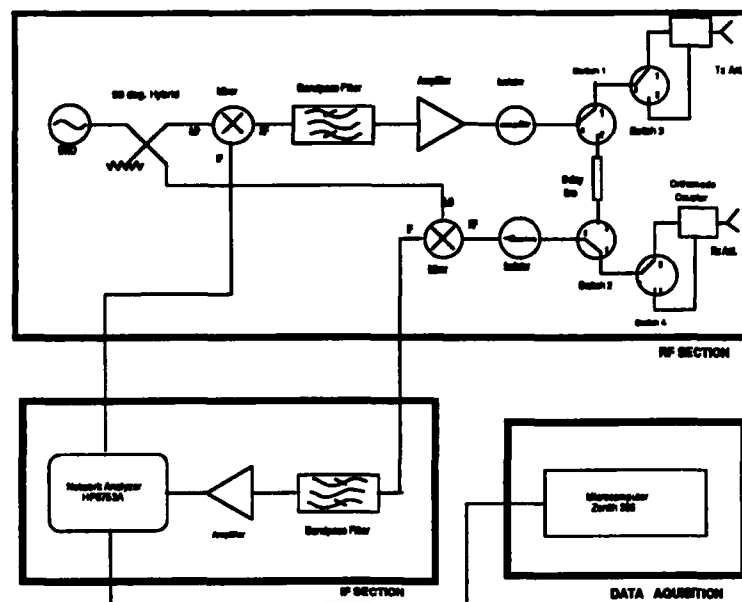


Figure 2.1. Block diagram describing both the C-band and Ku-band step-frequency radar system.

The RF sections of the C-band and Ku-band radar systems are nearly identical and are shown in figure 2.1. The source in the RF section is a dielectric resonator oscillator (DRO). The output of the DRO is mixed with the IF source from the network analyzer to generate the RF radar signal. The frequency of the DRO is set so that the center frequency of the RF signal is at 5.3 GHz for the C-band system and 13.4 GHz for the Ku-band system. This is filtered and amplified before passing through the switching network. The switching network in the RF section guides the signal to either the horizontal or vertical polarization port to the antennas. This allows for both vertical and horizontal polarizations to be transmitted. The backscattered signal is received through the receive antenna. The switching network separates the received signal into either vertical or horizontal polarization. The returned signal is then mixed down to IF for measurement with the network analyzer.

Table 2.1. Step-Frequency Radar System Parameters		
	<u>C band</u>	<u>K_u band</u>
Center Frequency. (GHz)	5.3	13.9
RF Bandwidth (MHz)	500	1000
Free-space Resolution (cm)	30	15
Number of frequency steps	200	400
Footprint in cm (2m range)	48 x 48	30 x 30
Transmit power (mW)	10	10

The horizontal and vertical polarization for the C-band radar system are obtained by using two pyramidal horn antennas for receiving and two for transmitting. The pyramidal horn is also called the standard gain horn since it has a wide beamwidth and its pattern is well-documented [Balanis, 1982]. These antennas provided a 15° two-way equivalent beamwidth as mounted during CRRELEX'90.

At Ku band the vertical and horizontal polarizations are obtained with a single diagonal horn antenna for transmitting and an identical antenna for receiving. The two antenna Ku-band system is obtained through the use of ortho-mode transducers for each of these antennas. The diagonal horn antenna relies on the superposition of the TE₀₁ and TE₁₀ modes. In the diagonal horn these modes generate a field pattern that resembles the TE₁₁ mode of a circular waveguide [Love, 1962]. The far-field patterns that result are shown here in figures 2.2 and 2.3 (taken from Love, 1962).

The principal plane patterns demonstrate that the antenna has superb sidelobe performance as shown in figure 2.2. Ideally, there is no cross-polarized pattern in the principal planes. In the 45° plane the cross-polarized pattern of figure 2.3 is seen to be about 15 dB below the normal antenna pattern near the main lobe in the ideal case. This is important when considering cross-polarized measurements and the effect of finite polarization purity on these measurements.

The network analyzer is controlled by a microcomputer via a Hewlett Packard Interface Bus (HPIB) expansion card. A computer program controls the stepping of the network analyzer through the frequencies needed to produce the bandwidths shown in table 2.1. The program also obtains the scattering coefficient measurement from the network analyzer and is used to store the data to disks. The switching network, which is used to switch between polarizations, was manually controlled by an external control box. The switch network was also used to perform a delay-line measurement as an internal calibration. The network analyzer, switch control box, and computer were housed in a shed adjacent to the lower pond as shown in photograph 2.2.

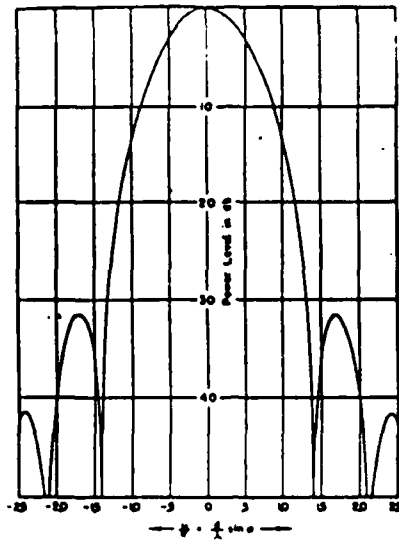


Figure 2.2. Antenna pattern for diagonal horn (from Love, 1962). This shows the principal plane E- and H-plane normalized antenna patterns for an ideal diagonal horn antenna.

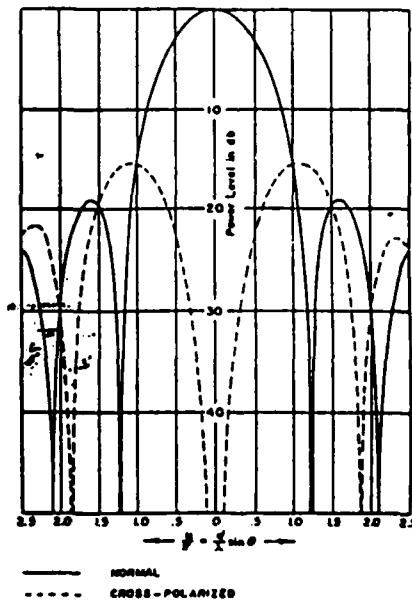
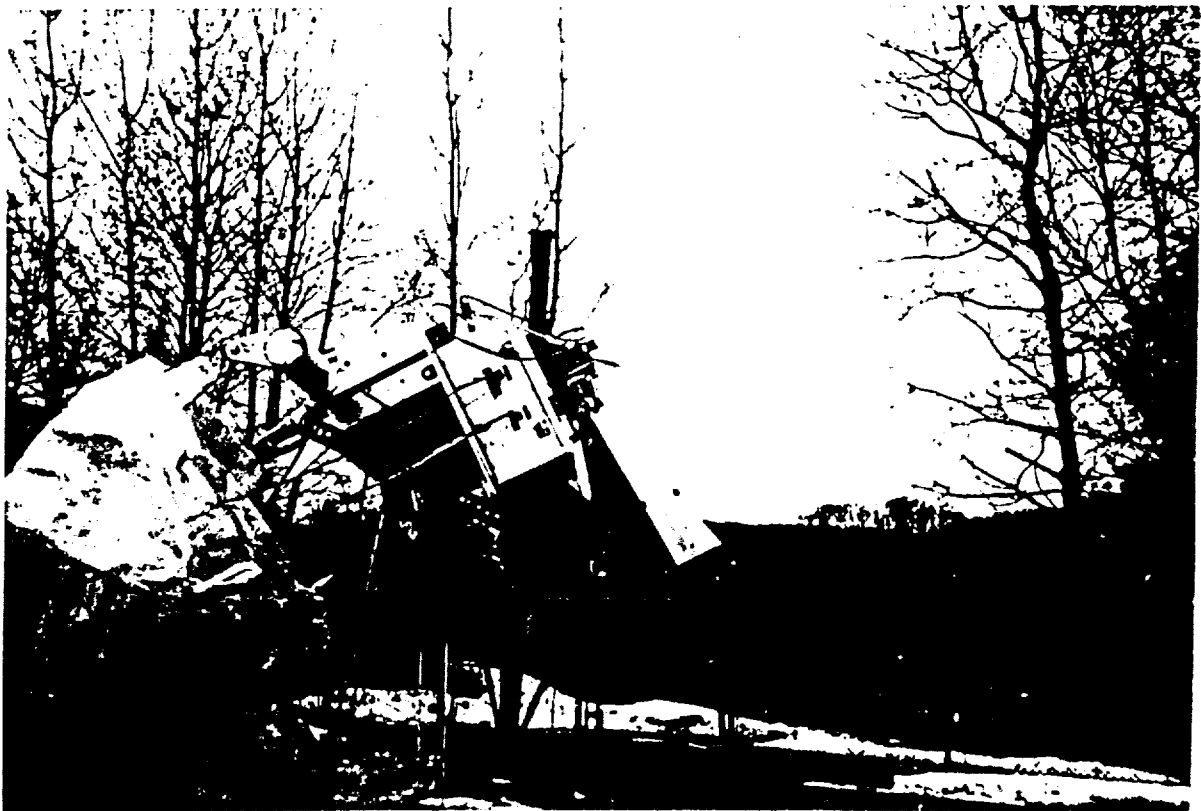
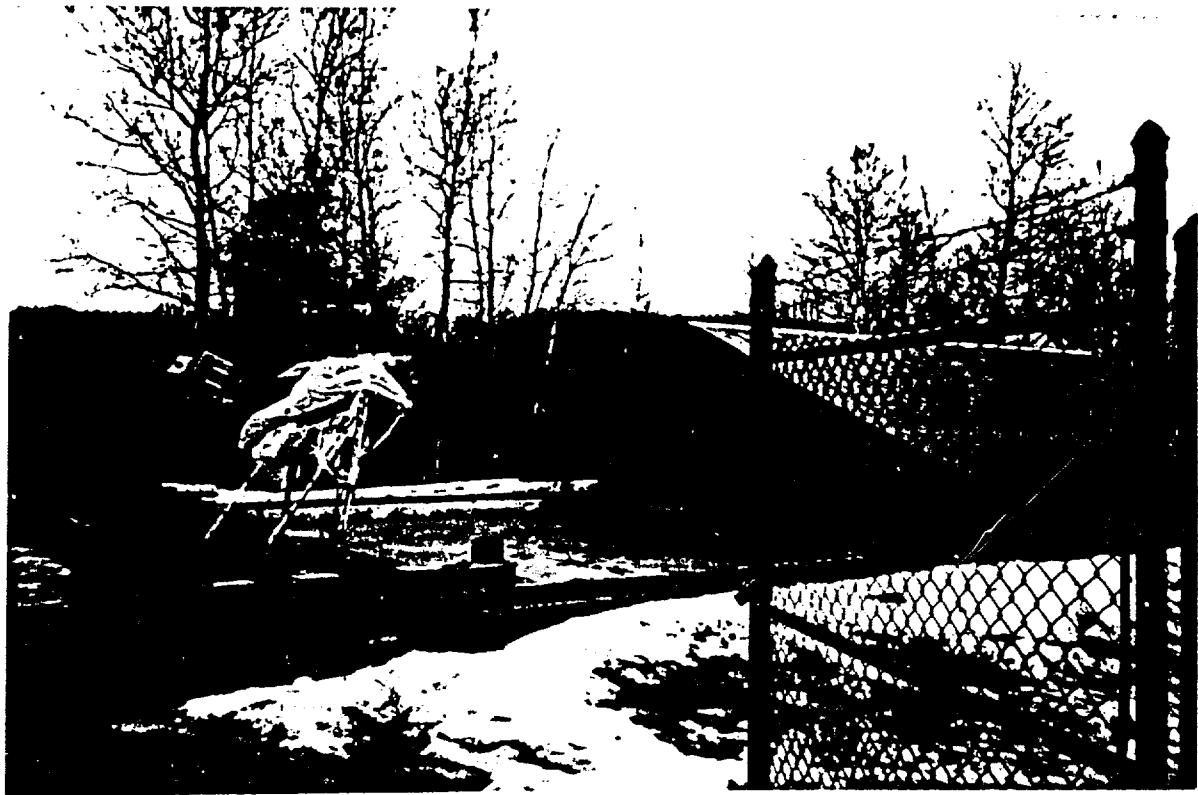


Figure 2.3. Diagonal horn antenna pattern for 45° planes (from Love, 1962). This shows the ideal 45° plane patterns for co-polarized and cross-polarized normalized power. This shows the level of cross-polarized power as being about 15 dB below the normal pattern near the main beam.



Photograph 2.1 (a) Mounting of the C-band and Ku-band step-frequency radar systems at CRREL's lower pond facility for CRRELEX'90. (b) Close-up view of the RF box and antenna mount showing the two diagonal Ku-band horns and the four C-band pyramidal horn antennas.



Photograph 2.2 A network analyzer, control boxes and Compaq computer were housed in a shed adjacent to CRREL's lower pond for the 1990 campaign.

3. CRRELEX'90 Experiment Description

Radar backscatter measurements from artificial sea ice were made at CRREL's lower pond facility during January and March, 1990. The experiment utilized an outdoor frozen pond which was made with saline water in order to simulate sea ice. This facility provides a test bed for experimentation under quasi-laboratory conditions. This allows for more control than expedition-type endeavors. The lower pond is made of concrete and is about 10m x 10m x 1.3 m, with vertical sides. The facility has a walkway on railroad tracks which served as a mobile base on which the antenna mount was placed. The RF sections were also placed on the antenna mounts, while the control and data acquisition systems were housed in a shed adjacent to the pond.

Measurements were made at incident angles ranging from 0° to 60° , with all four linear polarization combinations: VV, HH, VH, and HV. Movement of the antenna mount allowed for up to four independent spots for reduction of fading which occurs in radar backscatter measurements. In addition, ice core samples were collected by CRREL and analyzed to obtain the characteristics of the saline ice. Ice characterization data included measurements of salinity and temperature profiles, ice-structure, including micro structure from thin sections and macro structure (bubble size and surface roughness) from thick sections.

3.1 Radar backscatter measurements

Radar backscatter measurements and ice property measurements were made in January and again in March under a variety of weather conditions. Table 3.1 summarizes the dates, times and angles of which measurements were made, as well as the number of independent spots used.

Table 3.1. CRRELEX'90 Lower Pond Data Summary				
Date	Time (EST)	Incidence Angles	Frequency	Spots
7 Jan	17:00	12 - 55	C, K _U	3
9 Jan	17:44	0 - 55	C, K _U	4
24 Jan	15:44	0 - 40	K _U	2
29 Jan	10:51	47 - 55	K _U	2
5 Mar	13:27	3 - 53	K _U	3
6 Mar	13:33	3 - 53	C	3
8 Mar	21:03	0 - 55	C, K _U	4
10 Mar	13:48	0 - 55	C, K _U	3
11 Mar	04:58	0 - 55	C, K _U	4
14 Mar	04:24	0 - 55	C, K _U	4
28 Mar	06:37	0 - 53	C, K _U	3

In addition to the backscatter measurements from saline ice the return from several calibration targets were measured with the radar systems. These targets included a Luneburg lens, a metal sphere, and a dihedral corner reflector. These measurements were made so that careful calibration could be used to remove the systematic errors due to polarization leakage and other effects which occur when using real antennas.

3.2 In-situ snow and sea ice measurements

During the lower pond experiment of CRRELEX'90 the air and ice temperatures were taken periodically, along with ice surface salinity and snow depth. These are shown in table 3.2. From these parameters an estimate of the surface dielectric constant was made using past measurements from CRREL [Arcone, et al., 1986]. From these an approximate dielectric constant was selected at $3.75 - j0.4$. This is based on the temperature and age of the saline ice sheets.

Table 3.2. In-situ snow and ice information		
Ice or Snow Property		Date / Time
Temperature	-9.5° C : snow surface	17:00 / 7 Jan
	-3.0° C : snow-ice interface	17:00 / 7 Jan
	0° C : Ice Surface	13:48 / 10 Mar
	-1.5° C : Ice Surface	04:58 / 11 Mar
	-1.0° C : Ice Surface	04:24 / 14 Mar
Salinity	12 ‰ ± 2 ‰ at snow / ice interface	9 Jan.
snow depth	58 mm	7 Jan
	57 mm	9 Jan

In addition, photographs were made of sections cut from the saline ice sheet. Any snow, if present, was removed from these sections. These were used to characterize the surface in terms of rms roughness and correlation length for comparison to theoretical models. The photographs used to find the surface parameters for the experiment are shown on the following pages. The first six were taken on 20 January and the last two were taken in the latter portion of the campaign on 11 March.

The procedure for obtaining the surface roughness was performed by digitizing the ice section photographs by scanning into a computer. These were then expanded by a factor of 10 using a graphics routine. From the expanded version, x-axis and y-axis values were read from the image. The spacing between samples was 1 mm and the precision of the height reading was within 1/10 mm, on the expanded images. The standard deviation of the surface height (surface roughness) was calculated from

$$\sigma_h = \sqrt{\frac{1}{N-1} \left(\sum_{i=1}^N z_i^2 - N(\bar{z})^2 \right)}, \quad (3.1)$$

where N is the number of samples in the sequence and \bar{z} is the mean value of the surface height [Ulaby, 1982]. The autocorrelation of the surface height is also needed in scattering models and was obtained from,

$$\rho(x') = \frac{\sum_{i=1}^{N-j} (z_i - \bar{z})(z_{i+1} - \bar{z})}{N}, \quad (3.2)$$

where N is the number of samples, and x' is the spatial displacement defined by the sample number and the spacing as $x' = (j+1)\Delta x$.

The correlation length was obtained from

$$\rho(L_c) = \frac{1}{e}, \quad (3.3)$$

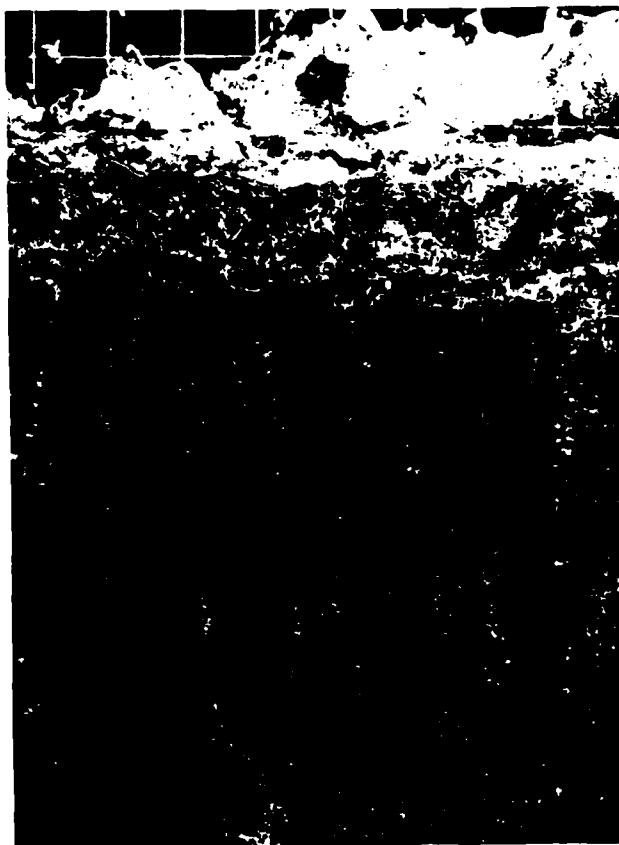
where L_c is the correlation length and as usual,

$$e = \lim_{x \rightarrow \infty} \left(1 + \frac{1}{x}\right)^x \approx 2.718. \quad (3.4)$$

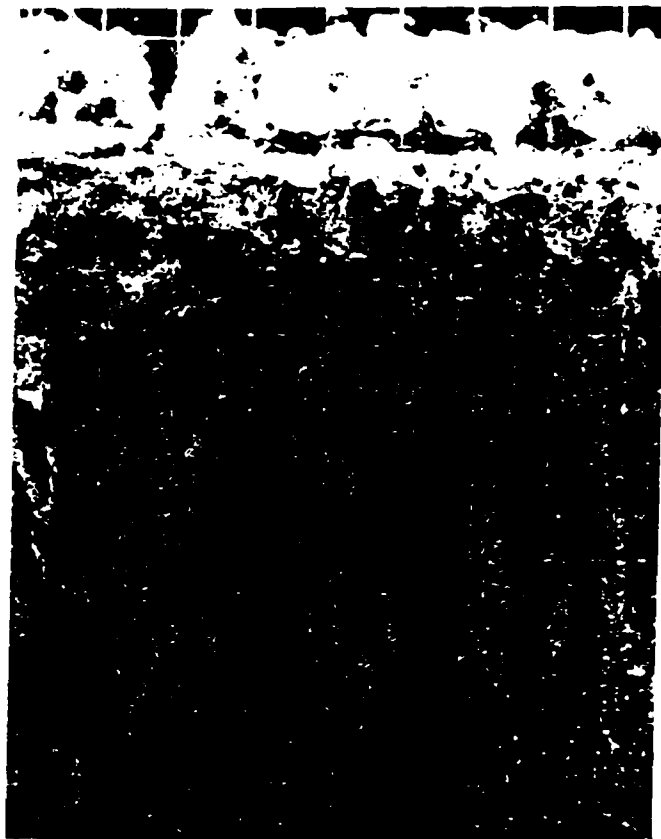
The computed autocorrelations for the slabs taken in the January experiment are shown in figures 3.1, 3.2, and 3.3. Figure 3.1 shows the correlation for slabs 1a and 1b, with slab 1a having a longer correlation length. This is due to the step-like jump in the ice surface, visible in photograph 3.1. The remaining correlations for January are more like that of slab 1a. Figure 3.4 shows the computed autocorrelation for the slabs taken in March. This plot demonstrates the marked increase in the correlation length for the smoother ice observed in the March campaign. Results of the

correlation lengths and the standard deviation of the surface height are shown in table 3.3. The averages for both 20 January and 11 March are used in a later section in surface scattering models for comparison to measured results.

Table 3.3. Results of surface roughness calculations		
Date / slab number	surface roughness (mm)	correlation length (cm)
20 January, slab 1a	4.068	1.15
20 January, slab 1b	2.49	0.29
20 January, slab 2a	1.598	0.25
20 January, slab 2b	1.427	0.28
20 January, slab 3a	1.212	0.37
20 January, slab 3b	2.164	0.5
20 January average	2.16	0.47
11 March, slab 1a	1.209	1.80
11 March, slab 1b	1.502	1.72
11 March average	1.36	1.76



Photograph 3.1. Reflected light photograph of vertical thick section 1a, taken on 20 Jan. from CRREL's lower pond facility. Grid scale measures 1 cm on a side.



Photograph 3.2. Reflected light photograph of vertical thick section 1b, taken on 20 Jan. from CRREL's lower pond facility. Grid scale measures 1 cm on a side.

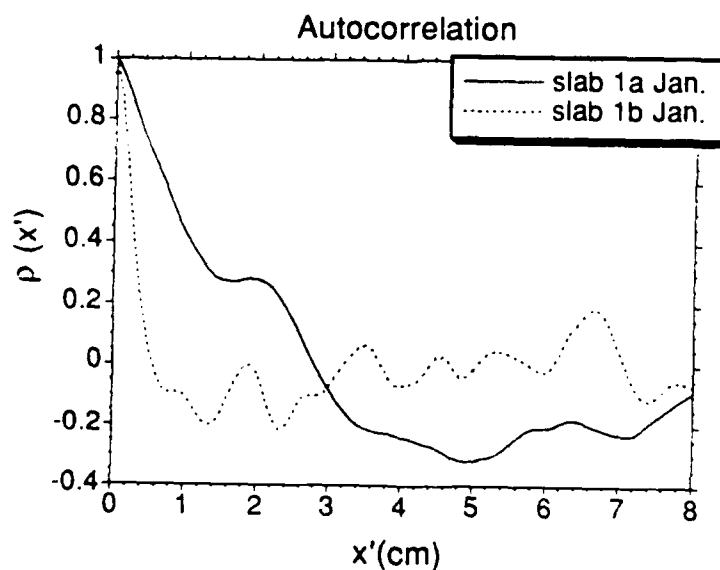
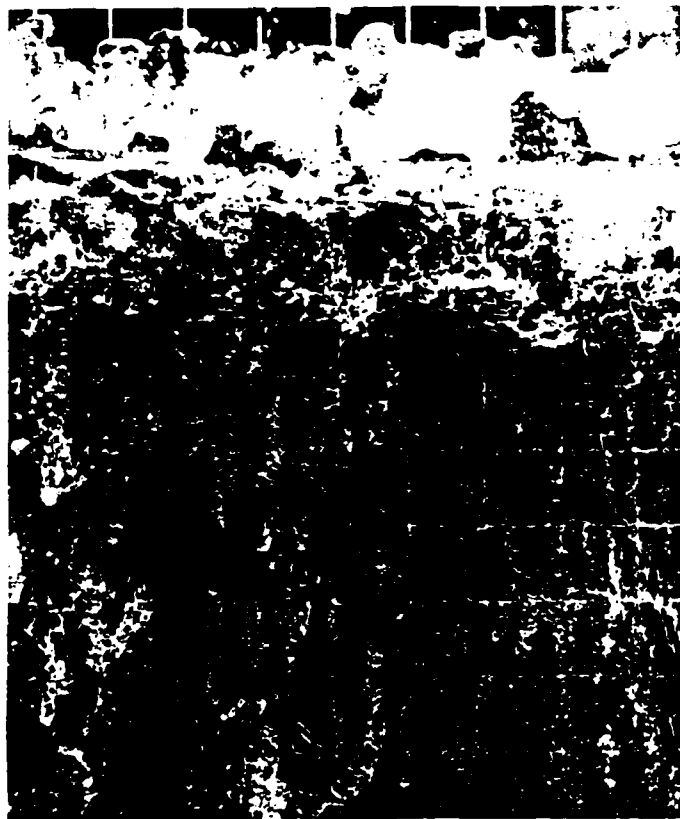
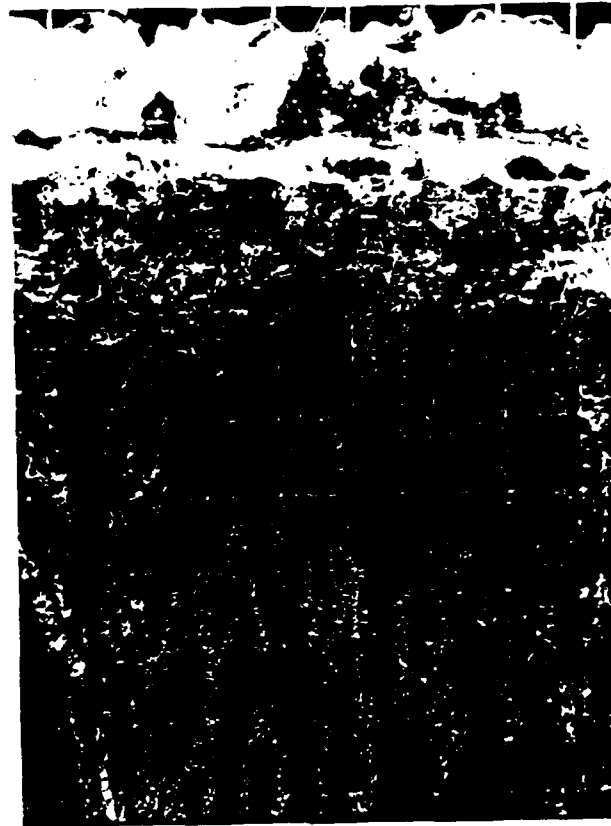


Figure 3.1. Autocorrelation calculations from slab 1a and 1b, characterizing the ice surface for the January CRRELEX'90 campaign.



Photograph 3.3. Reflected light photograph of vertical thick section 2a, taken on 20 Jan. from CRREL's lower pond facility. Grid measures 1 cm on a side.



Photograph 3.4. Reflected light photograph of vertical thick section 2b, taken on 20 Jan. from CRREL's lower pond facility. Grid scale measures 1 cm on a side.

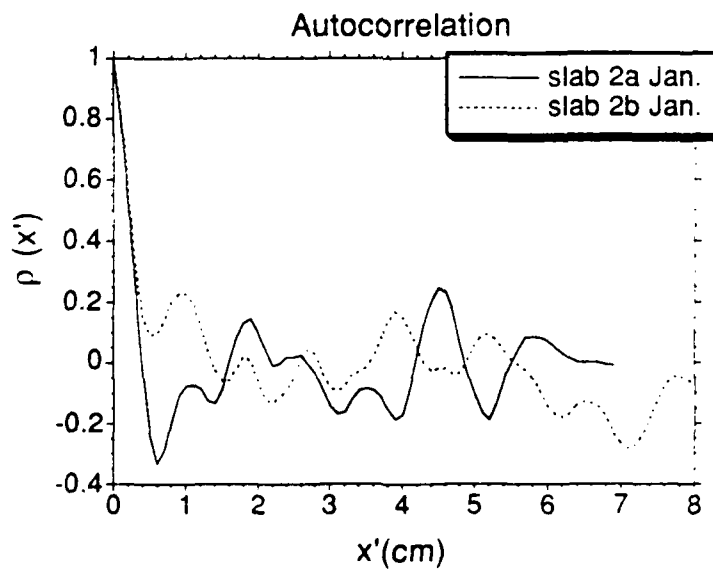
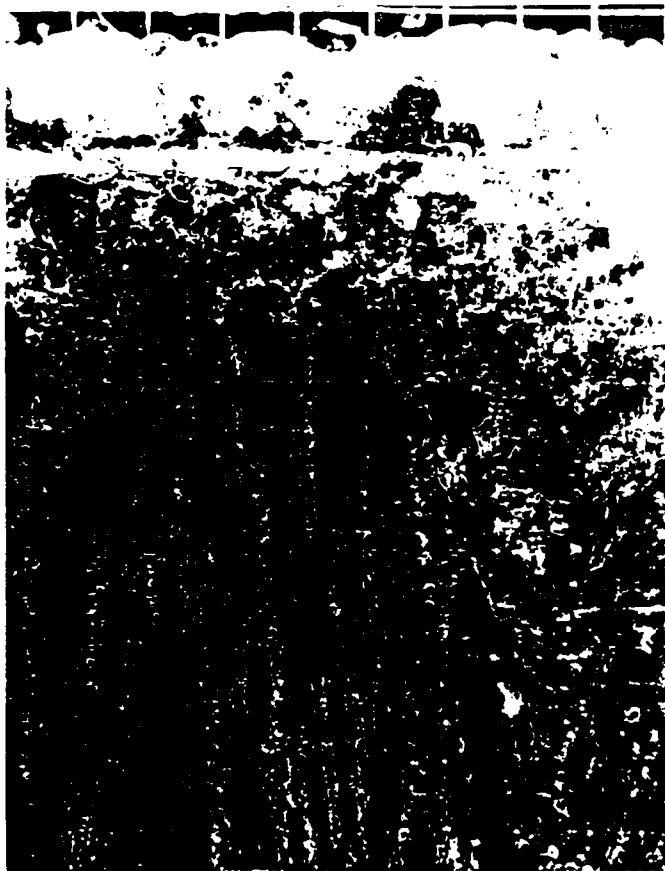


Figure 3.2. Autocorrelation calculations from slabs 2a and 2b, characterizing the ice surface for the January portion of CRRELEX'90.



Photograph 3.5. Reflected light photograph of vertical thick section 3a, taken on 20 Jan. from CRREL's lower pond facility. Grid scale measures 1 cm on a side.



Photograph 3.6. Reflected light photograph of vertical thick section 3b, taken on 20 Jan. from CRREL's lower pond facility. Grid scale measures 1 cm on a side.

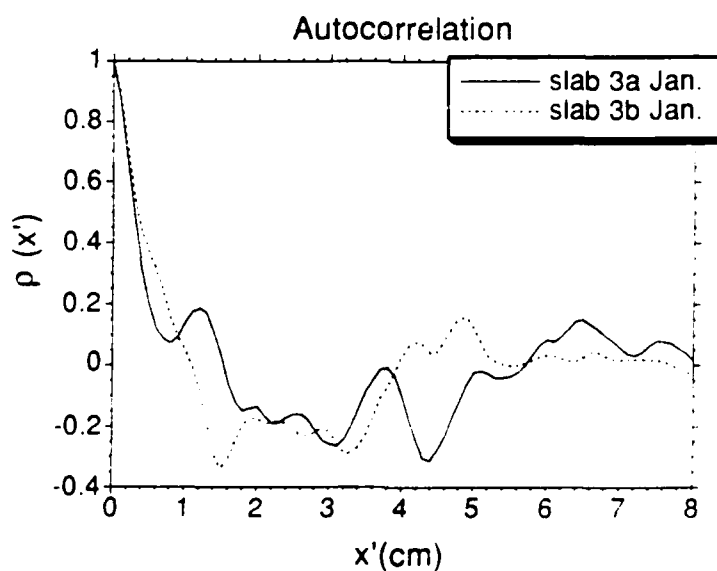


Figure 3.3. Autocorrelation calculations from slabs 3a and 3b, characterizing the ice surface for the January portion of CRRELEX'90.



Photograph 3.7. Reflected light photograph of vertical thick section taken on 11 March from CRREL's lower pond facility. Note the much smoother surface than the January photographs. This is due to melting and re-freezing that occurred between portions of the CRRELEX'90 campaign.



Photograph 3.8. Reflected light photograph of vertical thick section taken on 11 March from CRREL's lower pond facility.

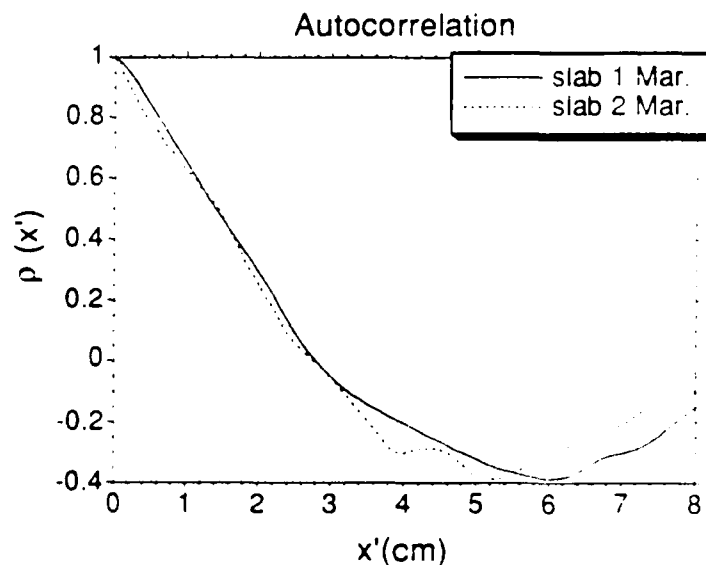


Figure 3.4. Autocorrelation calculations from slabs 1 and 2, characterizing the ice surface for the March portion of CRRELEX'90.

4. Vector Calibration and Measurements of Radar Backscatter

Step-frequency radars were used to measure the scattering coefficient of saline ice. The radars were calibrated using a complex vector calibration technique described in this section. The methods for obtaining the scattering coefficient from a step-frequency radar are described in this section as well as the method for calculating the backscatter coefficient when applying the complex vector calibration.

4.1 Step-frequency radar principles

The step-frequency radar systems described in the previous section were used to measure backscatter from saline ice. The voltage scattering coefficient from a given target can be obtained from the step-frequency radar measurement in the following manner. The amplitude and phase of the continuous-wave (CW) measurement at each of the discrete frequencies used by the radar system are stored on a disk. The complex spectrum (usually FFT) of these data is related to the voltage scattering coefficient, s_k of a target by [Iizuka, et al., 1984]

$$h_k = \frac{Ns_k E_0}{z_k^2} e^{j(\frac{4\pi}{c})(kf_0 \Delta z)}, \quad (4.1)$$

where h_k is the complex spectral component of the measured data at point k , N is the total number of discrete points used over the bandwidth, E_0 is the incident electric field magnitude and z_k is the distance from the radar to the scattering point in question. The phase term is simply an unwrapping due to the propagation of the

incident and reflected wave and is dependent on the specific frequency of the k^{th} measurement ($kf_0/\Delta z$) as well as the velocity (c) of the wave.

To obtain the power returned from a target the magnitude of the voltage scattering coefficients are squared. This is then used in the narrow-beam approximation to the radar equation as the returned power.

4.2 Complex vector calibration technique

The radar return from several calibration targets were used to compute the vector calibration matrix as described here. The targets included a Luneburg lens, a metal sphere, and a dihedral corner reflector. The diplane was chosen so that it could be used as both a depolarizing and a non-depolarizing target, depending on its orientation. The sphere was used for the vector error calibration as a non-depolarizing target. The Luneburg lens was used for absolute (scalar) calibration of the measurements. Absolute calibration was also performed with reference to the sphere instead of the lens as a verification of the Luneburg lens radar cross section value.

The vector calibration technique follows that demonstrated by [Riegger and Weisbeck, 1989] for simple targets. Here the technique is applied to the radar returns from artificial sea ice, a complex distributed target. This vector calibration removes the systematic errors induced by the radar system, including the antennas. Contributions to the systematic errors in radar measurements are due to two major

sources: frequency response of the RF components of the system and polarization coupling effects. The effects of these error sources are reduced with this technique.

This calibration is based on the assumption that the measured voltage scattering coefficient of an object at each polarization is the linear combination of the true voltage scattering coefficients from the four polarizations. For example, the measured voltage scattering coefficient for VV polarization, s_{vv}^m is given by,

$$s_{vv}^m = c_{10} + c_{11}s_{vv}^0 + c_{12}s_{hh}^0 + c_{13}s_{vh}^0 + c_{14}s_{hv}^0 \quad (4.2)$$

where s_{vv}^0 , s_{hh}^0 , s_{vh}^0 , and s_{hv}^0 are the true voltage scattering coefficients for the target for each polarization combination. The nature of the coefficients c_{ij} will be discussed later.

For the set of four linear polarization combinations there are three additional equations similar to (4.2). The c_{i0} terms represent the isolation error, usually due to the anechoic chamber in which data are taken. If the isolation terms are considered to be negligible the following matrix equation results,

$$\begin{bmatrix} s_{vv}^m \\ s_{hh}^m \\ s_{vh}^m \\ s_{hv}^m \end{bmatrix} = \begin{bmatrix} c_{11} & c_{12} & c_{13} & c_{14} \\ c_{21} & c_{22} & c_{23} & c_{24} \\ c_{31} & c_{32} & c_{33} & c_{34} \\ c_{41} & c_{42} & c_{43} & c_{44} \end{bmatrix} \cdot \begin{bmatrix} s_{vv}^0 \\ s_{hh}^0 \\ s_{vh}^0 \\ s_{hv}^0 \end{bmatrix} \quad (4.3)$$

The 4 x 4 matrix is called the calibration matrix, \bar{C} . The diagonal terms are due to frequency response of the components within the system and mismatches within the

system. These terms also account for the errors due to the different physical paths for the different polarizations in the radar system. The off-diagonal terms are due to polarization coupling or polarization leakage effects in the transmit and receive paths of the radar system. Leakage between polarizations can come from imperfect switches in the RF section as well as from antennas with limited polarization purity. The amount of contribution to the off-diagonal terms caused by the switches is determined by their isolation. The coefficient c_{32} , for example, accounts for the contribution of the HH component of σ^0 in the measurement of the VH component of σ^0 . This value is roughly equivalent to the polarization purity of the antennas when ideal switches are used.

All of these coefficients can be estimated by using only three calibration targets if several simplifying assumptions are made. First, the isolation error is ignored since this is simply the return with no target. In an indoor measurement facility the chamber is primary the source for these errors. In this study the measurements were made outdoors over a frozen saline pond and the isolation error is negligible. In addition to this assumption, the coefficients c_{12} , c_{21} , c_{34} and c_{43} are assumed to be negligible. These terms, called double leakage terms, arise from polarization leakage in both the transmit and receive paths simultaneously. These differ from the remaining off-diagonal terms which are due to polarization leakage either in the receive or the transmit path. The double leakage terms are generally small in comparison to the rest of the matrix for antennas with modest polarization purity. For example, an antenna with a polarization purity of 20 dB will result in double leakage terms that are 40 dB down from the dominant terms, whereas the remaining off-diagonal terms are roughly 20 dB down.

With these assumptions the remaining coefficients can be determined by performing fully polarimetric measurements on the three independent calibration targets. The metal sphere, the diplane in a depolarizing orientation (45° or 135°) and the diplane in a non-depolarizing orientation (0° or 90°) are the targets used to perform this calibration. These targets can be used to find the remaining coefficients and thus quantify \bar{C} . The sphere has a theoretical scattering matrix given by, $\bar{S}_{\text{sphere}} = \begin{bmatrix} 1 & 1 & 0 & 0 \end{bmatrix}^T$, where the notation here for the scattering matrix is $\bar{S} = [s_{vv}, s_{hh}, s_{vh}, s_{hv}]^T$. The scattering matrices for the diplane oriented vertically and horizontally (0° and 90°) are given as, $\bar{S}_{\text{diplane}0} = \begin{bmatrix} 1 & -1 & 0 & 0 \end{bmatrix}^T$, and $\bar{S}_{\text{diplane}90} = \begin{bmatrix} -1 & 1 & 0 & 0 \end{bmatrix}^T$. The scattering matrices for the diplane in its depolarizing orientations are, $\bar{S}_{\text{diplane}45} = \begin{bmatrix} 0 & 0 & -1 & -1 \end{bmatrix}^T$ and $\bar{S}_{\text{diplane}135} = \begin{bmatrix} 0 & 0 & 1 & 1 \end{bmatrix}^T$, where the angle is measured relative to vertical direction. Using these known ("true") scattering matrices and the actual measured scattering matrices, the calibration matrix \bar{C} can be obtained. The algorithmic details in computing \bar{C} are outlined in section 4.3.

This calibration matrix is then inverted so that better estimates of the true scattering coefficients can be obtained from the measured scattering coefficients. The true scattering coefficients can be obtained by a matrix multiplication of the inverse of the scattering matrix \bar{C} with the set of measured scattering coefficients from the four polarization combinations,

$$\bar{S}^0 = \bar{C}^{-1} \cdot \bar{S}^m. \quad (4.4)$$

Here \bar{S}^m represents the measured scattering coefficients and \bar{S}^0 represents the true scattering coefficients at the four polarization combinations as in (4.3). With this vector calibration any fully polarimetric measurement made by the radar system can

be used to obtain better estimates of the true scattering coefficients. The final step involves using the true scattering coefficients and the radar equation for surface targets to obtain a calibrated value for σ^0 , the backscatter coefficient. Similarly, the traditional radar equation can be used with the corrected scattering coefficients from hard targets to obtain calibrated radar cross sections, σ for the targets. The absolute calibration was made by feeding the measured scattering coefficients from either the Luneburg lens or the sphere through the correction matrix procedure to obtain an absolute level. The lens was used for absolute (scalar) calibration because its experimental radar cross section was documented [Bredow, 1989]. Before application to artificial sea ice returns, the vector calibration was applied to the simple calibration targets in order to validate the algorithm and reveal any limitations.

4.3 Implementation of the complex vector calibration algorithm

The calibration matrix \bar{C} , which is needed to characterize the radar system is obtained by using three calibration targets. The implementation of the algorithm begins with equation (4.3). For the sphere return, the components s_{vh}^0 and s_{hv}^0 are ideally zero so the measured co-polar terms can be expressed as

$$s_{vv}^m = c_{11} + c_{12}, \quad (4.5)$$

and

$$s_{hh}^m = c_{21} + c_{22}. \quad (4.6)$$

When the double-leakage terms (c_{12} and c_{21}) are neglected, the c_{11} and c_{22} coefficients simply become s_{vv}^m and s_{hh}^m , the measured co-polar scattering coefficients from the sphere.

The measured cross-polarized scattering coefficients from the sphere yield the equations,

$$s_{vh}^m = c_{31} + c_{32}, \quad (4.7)$$

and

$$s_{hv}^m = c_{41} + c_{42}. \quad (4.8)$$

Likewise, the measured cross-polarized returns from the diplane at 0° orientation yield,

$$s_{vh}^m = c_{31} - c_{32}, \quad (4.9)$$

and

$$s_{hv}^m = c_{41} - c_{42}. \quad (4.10)$$

Equations (4.7) and (4.9) are solved simultaneously to obtain the coefficients c_{31} and c_{32} while (4.8) and (4.10) are used to obtain the coefficients c_{41} and c_{42} . The measurements from the diplane at 0° orientation and metal sphere are used to calculate the left half of the calibration matrix. If the double-leakage terms cannot be neglected they may be obtained by solving the set of simultaneous equations obtained from the co-polar measurements from both the sphere and diplane instead of just the sphere return as outlined above.

The diplane at 45° orientation is used in the calculation of the c_{33} and c_{44} returns. Since the true co-polar scattering coefficients for the diplane in this orientation are zero the following equations relate the measured returns to the calibration coefficients,

$$s_{vh}^m = -(c_{33} + c_{34}), \quad (4.11)$$

and

$$s_{hv}^m = -(c_{43} + c_{44}). \quad (4.12)$$

If the double-leakage terms (c_{34} , c_{43}) are once-again neglected the coefficients c_{33} and c_{44} are simply the measured cross-polarized returns from the diplane at 45° orientation.

The remaining terms to be computed are the coefficients c_{13} , c_{14} , c_{23} , and c_{24} . These are calculated with the measured co-polarized return when the diplane is at 45° . The assumption required for this is that the coefficients c_{13} and c_{14} are equivalent, as are the coefficients c_{23} and c_{24} . This yields

$$c_{13} = c_{14} = \frac{1}{2} s_{vv}^m, \quad (4.13)$$

and

$$c_{23} = c_{24} = \frac{1}{2} s_{hh}^m \quad (4.14)$$

as the estimates for these coefficients. While the assumption that these pairs of coefficients are equivalent seems rather crude on the surface, it holds if the cross-polarized scattering coefficients to be measured are the same.

Figure 4.1 shows the steps involved in applying this calibration technique to determine the scattering coefficients from a distributed targets such as a saline ice sheet. A parallel procedure can be used to "re-calibrate" the radar cross sections of the calibrations themselves in order to verify the effectiveness of the technique as well as the absolute level of the calibration. The schematic of this "re-calibration" procedure is shown in Figure 4.2. This was used to cross-calibrate the radar with the sphere and lens measurements to obtain the most accurate absolute calibration possible.

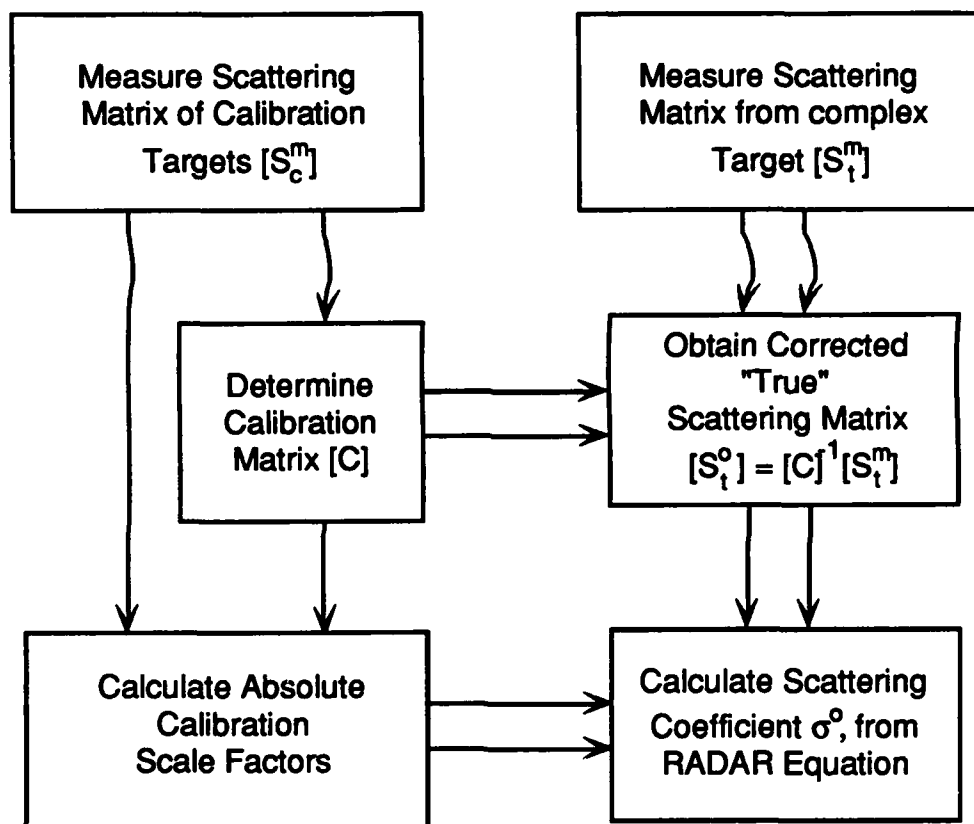


Figure 4.1. Details of the calibration procedure.

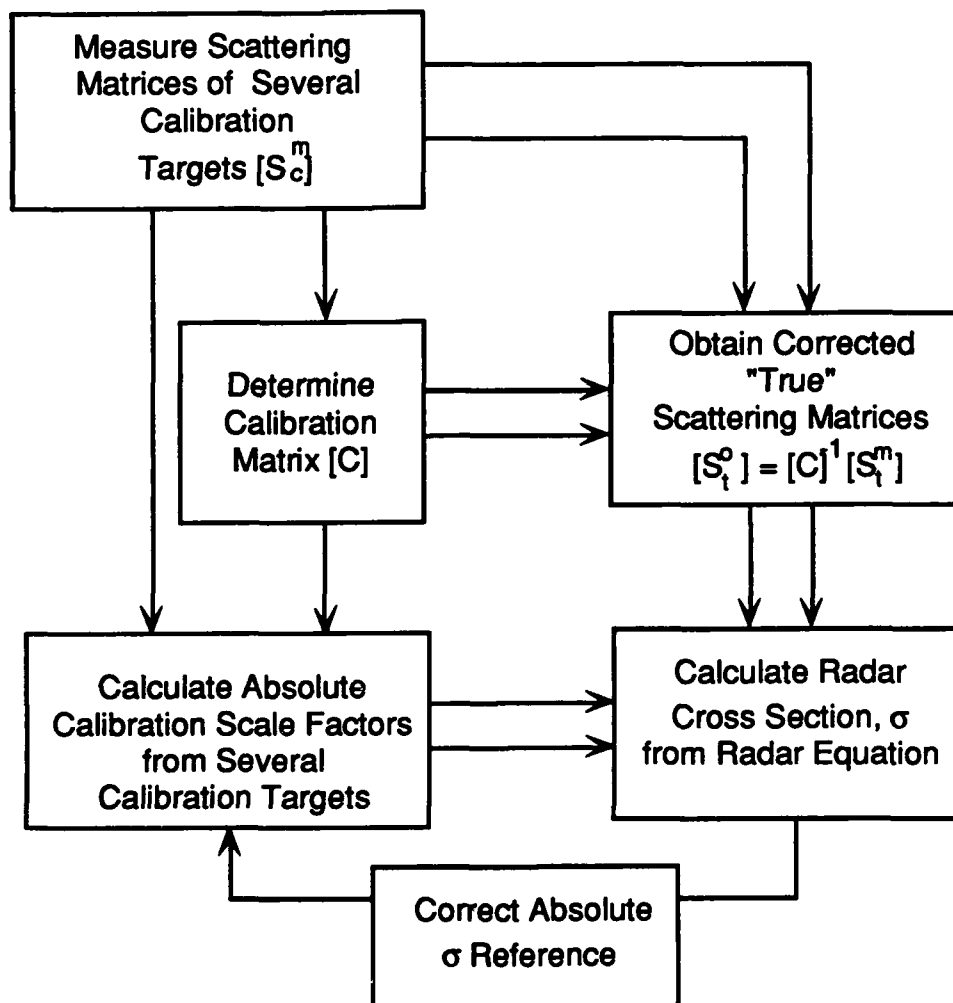


Figure 4.2. Measure of radar cross sections of hard targets using vector calibration procedure

4.4 Narrow-beam approximation to σ^0

For the usual scalar calibration, the radar equation is modified in order to account for a distributed target. When the target in question is a distributed one the radar equation can be written as

$$P_{pq} = \frac{\lambda^2}{(4\pi)^3} \iint_{A_0} \frac{P_t G_t G_r}{R^4} \sigma^0 dA. \quad (4.15)$$

If the antenna gain pattern is assumed to be a narrow beam then the gain is approximated as constant over the area illuminated. The range as well as the σ^0 variation also are assumed to vary little across the beamwidth yielding,

$$\sigma^0 = \frac{P_r \sigma_{cal} R_{cal}^4 P_{dcal}}{P_{cal} R_{cal}^4 A P_{dl}}. \quad (4.16)$$

Here P_r is the power returned from the distributed target and P_{cal} is the power returned from a calibration target of known radar cross section, σ_{cal} . The parameters P_{dcal} and P_{dl} are the delay line readings taken at the time of calibration and the time of the field measurement, respectively. The range to the distributed target is R , A is the area illuminated by the antenna, and R_{cal} is the range to the calibration target.

This equation for the calculation for the scattering coefficient is often called the narrow-beam approximation. The effect of the antenna pattern and the variation of σ^0 across the illuminated area is taken into account in a post-processing step using the technique described by [Wang and Gogineni, 1991].

The narrow-beam approximation also assumes that the polarization purity of the antennas is infinite, that is there is no horizontal component of the electric field

transmitted (or received) when the system is switched to vertical polarizations. If the polarization purity is finite, as in any real antenna system, the integral equation for the scattering coefficient becomes more complicated. The effect of the antenna limitations is demonstrated by the following. Let G_{vv} be the gain of the vertical component of the antenna system in vertical mode, G_{vh} be the gain of the vertical component of the antenna system in horizontal mode, G_{hv} be the gain of the horizontal component of the antenna system in vertical mode, and G_{hh} be the gain of the horizontal component of the antenna system in horizontal mode.

Then the measured scattering coefficient in terms of the true scattering coefficients can be expressed as,

$$P_{pp} = \frac{P_t \lambda^2 A_{eff}}{(4\pi)^3 R^4} [G_{pp}^2 \sigma_{pp}^0 + G_{qq}^2 \sigma_{qq}^0 + G_{pq}^2 \sigma_{pq}^0 + G_{qp}^2 \sigma_{qp}^0]. \quad (4.17)$$

For example the returned power for the VV component is given as

$$P_{vv} = \frac{P_t \lambda^2 A_{eff}}{(4\pi)^3 R^4} [G_{vv}^2 \sigma_{vv}^0 + G_{hh}^2 \sigma_{hh}^0 + G_{vh}^2 \sigma_{vh}^0 + G_{hv}^2 \sigma_{hv}^0]. \quad (4.18)$$

This is the scalar approximation to the vector model assumed in the complex vector calibration approach, where the measured σ^0 is expressed as the linear combination of the true scattering coefficients. If we used the voltage scattering coefficients, which are related to σ^0 by $s \propto \sqrt{\sigma^0}$, then the matrix formulation of the calibration matrix results. The coefficients of the matrix are complex in order to account for both the magnitude and phase of the field quantities. As mentioned before, the complex voltage scattering coefficient must be squared as a measure of the power returned from the target to be used in equation 4.16 to obtain a measure of σ^0 .

4.5 Beamwidth correction

The use of wide-beam antennas results in a second source of systematic error if the narrow-beam approximation (equation 4.16) is used in calculating σ^0 . Since the

measurements were taken with relatively wide-beam antennas and the calculations used for σ^0 relied on the narrow-beam approximation, a wide-beam correction had to be performed on the data. In [Wang and Gogineni, 1991] a numerical procedure for recovering the backscatter coefficient from wide-beam measurements was presented. This technique utilizes a two-part linear model fit to the experimental data as well as the assumption of a Gaussian antenna beam. These assumptions are used to solve the integral form of the radar equation for surface scattering. The difference between the assumed model and the results of integration are used to correct the actual measured data. Because of this, the technique is relatively insensitive to the model chosen. This procedure was applied to the CRRELEX'90 lower pond data set and the results are shown in the following section.

5. CRRELEX'90 Results

The calibration was applied to several targets to verify its effectiveness. In addition to the targets used to generate the vector error calibration matrix, a Luneburg lens and the diplane in a second orientation were used. The vector calibration was then applied to the artificial sea ice returns to obtain high quality radar backscatter measurements. The radar cross sections of the hard targets as well as the σ^0 of the ice were measured with the normal scalar calibration as well for comparison.

5.1 Calibration target results

The vector calibration algorithm was applied to the calibration targets in order to validate the technique. The theoretical radar cross sections for the calibration targets are shown in table 5.1 for both the targets at both Ku band and C band.

Table 5.1. Theoretical Radar Cross Sections for Calibration Targets				
	Ku-band σ (dBm ²)		C-band σ (dBm ²)	
Calibration Target	co-pol.	cross-pol.	co-pol.	cross pol.
Luneburg Lens	14.7	$-\infty$	6.7	$-\infty$
Metal Sphere	-13.9	$-\infty$	-13.9	$-\infty$
Diplane (0° or 90°)	23.3	$-\infty$	16.2	$-\infty$
Diplane (45° or 135°)	$-\infty$	23.3	$-\infty$	16.2

The results for the measurements of the calibration targets at Ku band are shown in table 5.2 and the results from the C-band measurements are in table 5.3. Here, the

calculation of σ is shown for the case when only simple scalar calibration is used and when the complex vector calibration is applied.

Table 5.2. Ku-band Radar Cross sections in dBm ²								
Calibration	Scalar Calibration				Vector Calibration			
Target	σ_{vv}	σ_{hh}	σ_{vh}	σ_{hv}	σ_{vv}	σ_{hh}	σ_{vh}	σ_{hv}
sphere	-12.97	-10.9	-25.3	-22.8	-13.9	-13.9	-51.9	-52.1
Diplane 0°	17.5	18.6	-2.82	-1.82	16.6	15.6	-22.0	-22.2
Diplane 45°	4.58	2.52	18.7	20.4	-322	-312	17.9	17.9
Diplane 90°	23.1	24.5	-0.68	-0.51	22.1	21.5	-14.4	-18.1
Lens	14.9	12.8	-5.77	-9.92	13.9	9.47	-15.6	-14.5

Table 5.3. C-band Radar Cross sections in dBm ²								
Calibration	Scalar Calibration				Vector Calibration			
Target	σ_{vv}	σ_{hh}	σ_{vh}	σ_{hv}	σ_{vv}	σ_{hh}	σ_{vh}	σ_{hv}
sphere	-20.4	-14.5	-39.2	-37.3	-20.4	-15.9	-63.7	-68.7
Diplane 0°	6.90	5.81	-9.76	-14.0	6.93	4.36	-36.9	-41.2
Diplane 45°	-15.0	-8.07	7.76	8.09	-341	-338	7.77	7.34
Diplane 90°	9.15	10.1	-8.15	-8.57	9.10	8.87	-24.0	-39.3
Lens	6.70	8.14	-11.9	-24.6	6.70	6.70	-39.3	-35.8

The ratio of co-polarized σ to cross-polarized σ is increased drastically for the sphere, lens and diplane at 0° and diplane at 90°. These are ideally non-depolarizing targets. These results demonstrate that the vector error correction technique is able to remove

systematic errors and obtain a better estimate of the true rcs of these targets. For the diplane at 45°, an ideally completely depolarizing target, the cross-polarized to co-polarized rcs ratio is also improved dramatically. This is illustrated by figures 5.1 and 5.2, which show the polarization ratio for the targets measured. The polarization ratio for ideally non-depolarizing targets is defined as,

$$P = \frac{\sigma_{vv} + \sigma_{hh}}{\sigma_{vh} + \sigma_{hv}}, \quad (5.1)$$

and for ideally depolarizing targets as,

$$P = \frac{\sigma_{vh} + \sigma_{hv}}{\sigma_{vv} + \sigma_{hh}}. \quad (5.2)$$

Here, σ_{ij} is the radar cross section for ij polarization combination and i or j denotes v or h , representing vertical or horizontal polarization. The polarization ratio for each of the hard targets when the vector calibration is applied, compared to the scalar calibration is shown in figure 5.1 for the Ku-band case. The C-band results are shown in figure 5.2. These results demonstrate the ability of the vector calibration to effectively increase the dynamic range of the measurements performed by the radar systems.

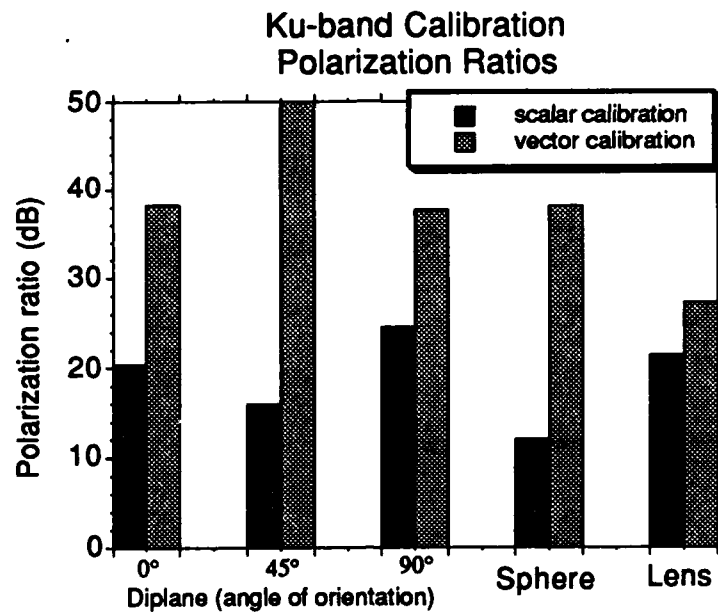


Figure 5.1. Polarization ratio comparison for Ku-band targets between scalar and vector calibration. The polarization ratio for the diplane at 45° is limited by the dynamic range used in the computation since the calculation depends on this return.

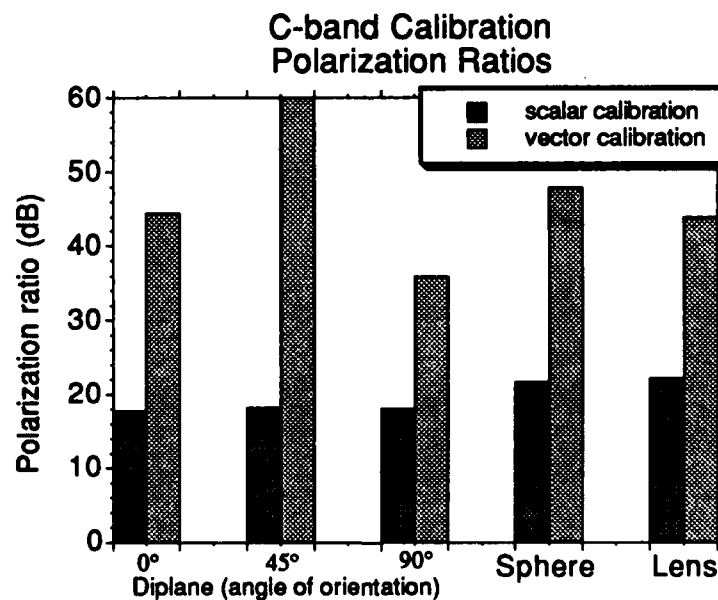


Figure 5.2. Polarization ratio comparison for C-band targets between scalar and vector calibration.

5.2 Polarimetric responses

Polarimetric response of the calibration targets were derived from the fully polarimetric data before and after applying the vector calibration to the data. The polarimetric response (sometimes called polarization signature) gives the scattering coefficient for an arbitrary incident polarization. The co-polarized response gives the scattering coefficient for the same polarization as would be transmitted as a function of the transmitted polarization. The cross-polarized response gives the scattering coefficient of the orthogonal polarization as a function of the incident polarization. The polarization is defined by the ellipticity and the orientation of the major axis with respect to vertical. The polarization response can be obtained from the measurement of the (voltage) scattering coefficient at the four linear polarizations: VV, HH, VH, and HV [Riegger, 1989].

The scattering matrix for any pair of similarly related orthogonal polarizations can be obtained from the linear ones by the relation,

$$[S^{\wedge}] = [Q(\alpha_2, \Psi_2)]^{-1} [S] [Q(\alpha_1, \Psi_1)], \quad (5.3)$$

where,

$$[S] = \begin{bmatrix} S_{hh} & S_{hv} \\ S_{vh} & S_{vv} \end{bmatrix}, \quad (5.4)$$

and S^{\wedge} is a new coordinate basis,

$$[S^{\wedge}] = \begin{bmatrix} \hat{S}_{11} & \hat{S}_{12} \\ \hat{S}_{21} & \hat{S}_{22} \end{bmatrix}. \quad (5.5)$$

$Q(\alpha_1, \Psi_1)$ is an operator associated with the incident field and $Q(\alpha_2, \Psi_2)$ is the operator associated with the scattered field. These are given in terms of the angles α and ψ as,

$$Q = \begin{bmatrix} \cos \psi \cos \alpha - j \sin \psi \sin \alpha & -\sin \psi \cos \alpha + j \cos \psi \sin \alpha \\ \sin \psi \cos \alpha + j \cos \psi \sin \alpha & \cos \psi \cos \alpha + j \sin \psi \sin \alpha \end{bmatrix}. \quad (5.6)$$

The angle α corresponds to the axial ratio of the polarization ellipse describing either the incident (with subscript 1) or scattered (subscript 2) polarization. For linear polarizations $\alpha=0^\circ$, and for circular polarizations $\alpha=\pm 45^\circ$. The angle ψ is the amount of rotation in the plane perpendicular to the direction of propagation that the wave polarization vector must move to align with the vertical direction ($\psi=0^\circ$). The new scattering coefficient s_{22}^{\wedge} plotted versus α and ψ define what is commonly referred to as the co-polarized polarization response. This is a plot of the co-polarized scattering coefficient for an arbitrary incident polarization vector and corresponding scattering polarization. Similarly, the plot of s_{12}^{\wedge} versus these angles is the cross-polarized response. This is a scattering coefficient plot versus an arbitrary incident polarization with the corresponding orthogonally-polarized scattered field.

5.3 Polarimetric responses for the calibration targets

The polarization responses for the calibration targets measured during CRRELEX'90 were derived from the linear polarization measurements. The ideal polarization responses for the calibration targets used are shown in figures 5.3, 5.4 and 5.5 [Ulaby, 1990]. These are used to judge the quality of the vector calibration as it applies to the calibration targets. The diplane polarization response demonstrates the value of the orientation variable in the signature. When the diplane is rotated by 45° the polarization response shows a shift of 45° along the orientation axis as shown in figures 5.4 and 5.5. This is useful in radar classification of targets when the orientation is unknown.

The polarization responses for the calibration targets were computed before and after applying the vector calibration. These are shown in the following series of figures for C band, followed by the same for Ku band. For all figures, the co-polarized polarization response is on the left and the cross-polarized response on the right. These demonstrate the improved responses for the calibration targets when the vector calibration is used.

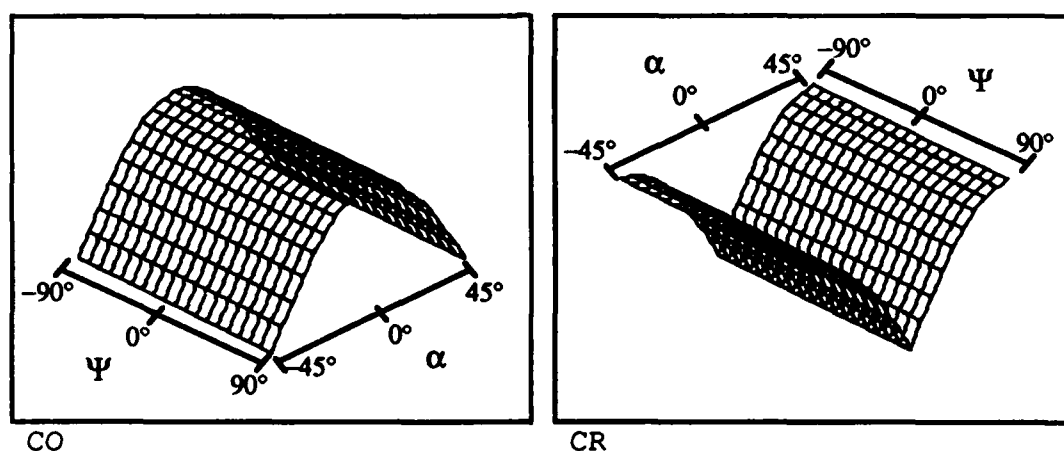


Figure 5.3. Ideal polarization response for a perfectly-conducting metal sphere. The co-polarized polarization response is on the left and the cross-polarized response is on the right.

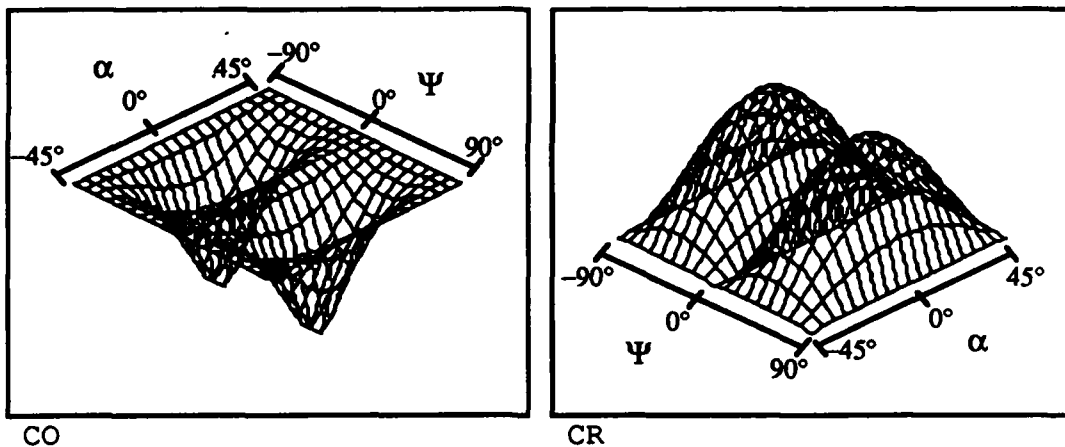


Figure 5.4. Ideal polarization response for a dihedral corner reflector oriented either vertically or horizontally. The co-polarized polarization response is on the left and the cross-polarized response is on the right.

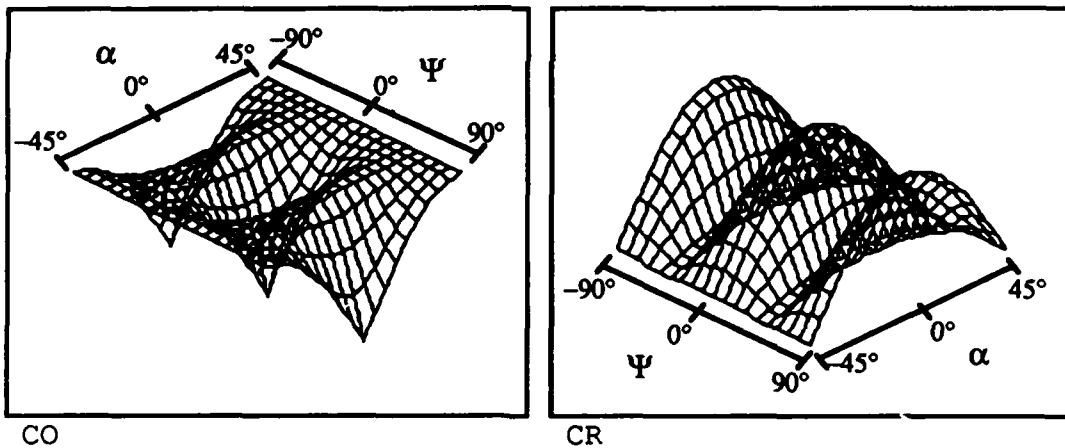


Figure 5.5. Ideal polarization response for a dihedral corner reflector oriented 45° from vertical. The co-polarized polarization response is on the left and the cross-polarized response is on the right. Note the shift of 45° along the orientation axis from figure 5.4.

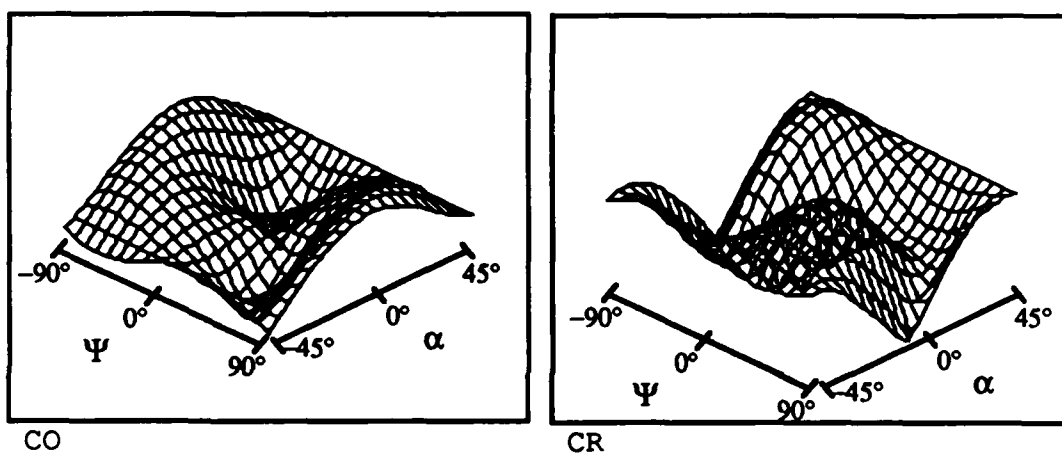


Figure 5.6 C-band polarimetric response for the metal sphere before the complex vector calibration was applied. The co-polarized response is on the left and the cross-polarized response is on the right.

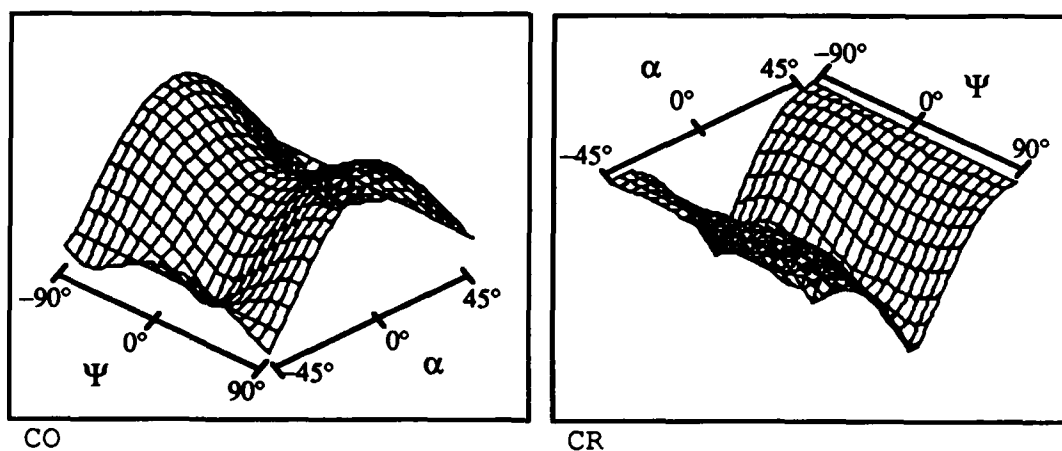


Figure 5.7 C-band polarimetric response for the metal sphere after the complex vector calibration was applied. The co-polarized response is on the left and the cross-polarized response is on the right.

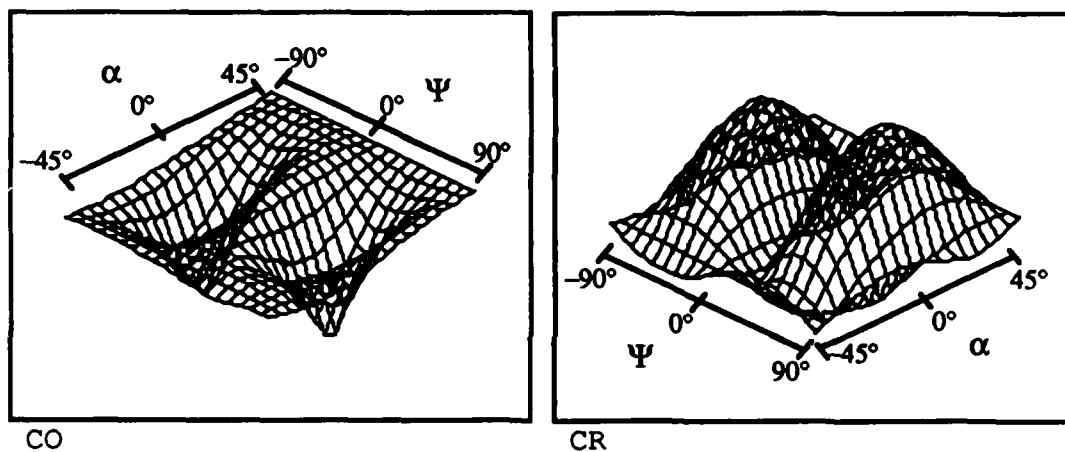


Figure 5.8 C-band polarimetric response for dihedral corner reflector at 0° orientation before the complex vector calibration was applied.

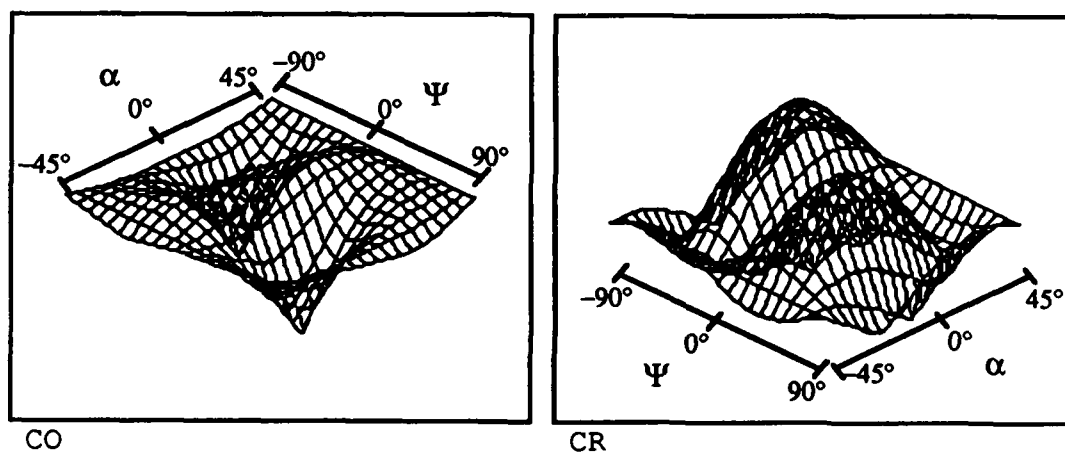


Figure 5.9 C-band polarimetric response for dihedral corner reflector at 0° orientation after the complex vector calibration was applied.

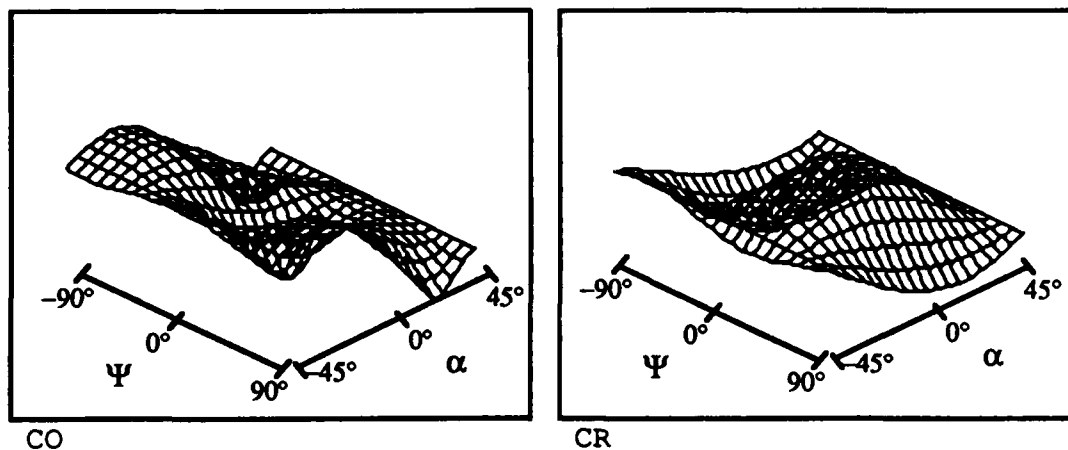


Figure 5.10 C-band polarimetric response for dihedral corner reflector at 45° orientation before the complex vector calibration was applied. The co-polarized response is on the left and the cross-polarized response is on the right.

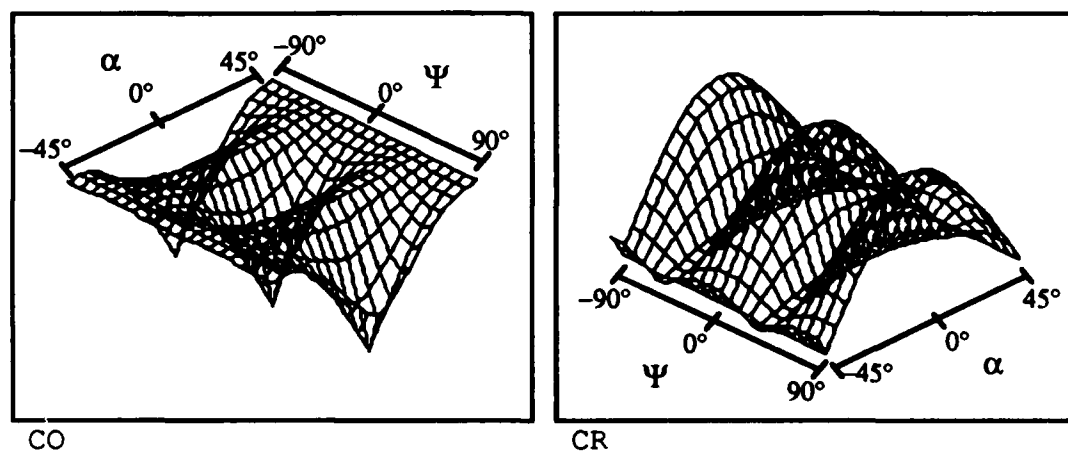


Figure 5.11 C-band polarimetric response for dihedral corner reflector at 45° orientation after the complex vector calibration was applied. The co-polarized response is on the left and the cross-polarized response is on the right.

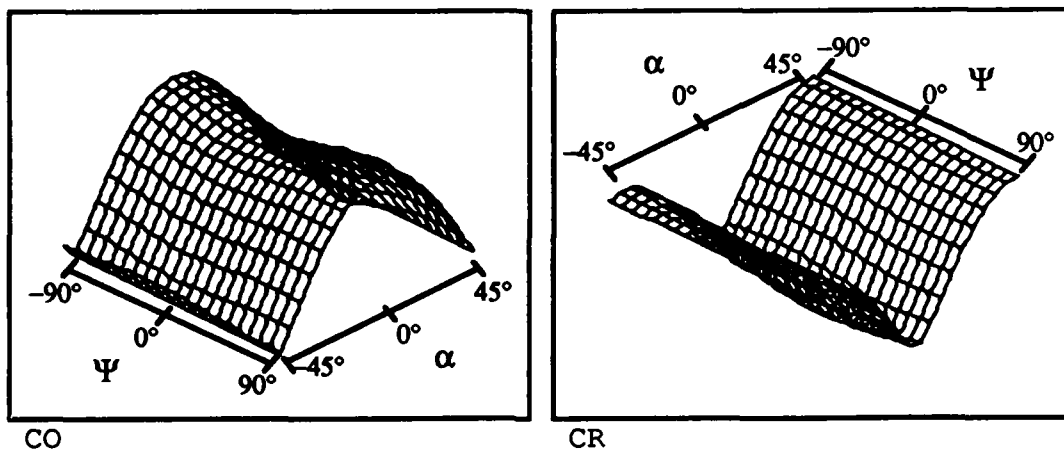


Figure 5.12 C-band polarimetric response for dihedral corner reflector at 90° orientation before the complex vector calibration was applied. The co-polarized response is on the left and the cross-polarized response is on the right.

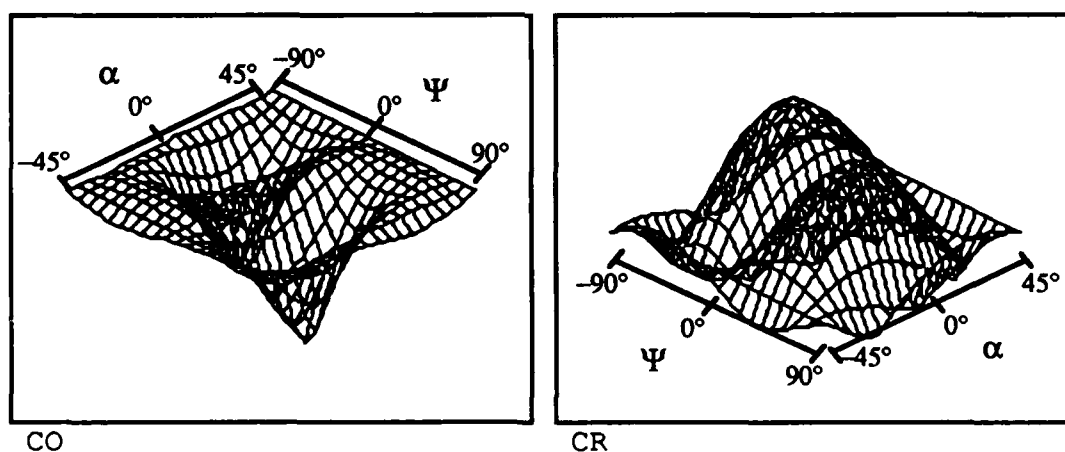


Figure 5.13 C-band polarimetric response for dihedral corner reflector at 90° orientation after the complex vector calibration was applied. The co-polarized response is on the left and the cross-polarized response is on the right.

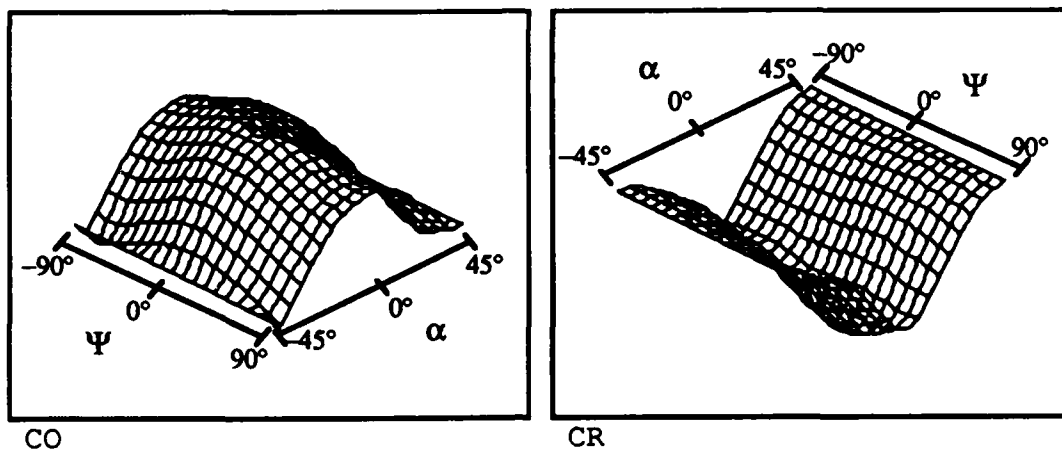


Figure 5.14 Ku-band polarimetric response for the metal sphere before the complex vector calibration was applied.

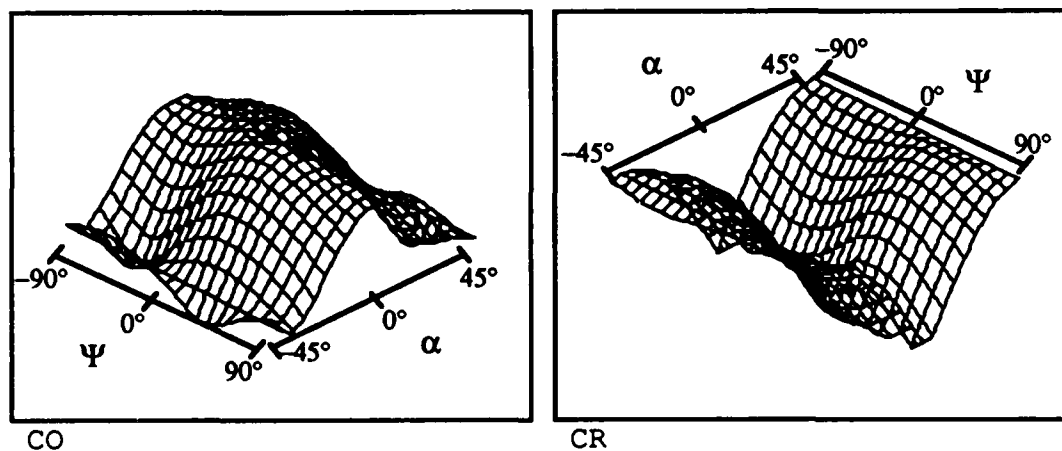


Figure 5.15 Ku-band polarimetric response for the metal sphere after the complex vector calibration was applied.

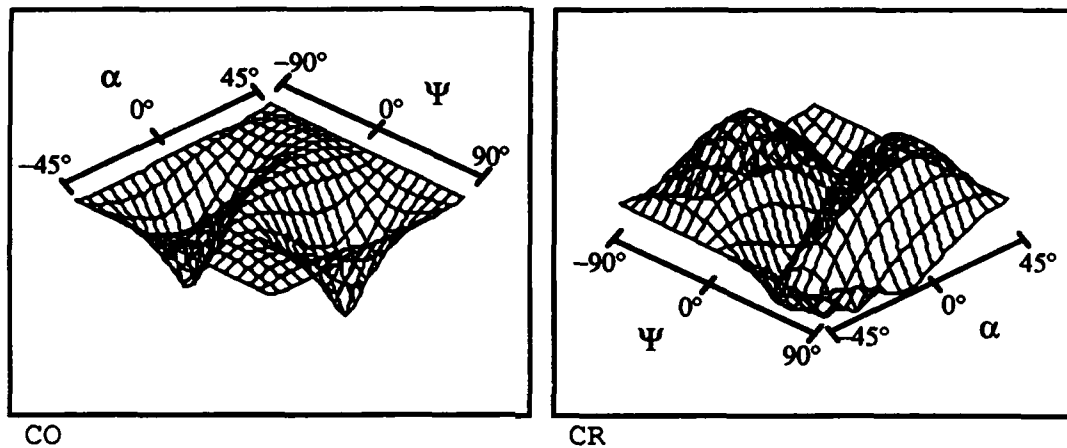


Figure 5.16 Ku-band polarimetric response for the diplane at 0° orientation before the complex vector calibration was applied.

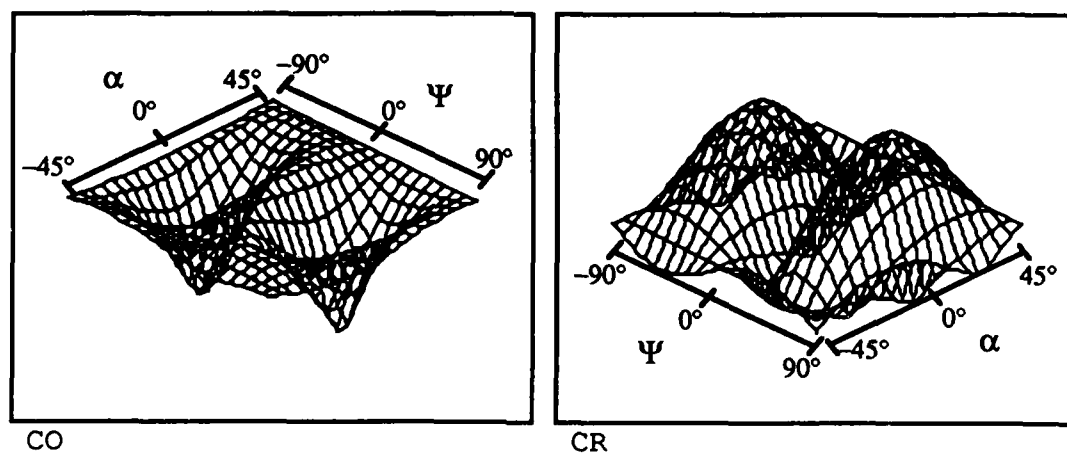


Figure 5.17 Ku-band polarimetric response for the diplane at 0° orientation after applying the complex vector calibration.

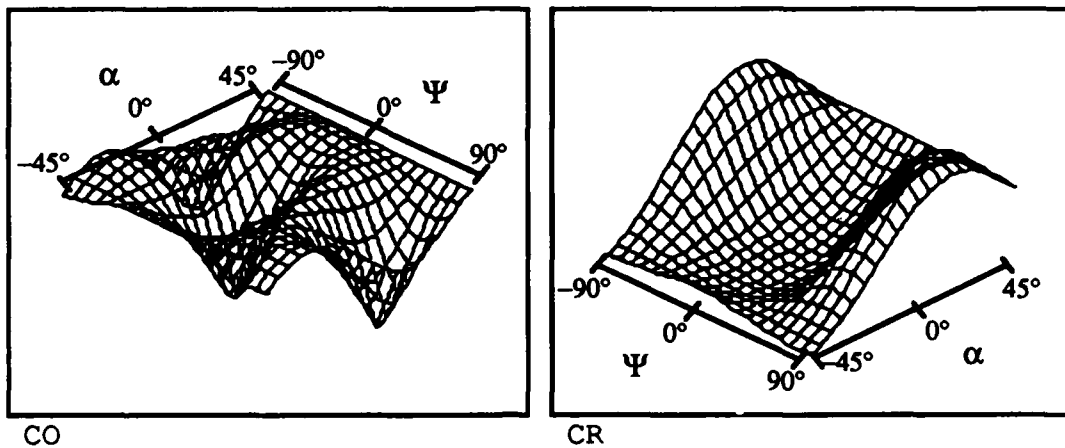


Figure 5.18 Ku-band polarimetric response for the diplane at 45° orientation before applying the complex vector calibration.

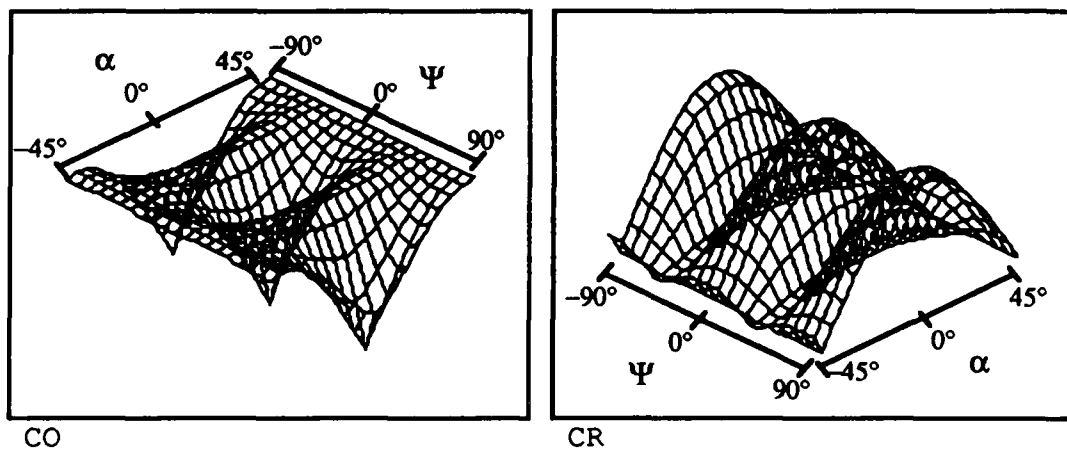


Figure 5.19 Ku-band polarimetric response for the diplane at 45° orientation after applying the complex vector calibration.

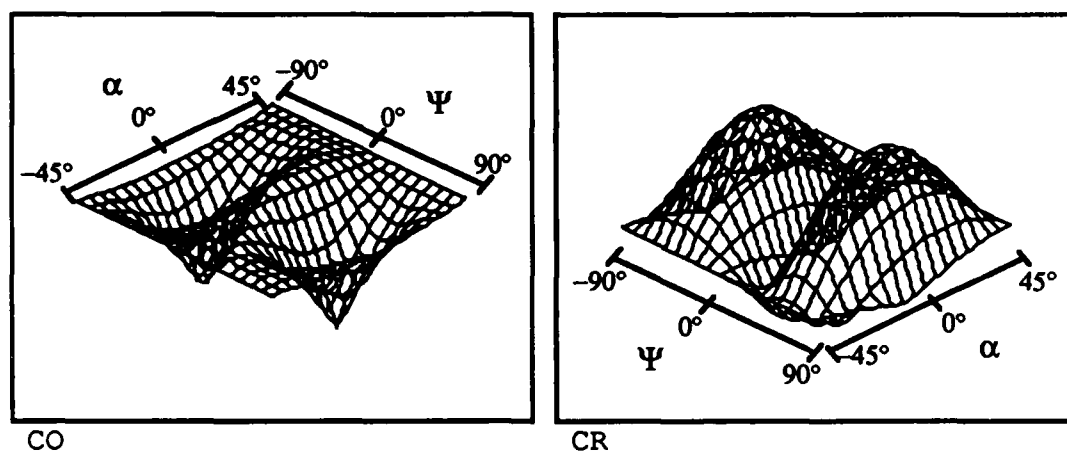


Figure 5.20 Ku-band polarimetric response for the diplane at 90° orientation before applying the complex vector calibration.

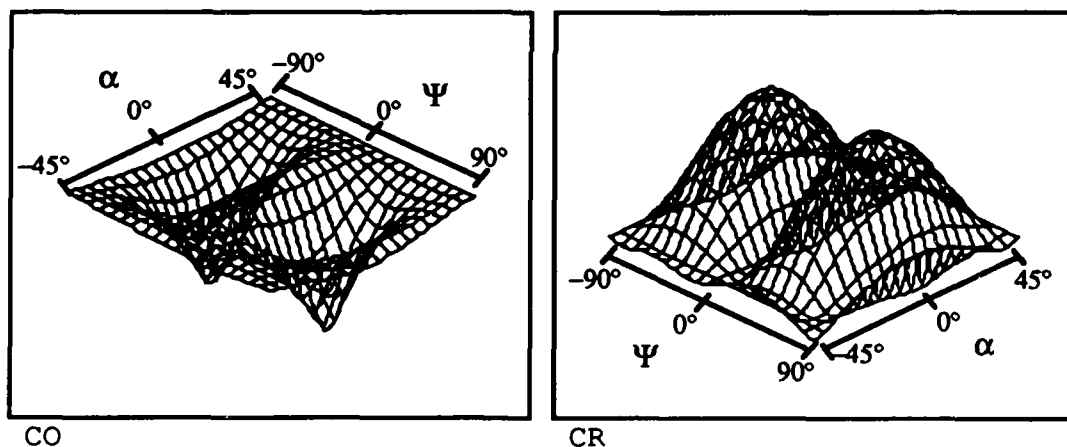


Figure 5.21 Ku-band polarimetric response for the diplane at 90° orientation after applying the complex vector calibration.

Note the dramatic improvement in the polarization responses for the diplane at 90° orientation and the sphere at C band. The other polarization responses demonstrate some improvement, which is evident in the raising and sharpening of the peaks and valleys in the responses.

5.4 Simulated sea ice results

Once the effectiveness of the method was verified the calibration was applied to complex returns from the artificial sea ice measurements. Two resulting backscatter coefficient (σ^0) measurements for data taken during the March experiment are shown in figures 5.22 and 5.23 for the C-band and Ku-band systems, respectively. For comparison, σ^0 measurements using the scalar calibration are also shown in figures 5.24 and 5.25. These demonstrate the improvement in dynamic range of the measurements when the vector calibration is applied. The ratio of co-polar to cross-polar σ^0 is much higher for the vector-calibrated data than for the scalar-calibrated data. These results are corrected for errors introduced by wide-beam antennas as described in section 4.5.

These results are from the early March portion of the CRRELEX'90 campaign. These curves are characteristic of those from slightly rough surfaces. Both the vector calibration and the scalar calibration were applied to all measurements made during the experiment at CRREL's lower pond facility. The resulting σ^0 vs. angle of incidence for both the scalar and vector calibration schemes are shown in appendices A and B before applying the wide-beam antenna correction. Appendix A shows the scalar calibrated results for Ku band and C band. Appendix B shows the Ku-band

and C-band results after applying the vector calibration. The resulting σ^0 vs. angle of incidence plots after the application of the wide-beam antenna correction are shown in Appendix C for scalar calibration and in Appendix D for the vector calibration.

These backscatter measurements show a strong angular trend, characteristic of scattering from smooth surfaces. The results, after careful calibration, are compared with surface scattering theory in the next section. This demonstrates that the primary backscatter mechanism from the saline ice during CRRELEX'90 was surface scatter.

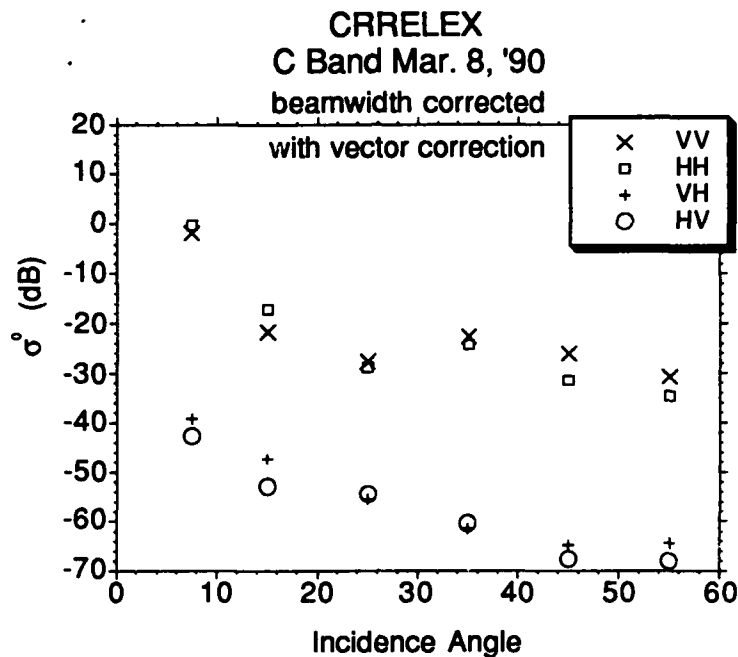


Figure 5.22 Backscatter from saline ice at C band using the complex vector calibration. These measurements show the improvement in the dynamic range of the measurement.

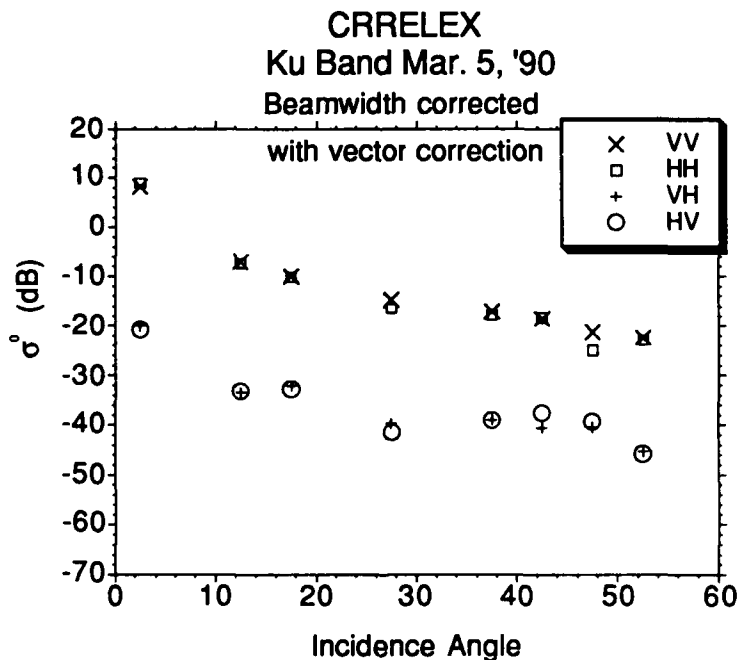


Figure 5.23 Backscatter from saline ice at Ku band using the complex vector calibration. These measurements show the improvement in the dynamic range of the measurement.

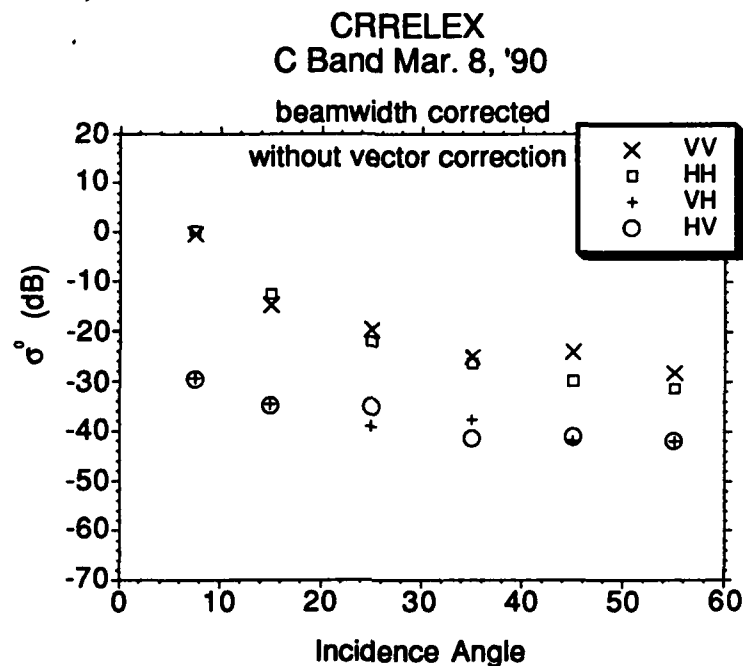


Figure 5.24 Backscatter from saline ice at C band using scalar calibration. These measurements show the effect of polarization leakage in the cross-polarized return.

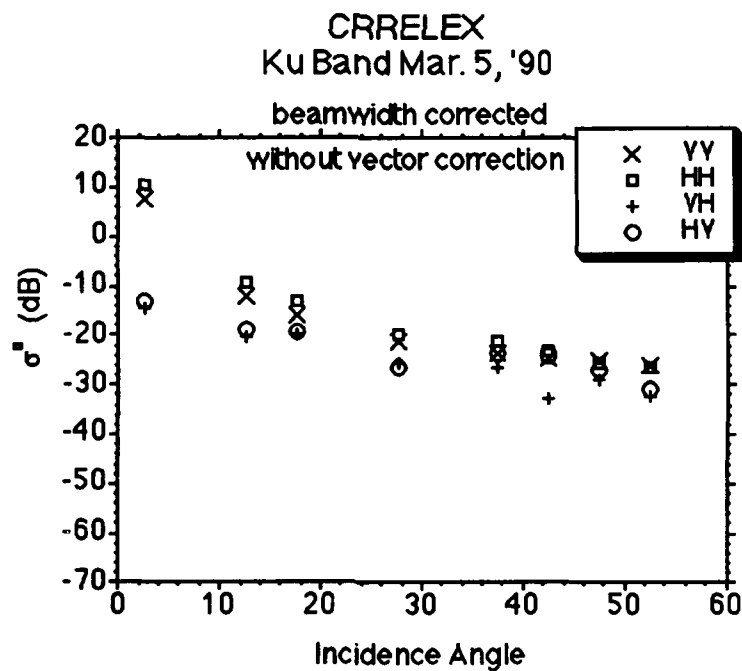


Figure 5.25. Backscatter from saline ice at Ku-band using scalar calibration. These measurements show the effect of polarization leakage in the cross-polarized return.

6. Comparison of Backscatter Measurements From Simulated Sea Ice to Rough Surface Scattering Theory

The microwave backscatter measurements performed at CRREL were fit to simple scattering models to verify the quality of the data set and to demonstrate that the primary backscatter mechanism is surface scattering. The first of these models is the small perturbation model for backscatter from a non-periodic random rough surface.

A random rough surface is characterized by the dielectric constant of the medium, the surface correlation function, and the standard deviation of the surface height σ_h , also called the rms surface height. The correlation length, L_c is a commonly used parameter extracted from the correlation function. The correlation lengths and surface roughness were computed for the CRREL experiment as shown in section 4. A short table of the average surface parameters is shown in table 6.1

Table 6.1 CRRELEX'90 sea ice surface parameters		
Date	σ_h (mm)	L_{corr} (mm)
20 Jan	2.16	4.7
11 Mar	1.36	17.6

6.1 Random rough surface scattering

The scattering from any surface consists of two components: a coherent and a non-coherent component. The total backscatter is the sum of the incoherent and coherent components.

Several theories to solve the incoherent scattering from rough surfaces exist in the literature, including integral equation methods [Fung and Pan, 1987], the Kirchhoff model [Rice, 1951] and [Wu and Fung, 1972], and the small perturbation method [Ulaby, et al., 1982]. The most commonly used are the Kirchhoff model and the small perturbation method. The Kirchhoff model uses the scalar approximation to the wave equation in order to find the scattered field intensities. This is considered a physical optics (PO) approximation and applies to high frequency cases, when then surface parameters are large with respect to wavelength. The small perturbation method assumes that the surface height variations are small with respect to wavelength. The boundaries of limitation of the small perturbation method are shown in table 6.2 and the limits for the Kirchhoff approach are shown in table 6.3 [Ulaby, et al., 1986]. Also in these tables are the calculated parameters using the CRRELEX'90 measurements for both frequencies and both time periods as an aid in determining which scattering model may be appropriate.

Table 6.2 Limitations of small perturbation method.			
Parameter	$\frac{\sigma_h}{L_c}$	$k \cdot L_c$	$k \cdot \sigma_h$
Limits	< 0.212	< 3	< 0.3
C-band January	0.46	0.52	0.24
C-band March	0.08	1.95	0.15
Ku-band January	0.46	1.32	0.61
Ku-band March	0.08	4.94	0.38

Table 6.3 Limitations of Kirchoff model		
Parameter	k^*L_c	$\frac{L_c^2}{\sigma_h \lambda}$
Limits	> 6	> 2.7
C-band January values	0.52	0.21
C-band March values	1.95	0.52
Ku-band January values	1.32	0.5
Ku-band March values	4.94	10.2

The coherent component of the backscatter is due to the direct reflection at the surface and dominates near nadir. Also called the specular component, it can be described as [Ulaby, et al., 1982]

$$\sigma_c = \pi k_1 |a_0|^2 \delta(q_x) \delta(q_y), \quad (6.1)$$

where k_1 is the wave number in the first medium, usually free space, and a_0 is

$$a_0 = -2R_{h0}(\cos\theta) \quad (6.2)$$

for HH polarization and

$$a_0 = -2R_{v0}(\cos\theta) \quad (6.3)$$

for VV polarization. Here R_{h0} is the perpendicular (horizontal) polarization reflection coefficient and R_{v0} is the parallel (vertical) polarization reflection coefficient. Due to the dirac delta functions, $\delta(q_x)$ and $\delta(q_y)$, the coherent component exists only for 0° incidence angle in the ideal case. When using finite-beam antennas a first-order solution to the contribution due to the coherent component of the scattering is, [Fung and Eom, 1983]

$$\sigma_{ppc}^0 \equiv \frac{\Gamma_p(\theta)}{B^2} \exp(-4k^2\sigma_h^2) \exp(-\theta^2/B^2), \quad (6.4)$$

where p is the polarization, θ is the incidence angle, Γ_p is the reflection coefficient for polarization p (either H or V), and B is given by

$$B^2 = \frac{1}{\sqrt{kR_0\beta}} + (\beta/2)^2. \quad (6.5)$$

The one-sided beamwidth of the antennas is β and the range to the scatterer is R_0 .

The coherent component of the scattering must be considered when the rms surface height is smaller than $\lambda/4$ [Ulaby, et al., 1986]. The rms surface roughness is smaller than $\lambda/10$ for Ku band and $\lambda/25$ for C band in the highest rms roughness case during CRRELEX'90. Because of this, the coherent component of the scattering must be considered.

6.2 Small perturbation method

The coherent component must be combined with the non-coherent scattering component to fully describe the backscatter from a slightly rough surface. The models considered in this study for describing the incoherent scattering component are reviewed in this section.

The small perturbation method for determining the backscatter from a slightly rough random surface is fully developed in [Ulaby, 1982] in general. The primary assumptions in the small perturbation method are that the surface standard deviation, σ_h is small with respect to wavelength and the surface slope is also small. These conditions are shown in table 6.2 with approximate limits as imposed through experimentation [Ulaby, 1982] and [Chen, 1988]. These assumptions allow the fields to be approximated by the first few orders of a Taylor's series expansion. The first-order solution results are described below.

The result for backscatter and non-magnetic surfaces ($\mu_r=1$) reduces to

$$\sigma_{pq}^r = 8k^4 \sigma_h^2 \cos^4 \theta |\alpha_{pq}|^2 W(2k \sin \theta, 0), \quad (6.6)$$

where pq denotes the polarization combination (VV, HH, VH, or HV), k is the wave number in medium 1, and W is the Fourier Transform of the surface correlation function. The parameters α_{pq} are given by,

$$\alpha_{hh} = \frac{\epsilon_r - 1}{\left[\cos \theta + \sqrt{\epsilon_r - \sin^2 \theta} \right]^2},$$

$$\alpha_{vv} = (\epsilon_r - 1) \frac{\sin^2 \theta - \epsilon_r (1 + \sin^2 \theta)}{\left[\epsilon_r \cos \theta + \sqrt{\epsilon_r - \sin^2 \theta} \right]^2},$$

and

$$\alpha_{hv} = \alpha_{vh} = 0.$$

This is the first-order approximation for the cross-polarized return. No cross-polarized component due to surface scatter alone arises in small perturbation theory until higher orders are considered [Valenzuela, 1967]. The technique for calculating the theoretical cross-polarized return is shown in section 6.3.

Two common assumptions for the correlation function of random surfaces have been used to compare measurements with theory. These are the Gaussian correlation function and the exponential correlation function. It has been shown through experiment [Bredow, 1989] that the exponential correlation function assumption fits well to measured data from saline ice grown at CRREL. Using the exponential correlation assumption, equation 6.6 simplifies to,

$$\sigma_{pq} = \frac{8(k\sigma_h)^2 (kL_c)^2 \cos^4 \theta |\alpha_{pq}|^2}{\left[1 + (2kL_c \sin \theta)^2 \right]^{3/2}}. \quad (6.7)$$

This can be easily computed for the set of surface parameters as a function of incidence angle for VV and HH polarization. This is performed in section 6.5 for comparison with the CRRELEX'90 measurements. The cross-polarized component is zero under the first-order approximation. The following section describes the method by which the second order approximation to the cross-polarized return is obtained.

6.3 Cross-polarization calculations with second-order small perturbation method

The cross-polarized backscatter from random rough surface comes from using a second order approximation of the perturbation series expansion [Ulaby, et al., 1986, pp. 952]. When the second order is taken into account, the cross-polarized backscatter coefficient is,

$$\sigma_{vh}^0 = \sigma_{hv}^0 = \left[\pi k^4 \sigma_h^4 \cos^2 \theta \frac{(\epsilon_r - 1)(R_v - R_h)^2}{2} \right] \cdot \int_{-\infty}^{\infty} \int_{-\infty}^{\infty} \frac{u^2 v^2}{|D_0|^2} W(u - k \sin \theta, v) W(u + k \sin \theta, v) du dv \quad (6.8)$$

where

$$D_0 = \epsilon_r \sqrt{k_0^2 - (u^2 + v^2)} + \sqrt{\epsilon_r k_0^2 - (u^2 + v^2)},$$

and θ is the angle of incidence. $W(u, v)$ is the roughness spectrum and is related to the surface correlation $\rho(\alpha, \beta)$ by,

$$W(u, v) = \frac{1}{2\pi} \int_{-\infty}^{\infty} \int_{-\infty}^{\infty} \rho(\alpha, \beta) e^{(-j\alpha u - j\beta v)} d\alpha d\beta. \quad (6.9)$$

If the integral is transformed into cylindrical coordinates the final form of the solution, suitable for calculation on a computer, is given as:

$$\sigma_{vh}^0 = \sigma_{hv}^0 = 2\pi k_0^4 \sigma_h^4 \cos^4 \theta T_{vh} \cdot \int_0^{2\pi} \int_0^{\infty} \frac{R^5 \cos^2 \phi \sin^2 \phi W(R^+) W(R^-)}{|D_0|^2} dR d\phi. \quad (6.10)$$

The coefficient term T_{vh} can be expressed as

$$T_{vh} = \left| \frac{(\epsilon_r - 1)^2 (\sqrt{\epsilon_r - \sin^2 \theta})}{(\epsilon_r \cos \theta + \sqrt{\epsilon_r - \sin^2 \theta})(\cos \theta + \sqrt{\epsilon_r - \sin^2 \theta})} \right|^2, \quad (6.11)$$

and

$$R^\pm = \sqrt{R^2 + k_0^2 \sin^2 \theta \pm 2k_0 R \sin \theta \cos \phi}. \quad (6.12)$$

If the correlation function is assumed to be exponential, the isotropic roughness spectrum can be expressed as,

$$W(R) = \frac{L_c^2}{[1 + (L_c R)^2]^{\frac{3}{2}}}. \quad (6.13)$$

The integration in 6.10 must generally be carried out numerically. The integrand tends to be well-behaved for the range of allowable values for σ_h and L_c allowed in the small perturbation method.

6.4 Comparison of measurements with theory

Comparison of the measured cross-polarized response with the theoretical value computed from the theory presented here is made in this section. Using the small perturbation method and the surface parameters computed for CRRELEX'90, the theoretical backscatter coefficient were calculated. These computations were compared with the measurements. Figure 6.1 shows the result of the small perturbation method plotted along with the measured Ku-band co-polarized response and the result of the method of 6.3 with the cross-polarized response. The backscatter measurements were taken on the same day as the sample from which the surface roughness parameters were obtained. Since the cross-polarized response was observed to be overestimated in this case, the correlation length was adjusted to achieve a better fit to the measure data. This parametric fit is shown in figure 6.2 for a correlation length of 3.48 cm. The correlation length computation from the thick

section photographs may be a poor estimate of the actual correlation length due to the small sample length in the photographs. In slab 1a, for example, (section 4, figure 4.1) the correlation length calculation is twice that of slab 1b although both were taken at the same time.

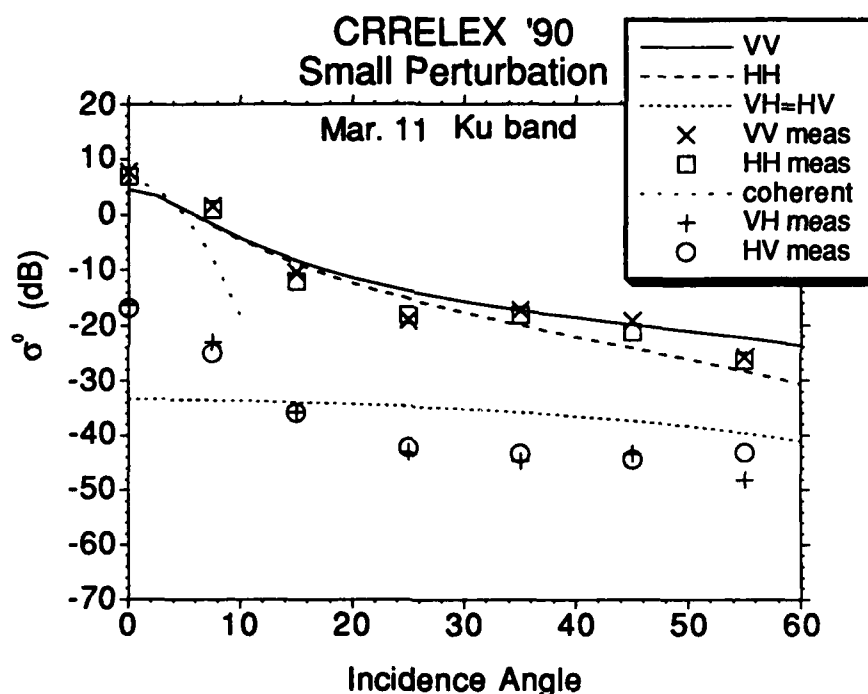


Figure 6.1 Comparison of small perturbation method with measured backscatter at Ku band from CRRELEX'90. Theory for the cross-polarized response is the integral equation method. All theoretical curves are drawn as lines, with the measurements as various symbols. This demonstrates that the primary backscatter mechanism is surface scattering. Values used in model are $\sigma_h=1.36$ mm, $L_c=17.6$ mm and $\epsilon_r=3.75-j0.2$.

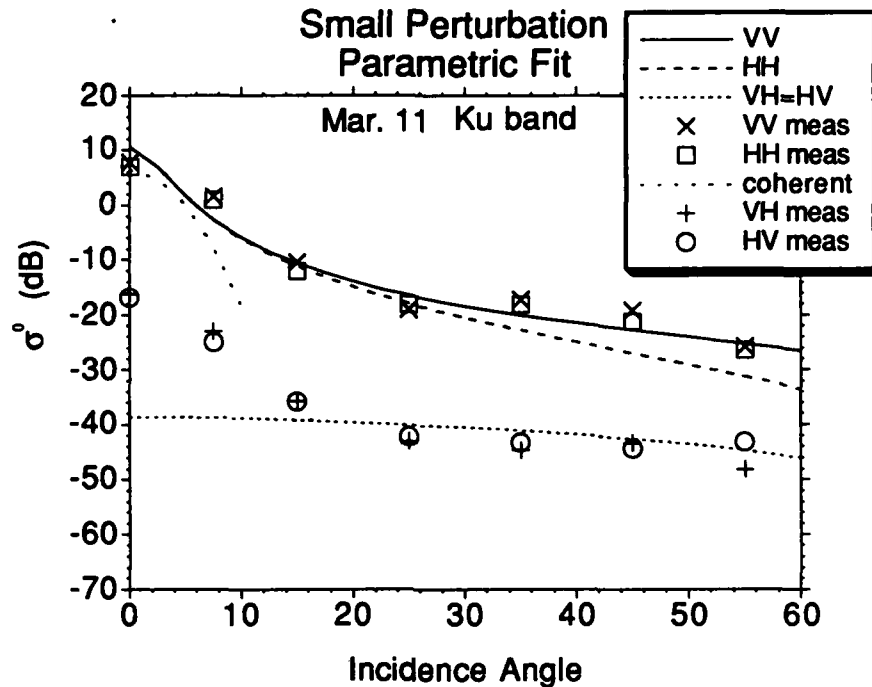


Figure 6.2 Comparison of small perturbation method with measured backscatter at Ku band from CRRELEX'90. In this case the correlation length was adjusted to achieve a better fit. Theory for the cross-polarized response is the integral equation method. All theoretical curves are drawn as lines, with the measurements as various symbols. This demonstrates that the primary backscatter mechanism is surface scattering. Values used in model are $\sigma_h=1.36$ mm, $L_c=3.52$ cm and $\epsilon_r=3.75-j0.2$.

Figure 6.3 shows the C-band results, using the computed surface parameters. Figure 6.4 shows the theoretical results obtained using the correlation length that best fit the Ku-band results. The theory and experiment generally match at both frequencies for the co-polarized response. The measured σ^0 and that calculated from the small perturbation method agree to within ± 3 dB in terms of mean-square error. However, the theory and measurements only agree grossly for the cross-polarized response, especially at C-band. The measured return at low angles of incidence is

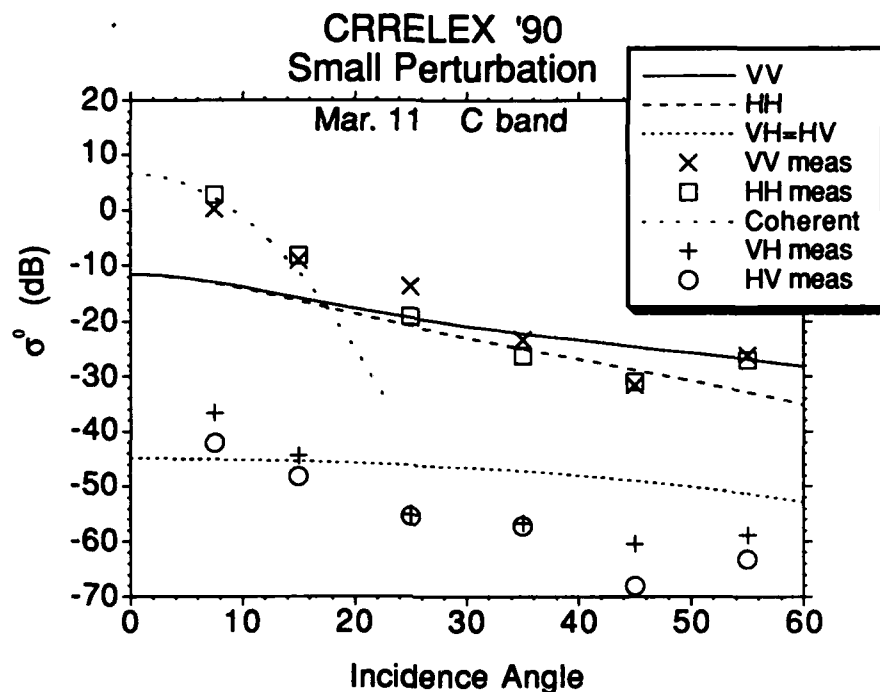


Figure 6.3 Comparison of small perturbation method with measured backscatter at C band from CRRELEX'90. Theory for the cross-polarized response is the integral equation method. All theoretical curves are drawn as lines, with the measurements as various symbols. This demonstrates that the primary backscatter mechanism is surface scattering. Values used in model are $\sigma_h=1.36$ mm, $L_c=17.6$ mm and $\epsilon_r=3.75-j0.2$.

underestimated by the theory by as much as 15 dB, while at higher angles the return is overestimated by up to 8 dB at C band. The cross-polarized measurements and the theory only agree on the general level of the backscatter, but the angular response of the cross-polarized measurements is not predicted by the method shown in section 6.3 with the surface parameters selected.

In both cases the coherent component is plotted near nadir to show that the increase in backscatter near nadir is due to the coherent component. From the limits imposed on

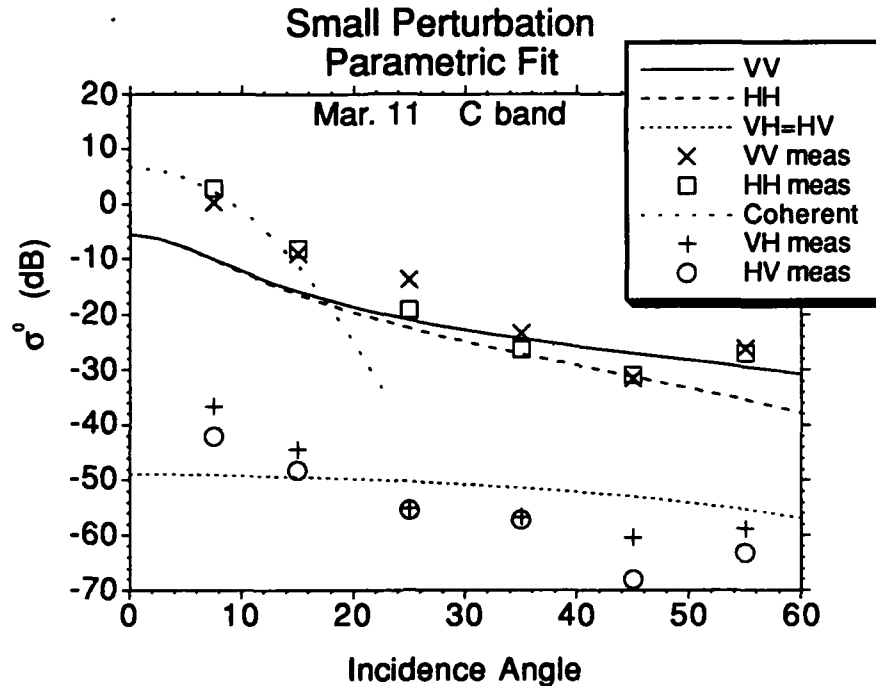


Figure 6.4 Comparison of small perturbation method with measured backscatter at C band from CRRELEX'90. In this case, the correlation length was used from the better fit obtained at Ku-band. Theory for the cross-polarized response is the integral equation method. All theoretical curves are drawn as lines, with the measurements as various symbols. This demonstrates that the primary backscatter mechanism is surface scattering. Values used in model are $\sigma_h=1.36$ mm, $L_c=35.2$ mm and $\epsilon_f=3.75-j0.2$.

the surface parameters for the small perturbation method (Table 6.2) we see that all criteria are met for the C-band case. In the Ku-band case the surface correlation length is slightly longer than that allowed by these restrictions. It must be emphasized that these restrictions are general guidelines and were brought about by numerical experimentation [Chen, 1988]. In fact in some cases the limit on correlation length is considered to be $k_0 \cdot L < 6$ [Ulaby, et, al, 1986].

For computation of error measures the combination of coherent and incoherent backscatter are plotted versus the measurements in figures 6.5 through 6.8. These correspond to figures 6.1 through 6.4, but have the result of adding the coherent and incoherent components. The resulting mean-square error between the measurements and the theoretical results are shown in table 6.4. These comparisons demonstrate that the primary backscatter mechanism for this saline ice is the scattering from the surface. However, the theory and experiment are far from a perfect match. This may be due to underestimating the surface correlation length from photographs of cross sections of samples from the ice sheet or changes in the surface roughness across the ice sheet. Another cause for the slight discrepancy between theory and measurement at Ku-band is that these data are on the edge of the limits for applying small perturbation theory. To avoid these kinds of limitations integral equation methods may be more applicable [Fung and Pan, 1987].

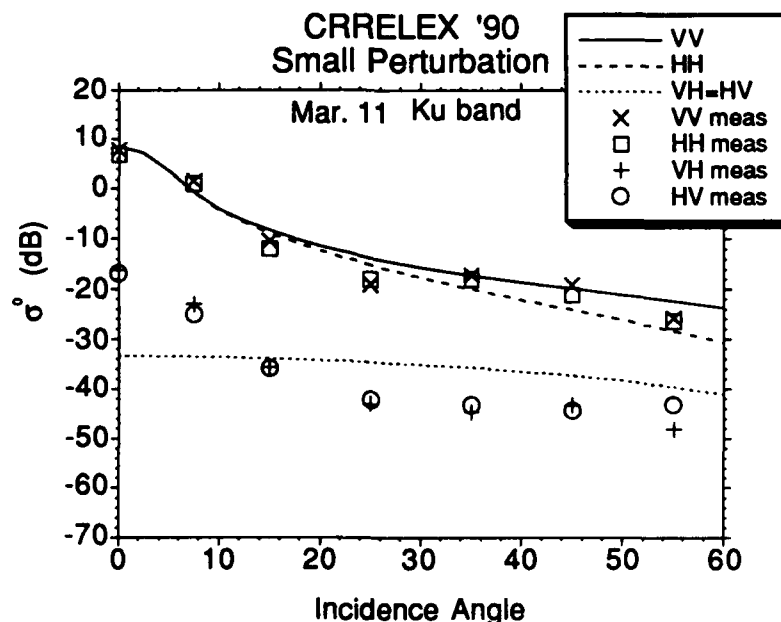


Figure 6.5 Sum of coherent and incoherent theoretical backscatter components compared to measurements at Ku band. This corresponds to the plot of figure 6.1.

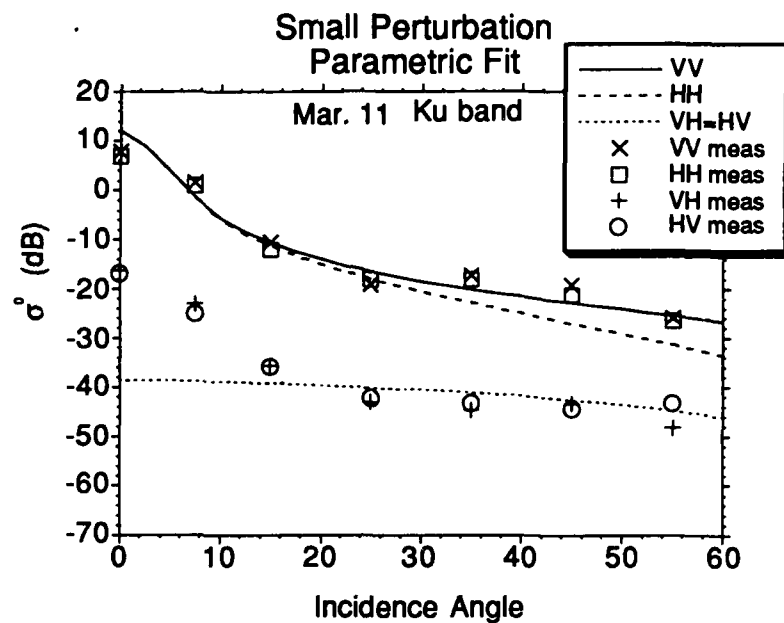


Figure 6.6 Sum of coherent and incoherent theoretical backscatter components compared to measurements at Ku band. This corresponds to the plot of figure 6.2.

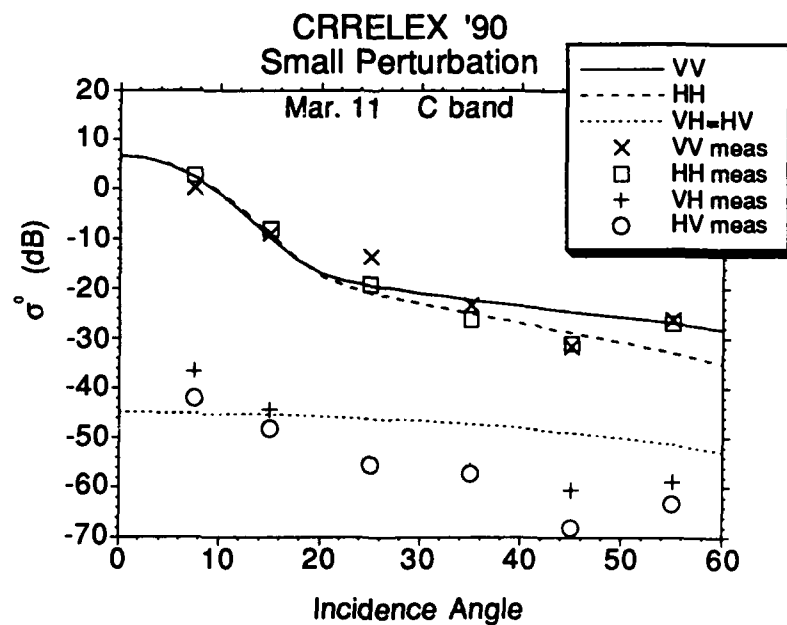


Figure 6.7 Sum of coherent and incoherent theoretical backscatter components compared to measurements at C band. This corresponds to the plot of figure 6.3.

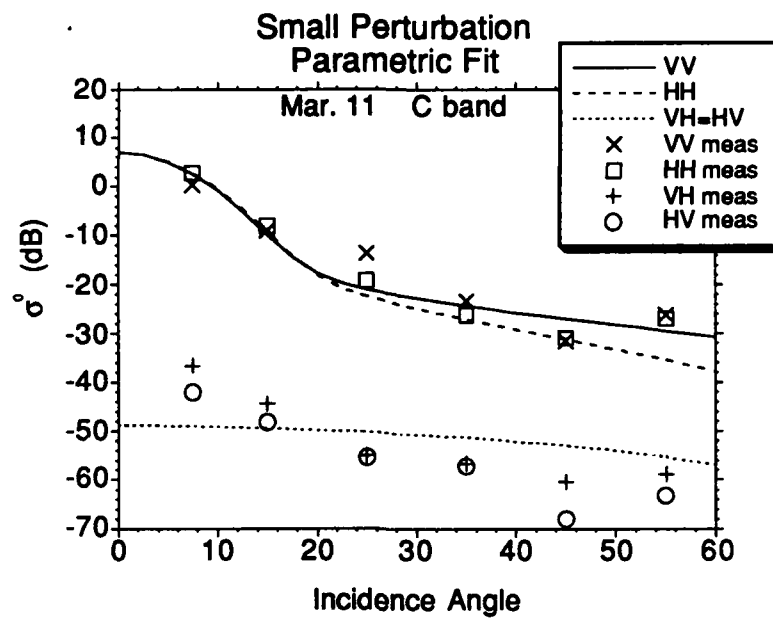


Figure 6.8 Sum of coherent and incoherent theoretical backscatter components compared to measurements at C band. This corresponds to the plot of figure 6.4.

Table 6.4. Mean-square error measures (in dB) of comparisons between theory and measurement				
	C-band	C-band parametric fit	Ku-band	Ku-band parametric fit
VV	3.8	3.9	2.7	2.8
HH	2.7	3.7	2.4	3.9
VH	8.5	7.1	9.8	10.7
HV	10.9	8.2	8.7	9.9
VH (15°-55°)	8.4	5.4	7.3	3.0
HH (15°-55°)	11.9	8.4	6.0	2.3
Corresponding Figures	7.3, 7.7	7.4, 7.8	7.1, 7.5	7.2, 7.6

For the January portion of the experiment, the surface parameters were computed from a sample taken on 20 January. The closest time frame in which backscatter measurements were performed was on 24 January. There were no C-band measurements made in late January, but both C-band and Ku-band measurements were made on 9 January. Figure 6.9 shows the Ku-band Kirchoff model and small perturbation method results compared to backscatter data from 24 January. This shows that the Kirchoff approach may be slightly more appropriate than the small perturbation method, but the characteristics of this surface lies outside the regions of validity for both theories. This violation is not severe, though, and the two theories are fairly close for large angles. This shows that in this case also, the surface scatter dominates the co-polarized return. Since there were no data taken on 20 January, data from 24 January are shown as the measured data. The time between the backscatter measurement and sampling for surface parameterization may be the primary reason for the difference between measurements and theory for this case.

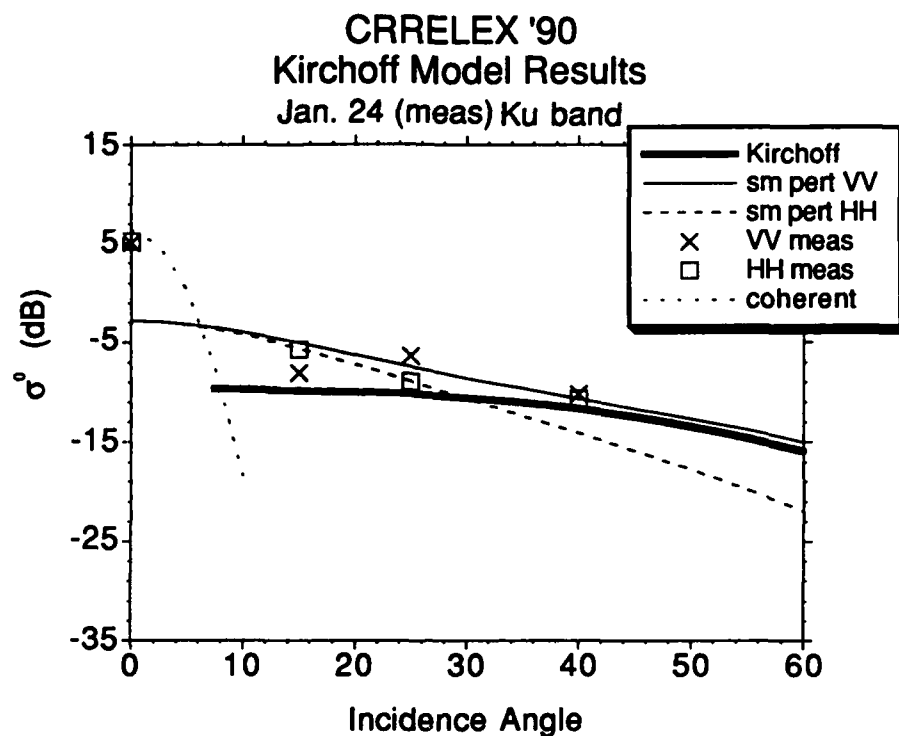


Figure 6.9 Comparison of Ku-band measurements from 24 January, with Kirchoff model and small perturbation method. Surface parameters were characterized from slab taken on 20 January. These parameters are $\sigma_h=2.16$ mm, $L_c=4.7$ mm and $\epsilon_r=3.75-j0.2$.

7. CRRELEX'90 Conclusions

7.1. Conclusions

Measurements of microwave backscatter from simulated sea ice demonstrate that the dominant backscatter mechanism is the surface scatter when an exponential correlation function is assumed for the surface. Both the co-polarized and cross-polarized measurements compare favorably with the predictions of surface scattering models at two frequencies. The surface parameters used in the models were measured directly from photographs of cross sections of the saline ice. Therefore, since two frequencies of backscatter measurements were predicted accurately by surface scatter models the predominate backscatter is from the surface. It is possible, assuming Gaussian correlation for the surface, to come to the conclusion that the volume plays a significant role in the backscatter from saline ice [Coutu, personal communication, 1992]. The autocorrelation of sea ice surfaces though tend to be closer to exponential than Gaussian.

These measurements were carefully calibrated using a complex vector error correction scheme to remove polarization coupling and other systematic effects. The dynamic range of polarimetric measurements made by scatterometers are limited by coupling and polarization leakage in the antenna system and RF section. These effects must be accounted for and corrected if one is to obtain accurate characterization of the polarimetric response of distributed targets.

This demonstrates the need for careful calibration in experiments of this type, especially when cross-polarized backscatter measurements are performed. The

systematic effects on the cross-polarized backscatter introduce significant error and may lead to misinterpretation of the results. This is a vital consideration in the study of radar backscatter from sea ice using fully polarimetric systems.

7.2 Limitations and constraints

There are limitations to the accuracy of the measurements that can be obtained when applying the vector error calibration technique. These limits depend on how carefully the measurements can be performed in a practical situation.

The signal-to-noise ratio (SNR) of each calibration target measurement must be sufficiently large. This is a problem when using a metal sphere, for example, because of its low radar cross section. An SNR of less than 10 dB may cause enough phase error to distort the calibration, resulting in measurement inaccuracies. The alignment of the calibration targets, especially in the case of the dihedral corner reflectors is vital. In one dimension, the rotation of the diplane will affect the amount of depolarization attributed to the system. An error in aligning the rotation angle may cause a mistake in characterization of the system's polarization response. Any pitch of the diplane, on the other hand will simply cause a reduction in the absolute level of the return power. This effect is taken into account in the normalization of the power returns before computing the calibration matrix.

Since wide-beam antennas were used for this experiment their effect on the measurement must be considered. In using the wide-beam correction scheme mentioned in section 4.5 and described in [Wang and Gogineni, 1990], these antenna effects are reduced. The wide-beam antenna actually helps in practical

implementation of the vector calibration because of the reduced sensitivity with respect to alignment than for narrow-beam antenna systems.

The effect of the limitations due to rotation and pitch of the calibration targets as well as random errors to low SNR is to cause some limit on the minimum measurable scattering coefficient. This dynamic range is significantly larger than when applying the simple scalar calibration as evidenced by the increase in dynamic range of the σ^0 measurements shown in sections 5 and 6.

References

- Arcone, S.A., A.J. Gow, and S. McGrew, (1986), "Microwave Dielectric, Structural and Salinity Properties of Simulated Sea Ice," *IEEE Transactions on Geoscience and Remote Sensing*, vol. 24, no. 6, pp. 832-839.
- Balanis, C.A., (1982), *Antenna Theory*, New York : Harper & Row Publishers, pp. 532-587.
- Beaven, S.G., S.P. Gogineni, S. Tjuatja, A.K. Fung, and J. Bredow (1991) "Radar Backscatter from Saline Ice: Measurements and Comparison of Measurements with Theory," *IGARSS'91*, vol. II, pp. 425-428.
- Bredow, J.W., (1989), "A laboratory Investigation Into Microwave Backscattering From Sea Ice," Ph.D. Dissertation, University of Kansas.
- Chen, T., T. Chu, and F. Chen, (1991), "A NeBand Polarimetric Measurement System," *IEEE Transactions on Antennas and Propagation*, vol. 39, no. 8, pp. 1188-1192.
- Chen, M.F., and A.K. Fung, (1988), "A Numerical Study of the Regions of Validity of the Kirchoff and Small-Perturbation Rough Surface Scattering Models," *Radio Science*, Vol. 23, No. 2, pp. 163-170, March-April, 1988.
- Coutu, Pierre, Massachusetts Institute of Technology, personal communication, Dec. 1992.

- Drinkwater, M.R., R. Kwok, D. Winebrenner, and E. Rignot, (1991), "Multi-frequency Polarimetric SAR Observations of Sea Ice," *Journal of Geophysical Research*, vol. 96 no. C11, pp. 20679-20698.
- Fung, A.K. and H.J. Eom, (1983), "Coherent scattering of a Spherical Wave from an Irregular Surface," *IEEE Transactions on Antennas and Propagation*, vol. TAP-31, pp. 68-72.
- Fung, A.K., and G.W. Pan, (1987), "A scattering model for perfectly conducting random surfaces I. Model development," *International Journal of Remote Sensing*, Vol. 8, no. 11, pp. 1579-1593.
- Houghton, J.T., G.J. Jenkins, and J.J. Ephraums, (1990), "Climate change - the IPCC scientific assessment, Cambridge University Press.
- Iizuka, K., and A.P. Freundorfer, (1984), "Step-frequency radar", *Journal of Applied Physics*, vol. 56, no. 9, pp. 2572-2583.
- Kong, J.A., (1990), Electromagnetic Wave Theory, Wiley-Interscience, New York.
- Kwok, R., M. Drinkwater, A. Pang, and E. Rignot, (1991), "Characterization and Classification of Sea Ice in Polarimetric SAR Data," *IGARSS'91*, vol.I, pp. 81-84.
- Love, A.W., (1962), "The Diagonal Horn Antenna," *The Microwave Journal* , pp. 117-122, March, 1962.

- Parkinson, C.L., J.C. Comiso, H.J. Zwally, D.J. Cavalieri, P. Gloerson, and W.J. Campbell, (1987) Arctic Sea Ice, 1973-1976: Satellite Passive-Microwave Observations, Washington DC: NASA Scientific and Technical Information Branch.
- Rice, S.O. (1951), "Reflection of Electromagnetic Waves from Slightly Rough Surfaces, *Communications in Pure and Applied Mathematics*, vol. 4, pp. 361-378.
- Riegger, S., and W. Wiesbeck, (1989), "Wide-band Polarimetry and Complex Radar Cross Section Signatures," *Proceedings of the IEEE*, vol. 77, no. 5, pp. 649-658.
- Swift, C.T., K. St. Germain, K. Jezek, S.P. Gogineni, A. Gow, D. Perovich, T. Grenfell, R. Onstott, (1992), Laboratory Investigations of the Electromagnetic Properties of Artificial Sea Ice, in: *Microwave Remote Sensing of Sea Ice*, F.D. Carsey (ed.), American Geophysical Union, Monograph 68, pp. 177-200.
- Ulaby, F.T., R.K. Moore, and A. K. Fung, (1981), *Microwave Remote Sensing: Active and Passive*, vol. I, Norwood, MA: Artech House.

Ulaby, F.T., R.K. Moore, and A. K. Fung, (1982), *Microwave Remote Sensing: Active and Passive*, vol. II, Norwood, MA: Artech House.

Ulaby, F.T., R.K. Moore, and A. K. Fung, (1986), *Microwave Remote Sensing: Active and Passive*, vol. III, Norwood, MA: Artech House.

Ulaby, F.T. and C. Elachi, (1990), Radar Polarimetry for Geoscience Applications, Artech House, Norwood, MA.

Valenzuela, G.R. (1967), "Depolarization of EM Waves by slightly Rough Surfaces," *IEEE Transaction on Antennas and Propagation*, vol. TAP-15, pp. 552-557.

Wadhams, P., (1992) "Remote Sensing of Snow and Ice," presented at *University of Dundee Remote Sensing Summer School: Remote Sensing and Global Climate Change*, University of Dundee, Scotland, UK, July, 1992.

Wang, Q., and S.P. Gogineni, (1991), "A Numerical Procedure for Recovering Scattering Coefficients from Measurements with Wide-Beam Antennas", *IEEE Trans. on Geoscience and Remote Sensing*, vol. 25, no. 5, pp. 778-783.

Wiesbeck, W., and S. Riegger, (1991), "A Complete Error Model for Free-Space Polarimetric Measurements," *IEEE Transactions on Antennas and Propagation*, vol. 39, no. 8, pp. 1105-1111.

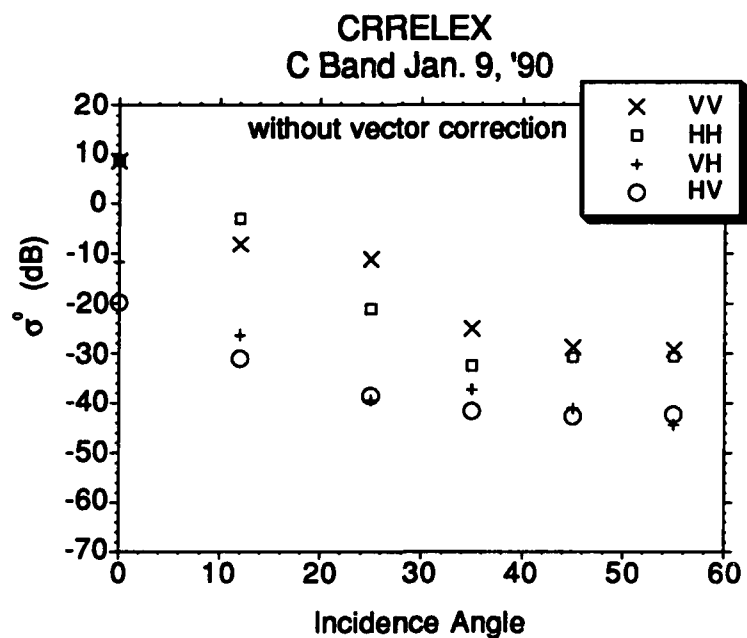
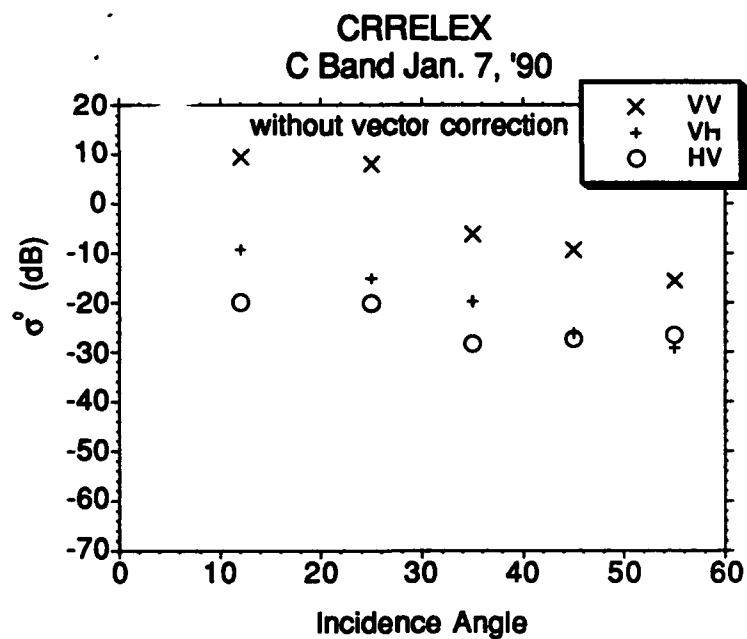
Wu, S.T., and A.K. Fung, (1972), "A Noncoherent Model for Microwave Emmisions and Backscattering from the Sea Surface," *Journal of Geophysics Research*, vol. 77, pp. 5917-5929.

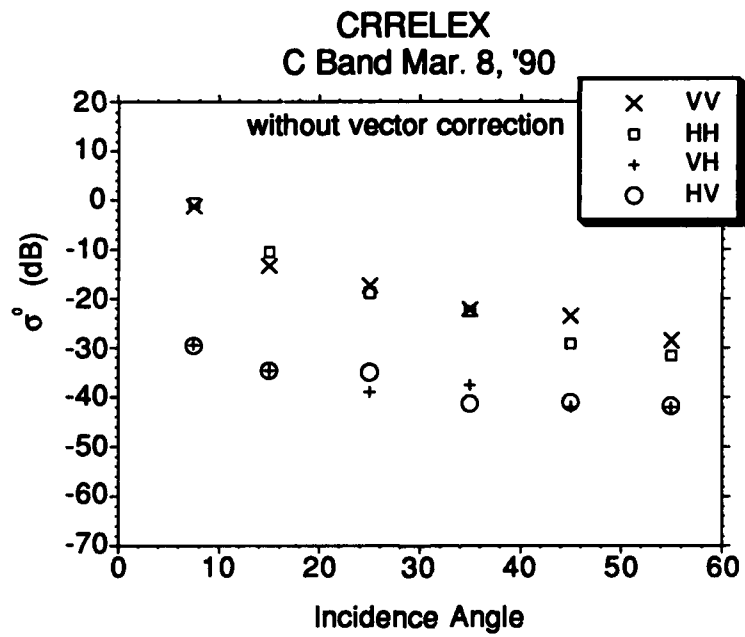
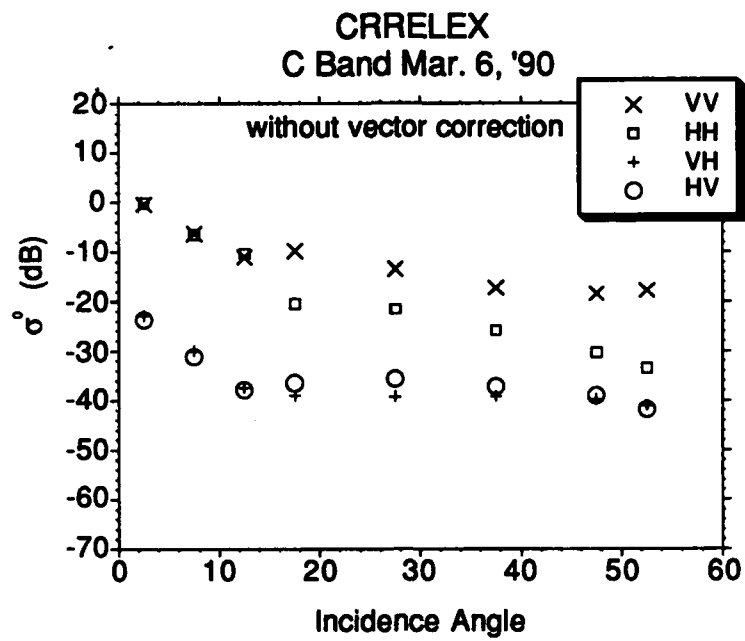
Acknowledgement:

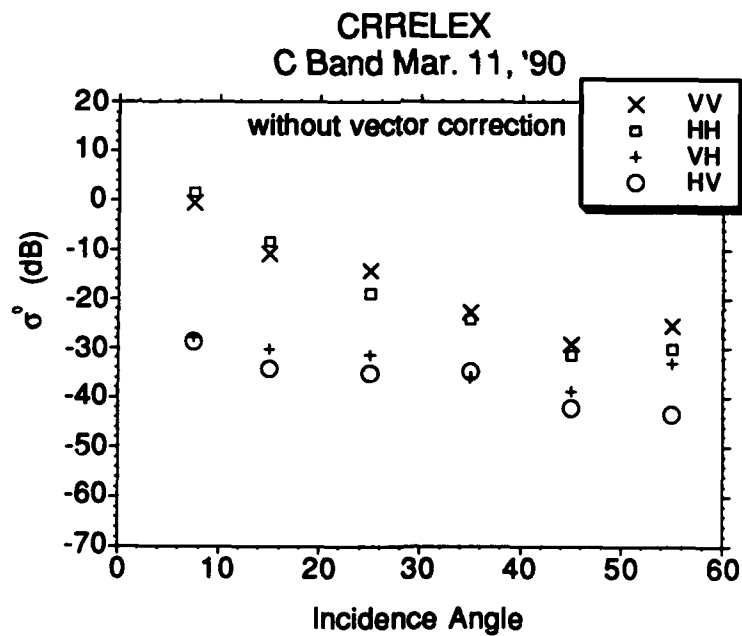
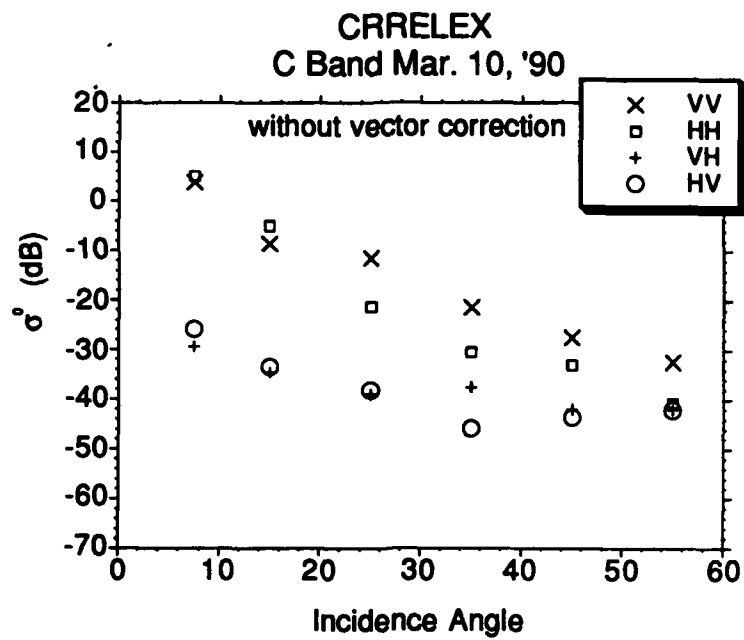
The authors would like to thank Terry Tucker and John Govoni at CRREL for their assistance in the experiment. We'd also like to thank Jim Ronnau and Jeff Young of KU for their participation in the experiment. This work was funded in part by an Office of Naval Research (ONR) doctoral fellowship, as well as ONR grant #N00014-89-J-1456.

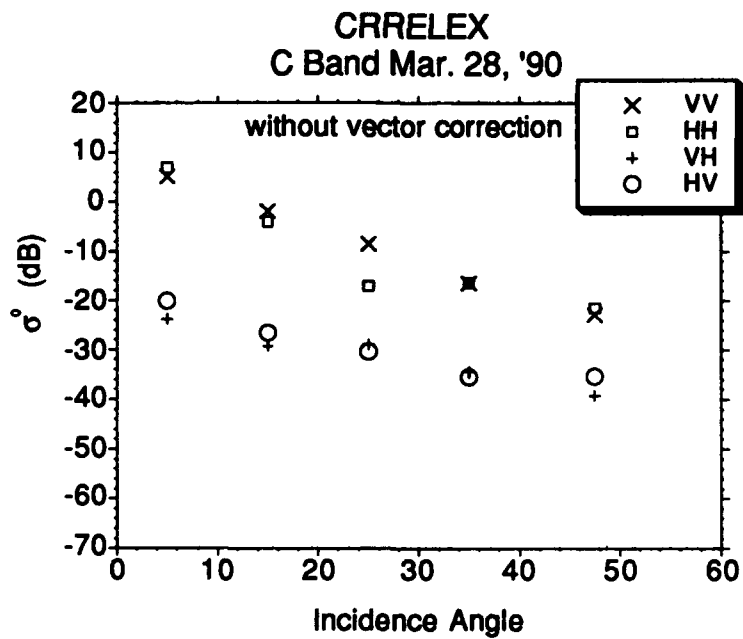
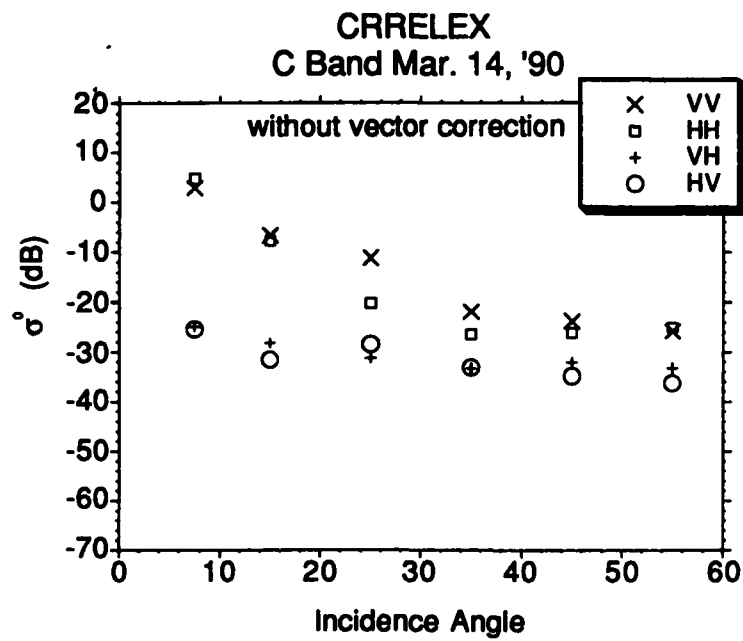
Appendix A

**CRRELEX'90 Scalar calibrated results of scattering from simulated sea ice
without beamwidth correction for both C band and Ku band**

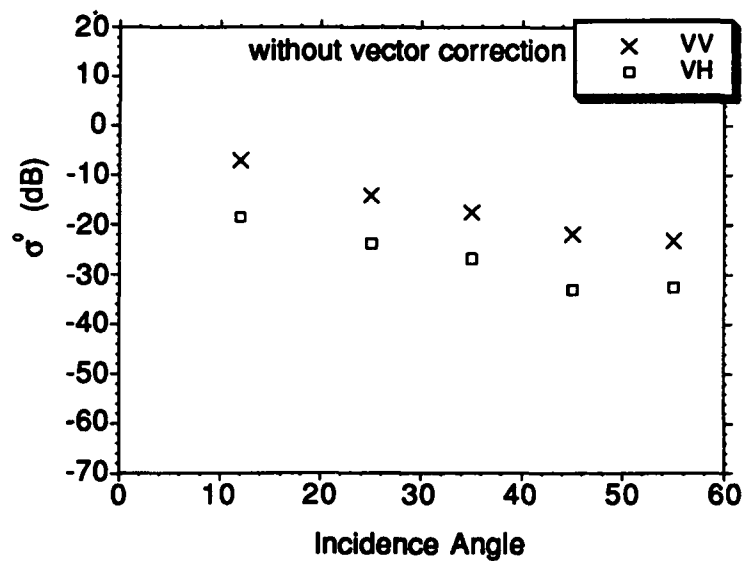




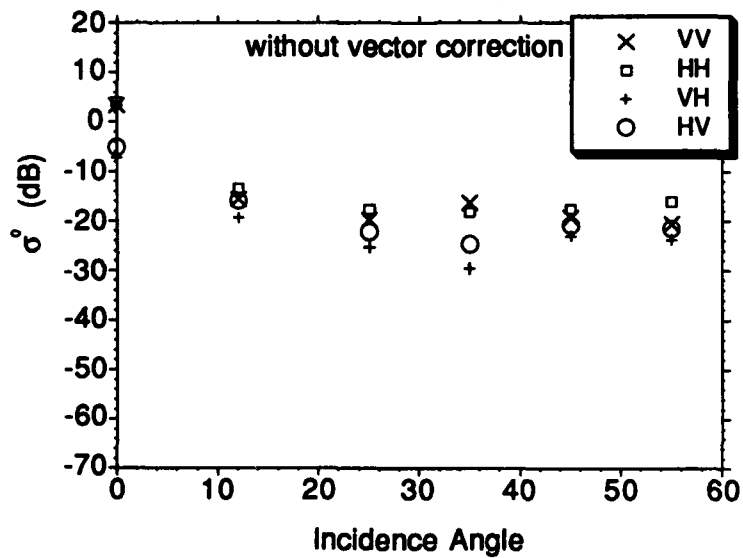




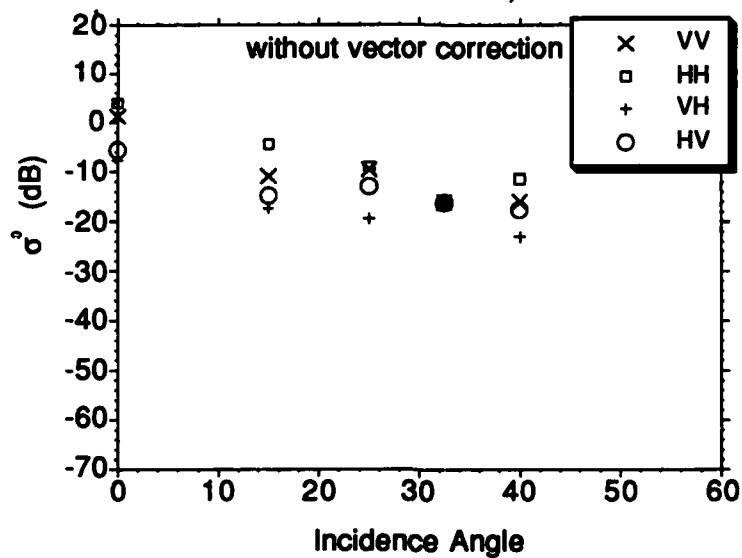
CRRELEX
Ku Band Jan. 7, '90



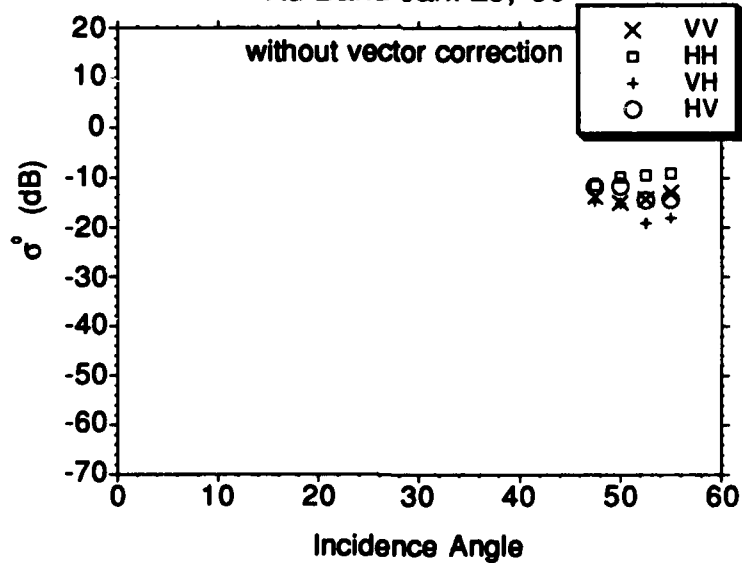
CRRELEX
Ku Band Jan. 9, '90

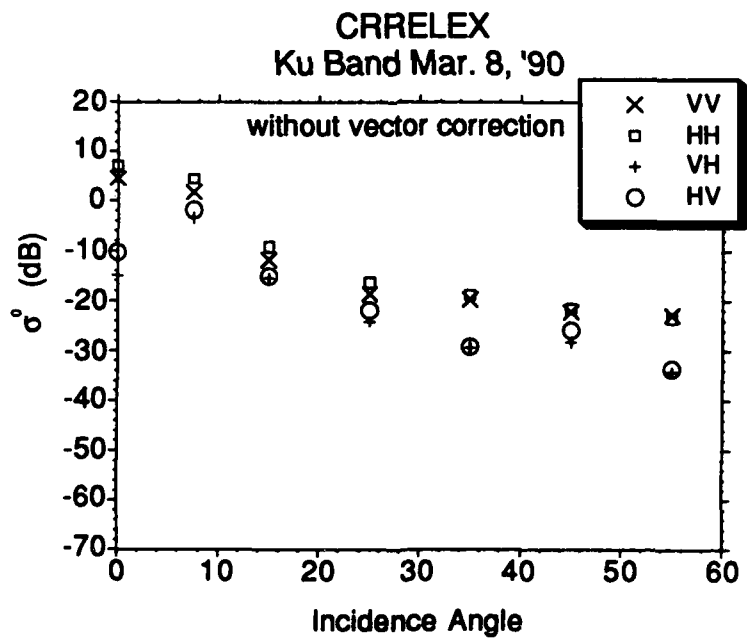
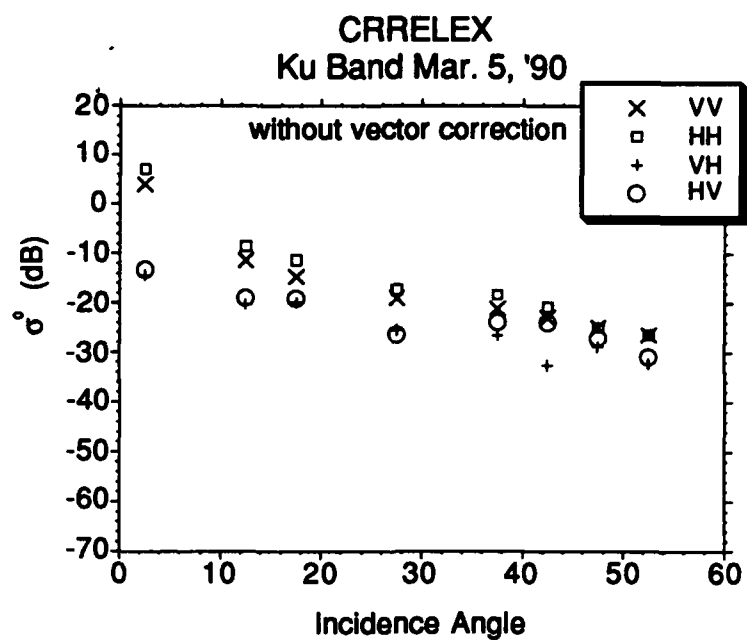


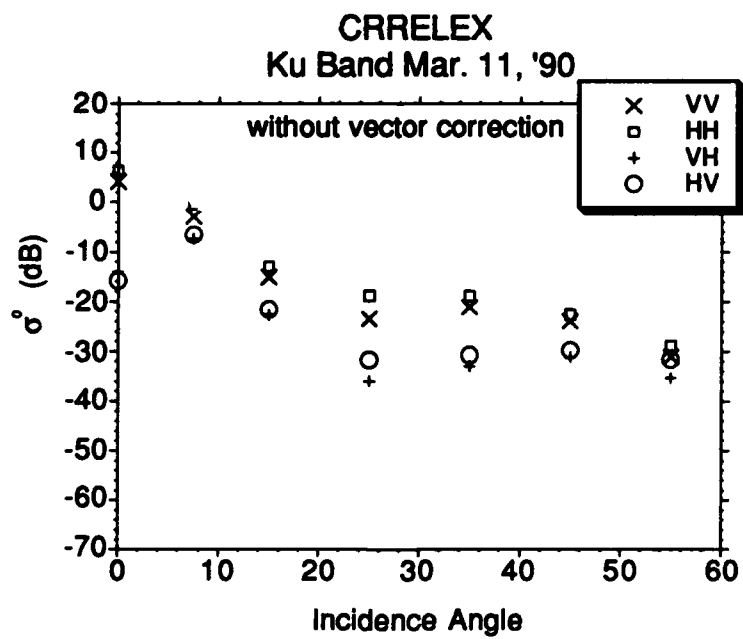
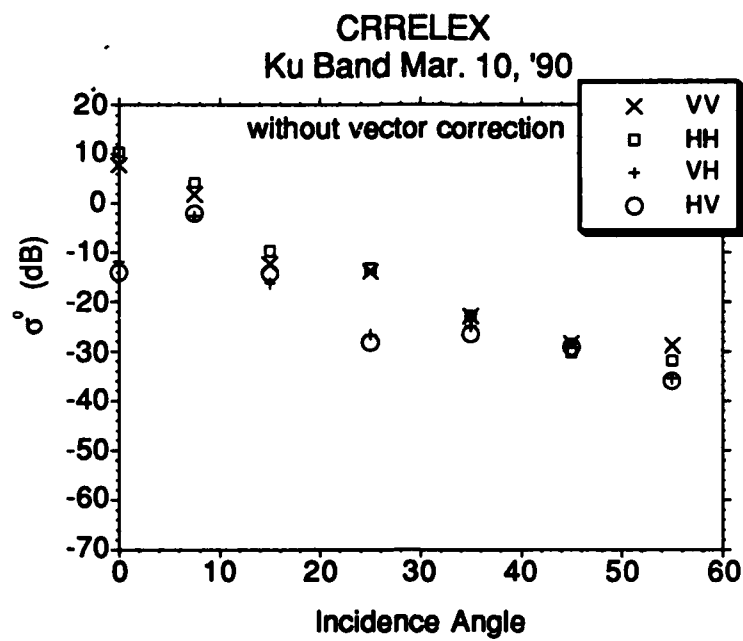
CRRELEX
Ku Band Jan. 24, '90

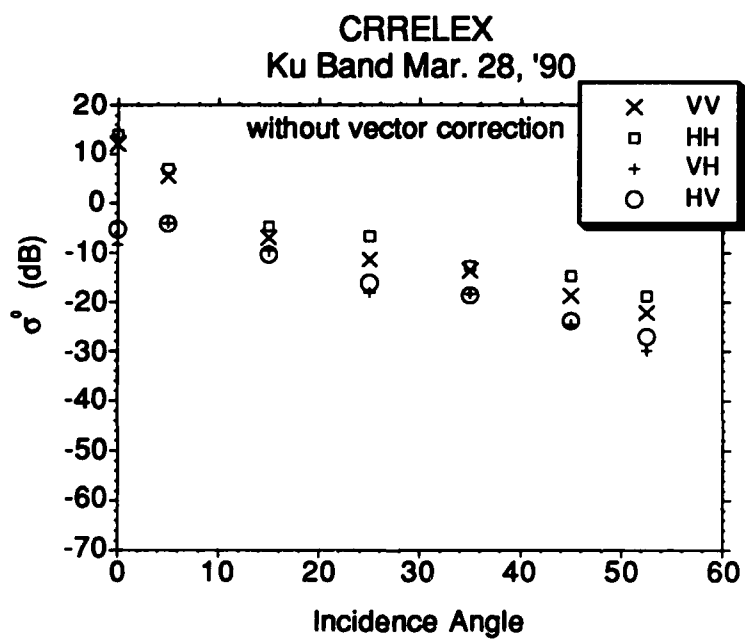
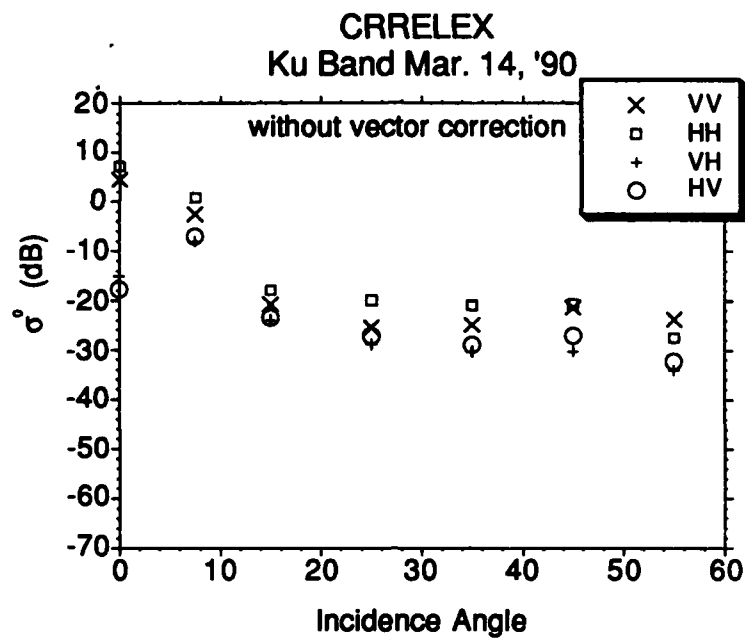


CRRELEX
Ku Band Jan. 29, '90



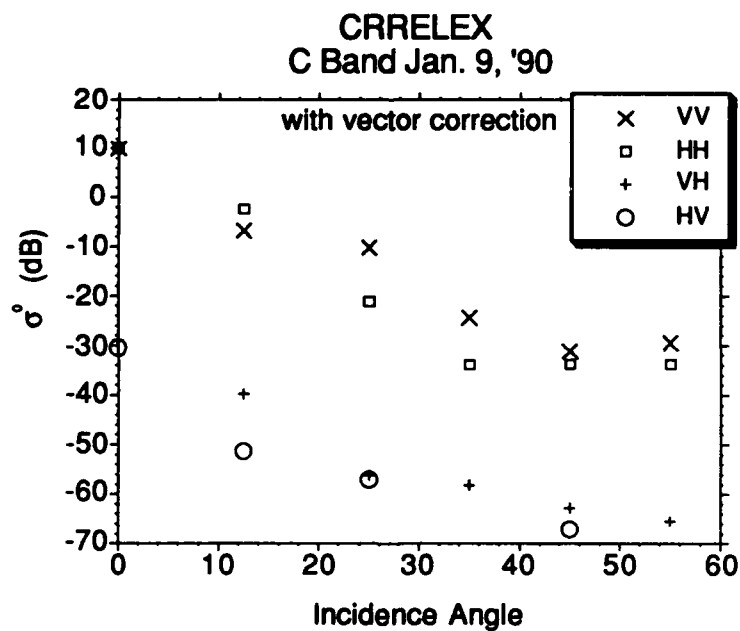
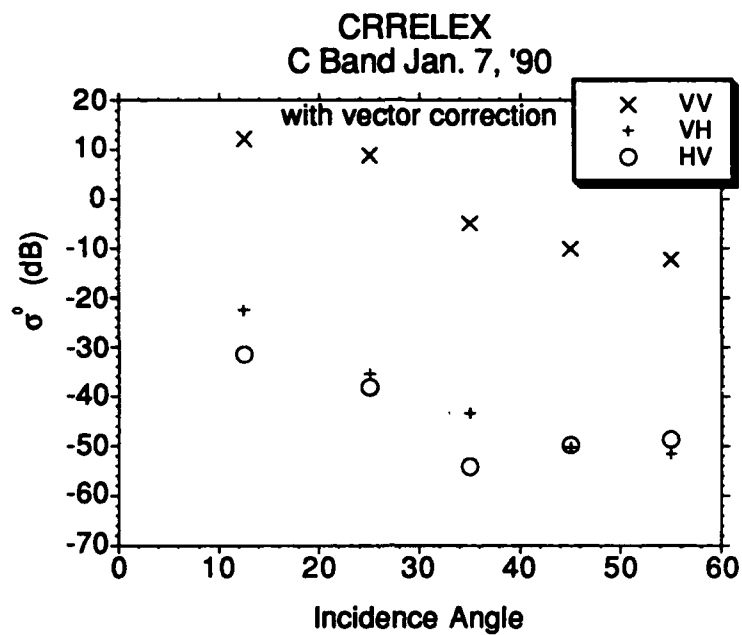


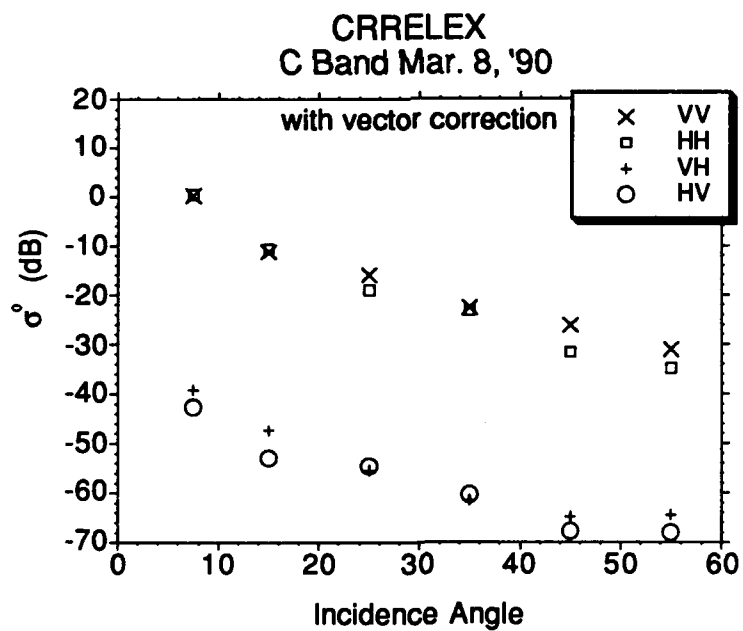
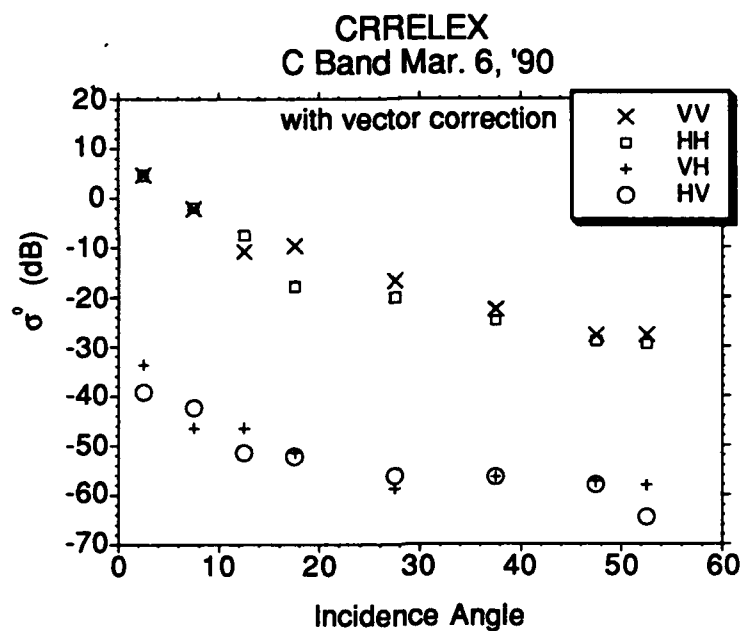


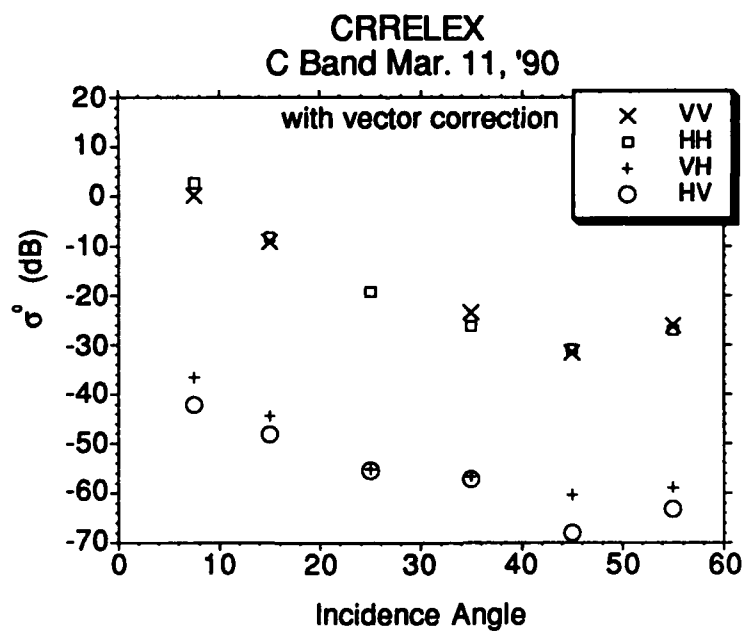
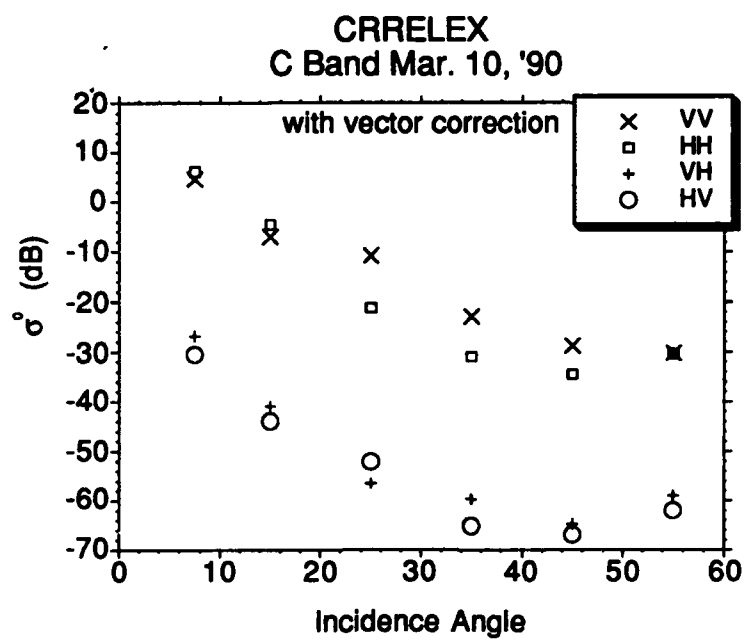


Appendix B

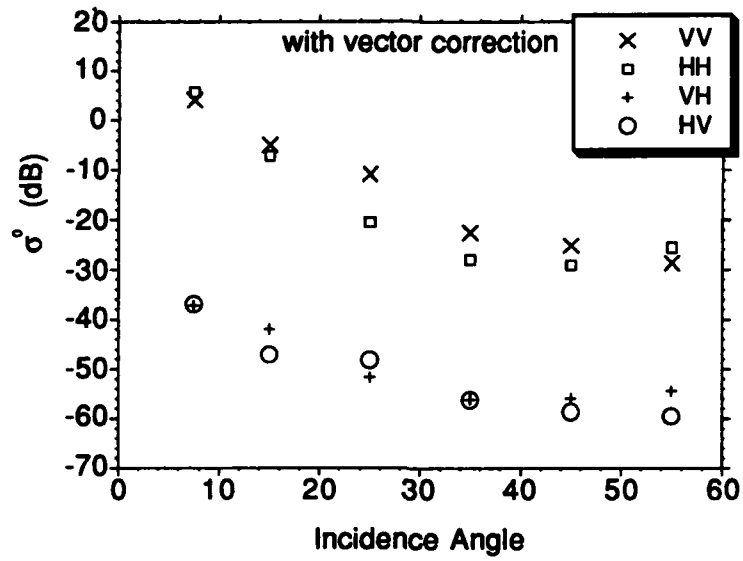
**CRRELEX'90 VECTOR calibrated results of scattering from simulated sea
ice without beamwidth correction for both C band and Ku band**



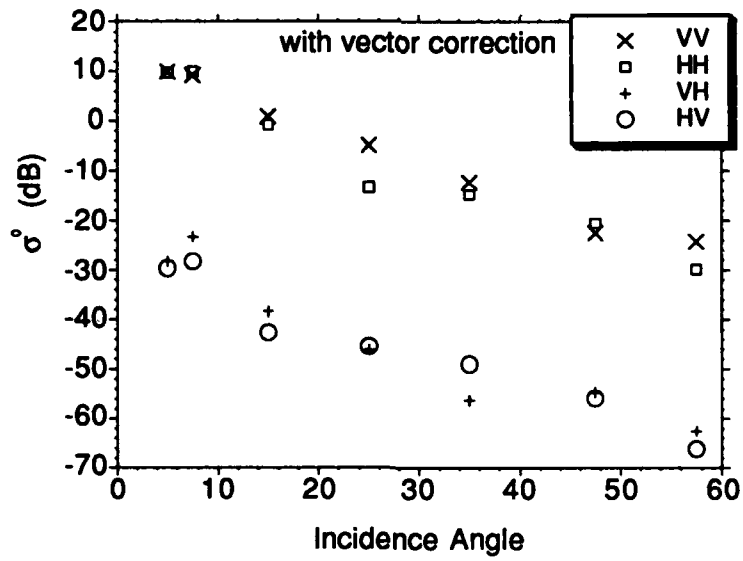


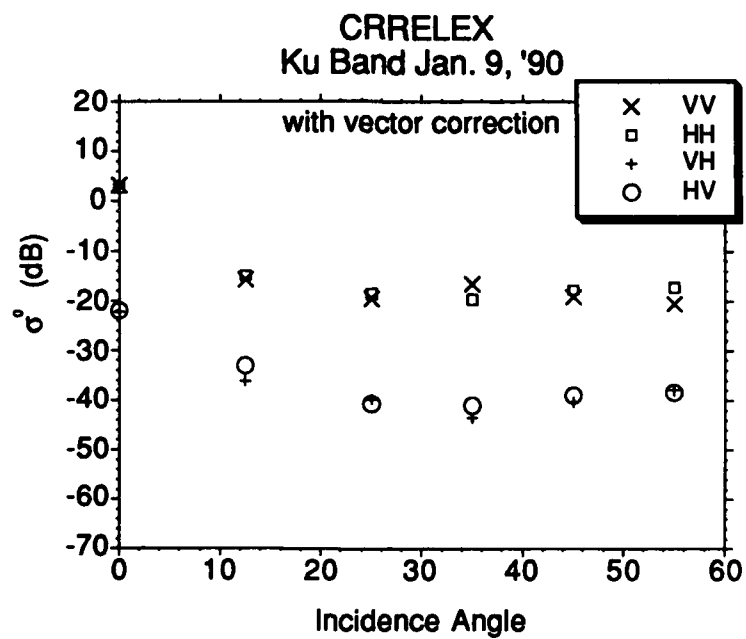
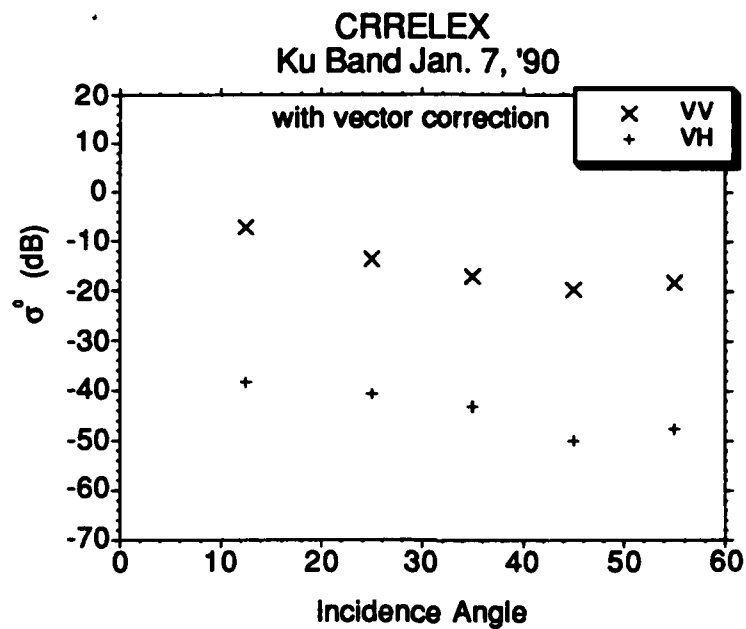


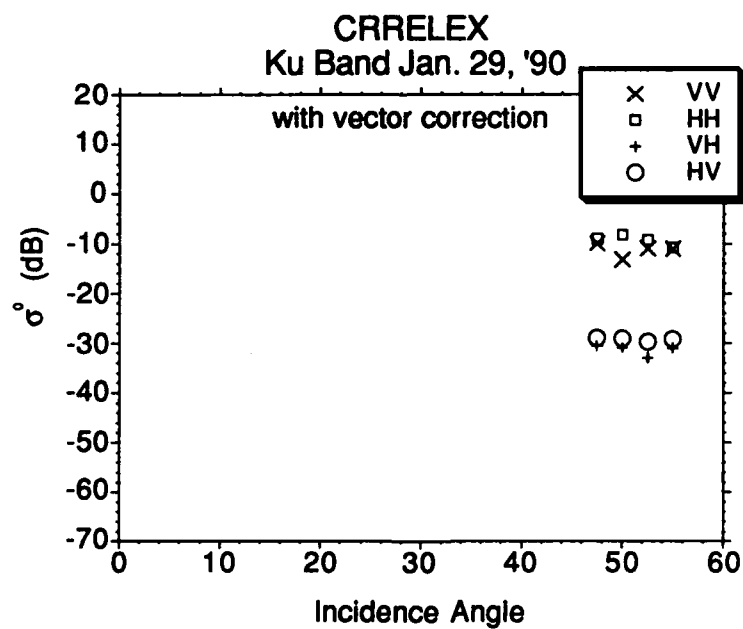
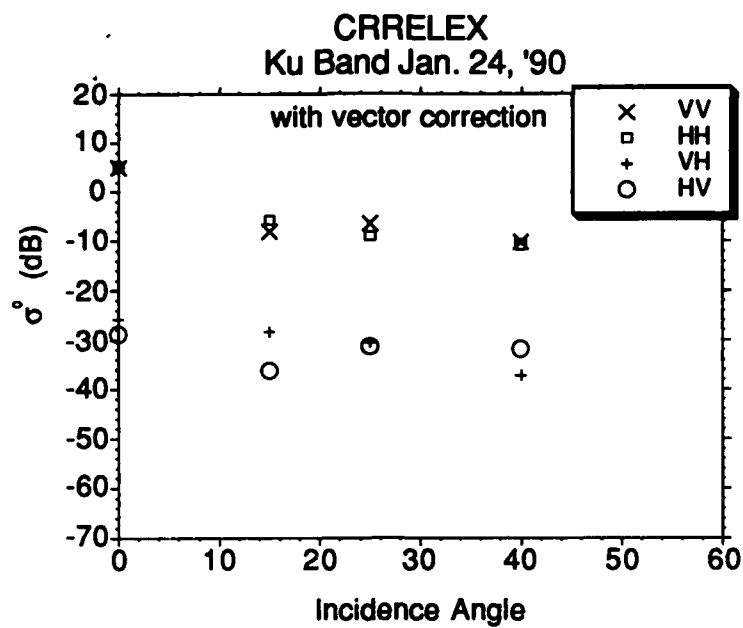
CRRELEX
C Band Mar. 14, '90

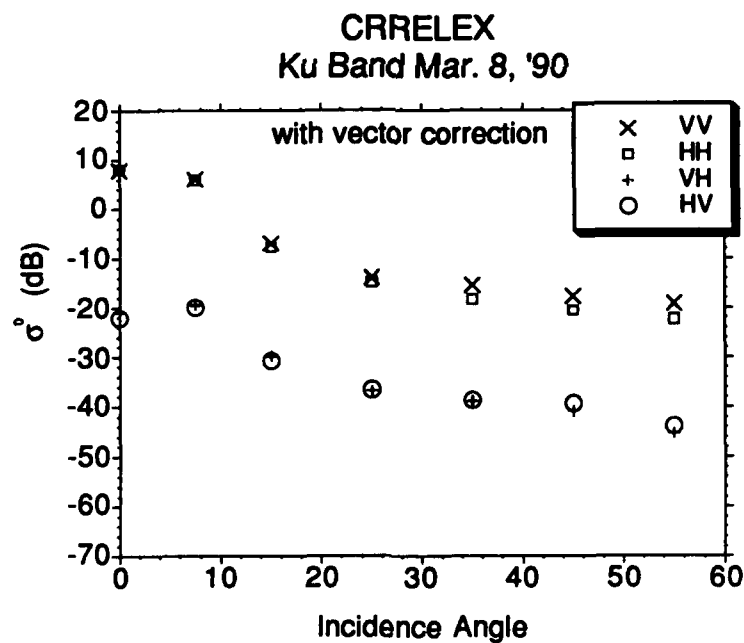
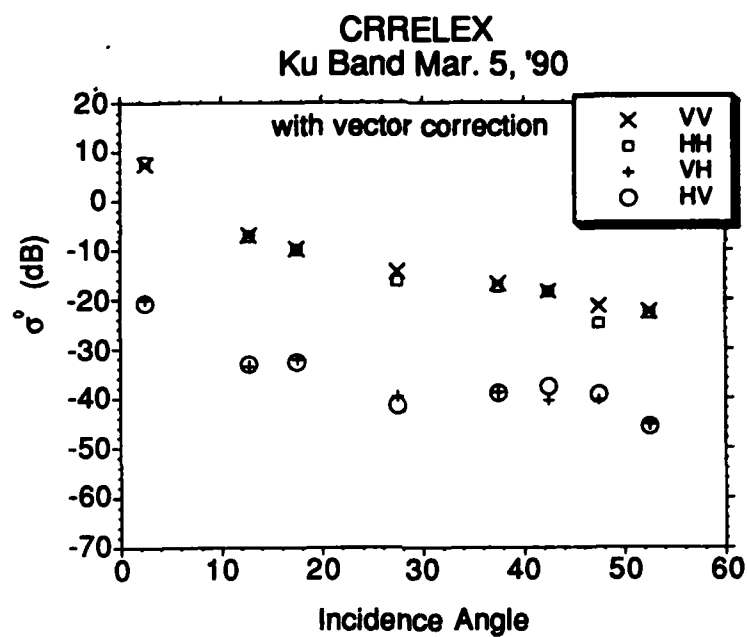


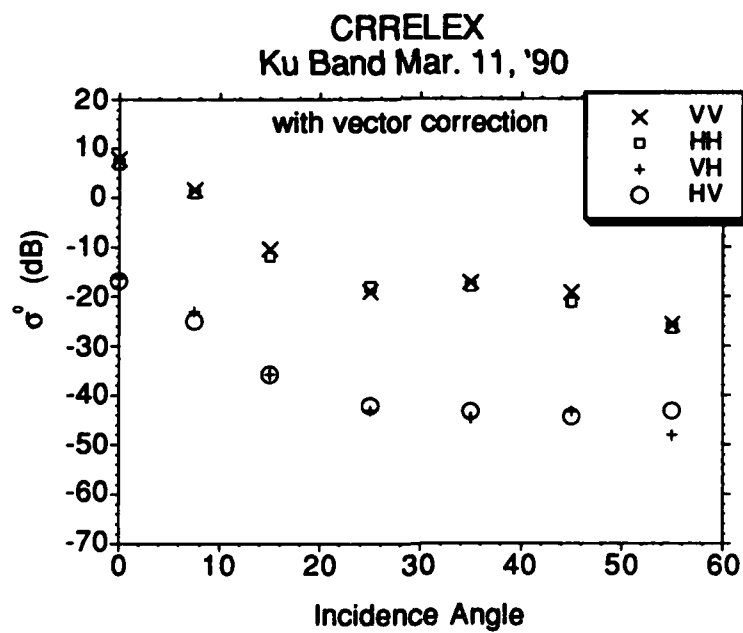
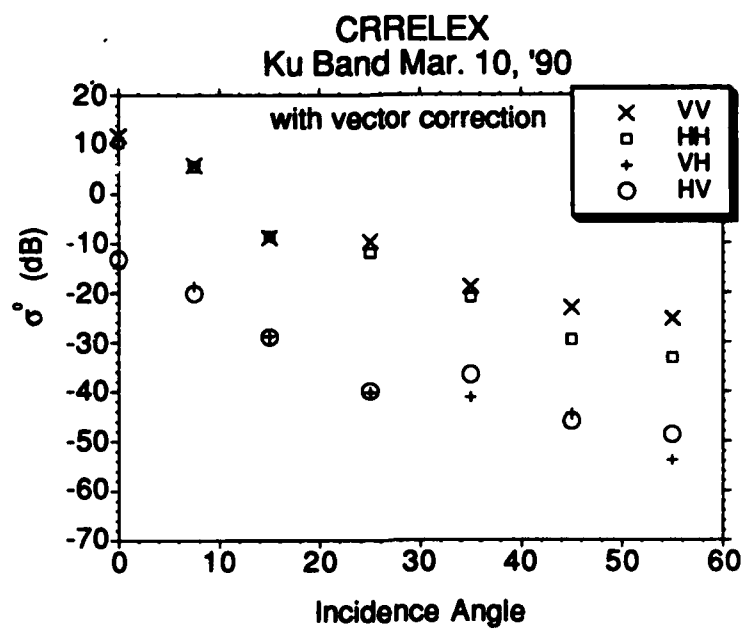
CRRELEX
C Band Mar. 28, '90

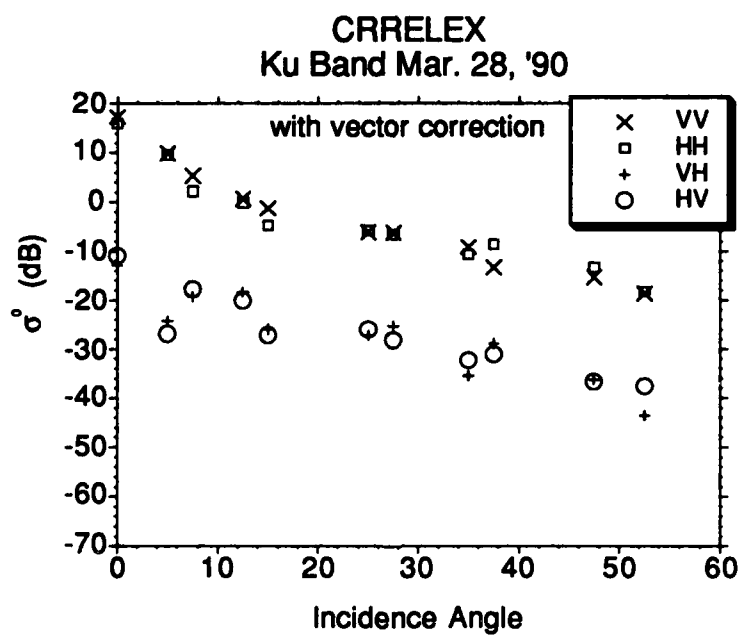
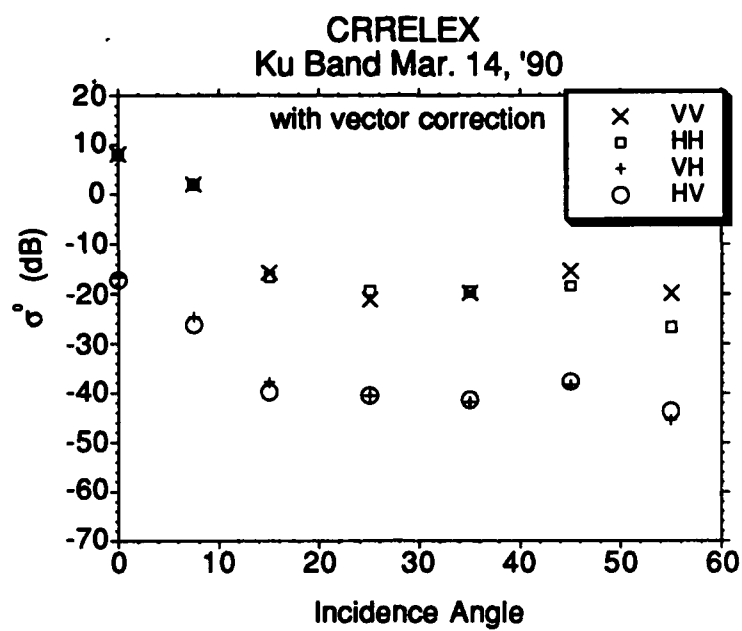






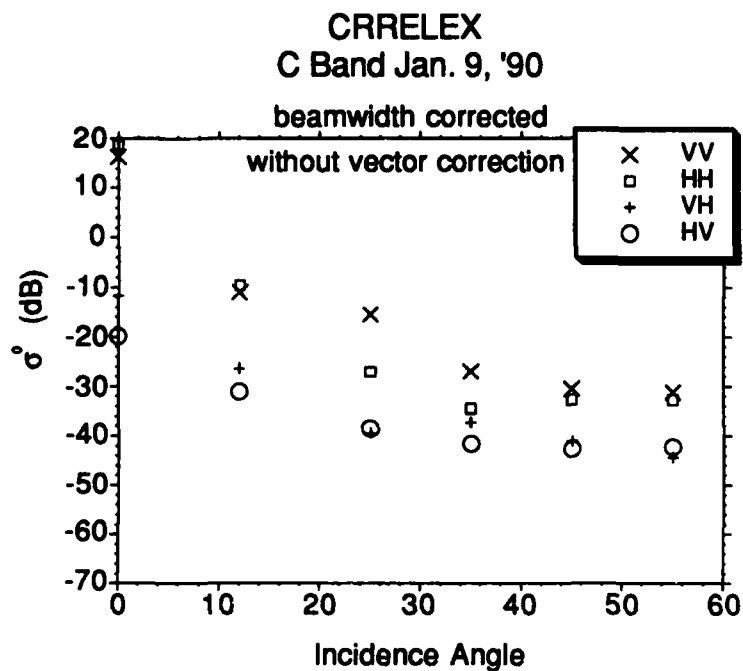
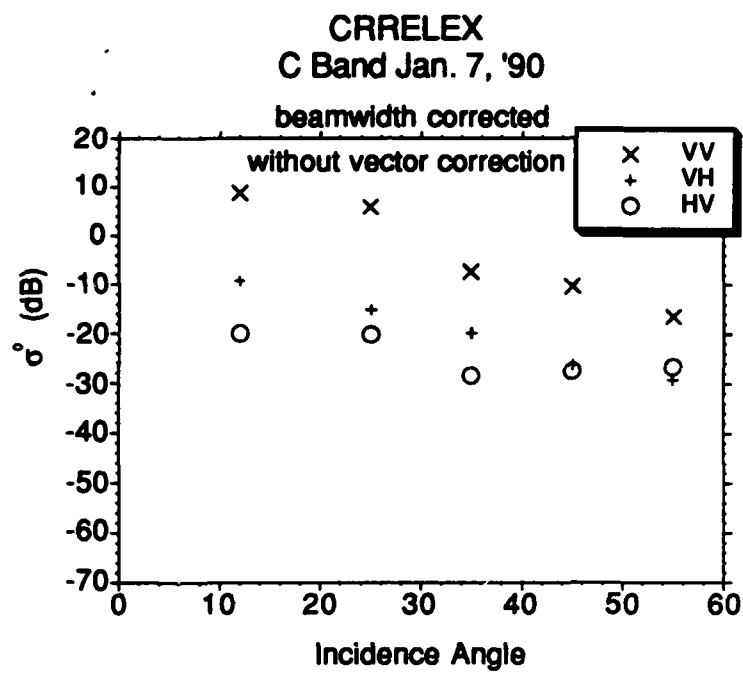




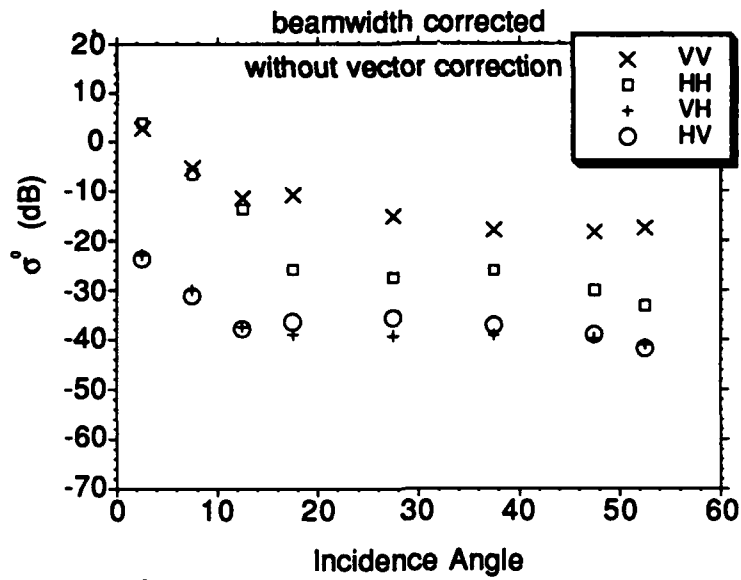


Appendix C

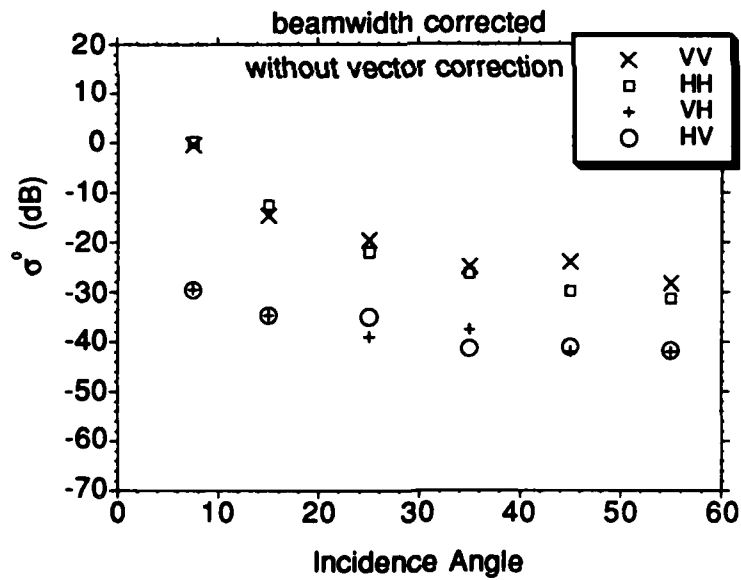
**CRRELEX'90 Scalar calibrated results of scattering from simulated sea ice
with beamwidth correction for both C band and Ku band**

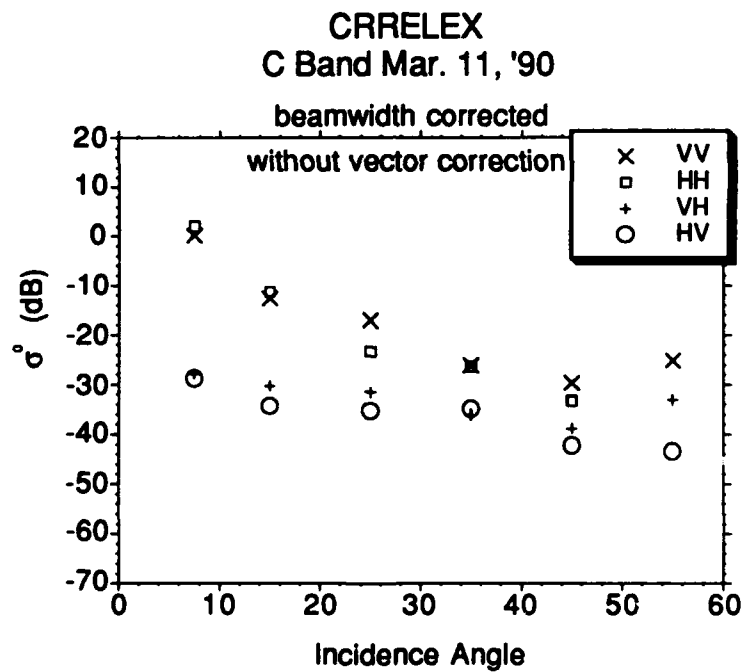
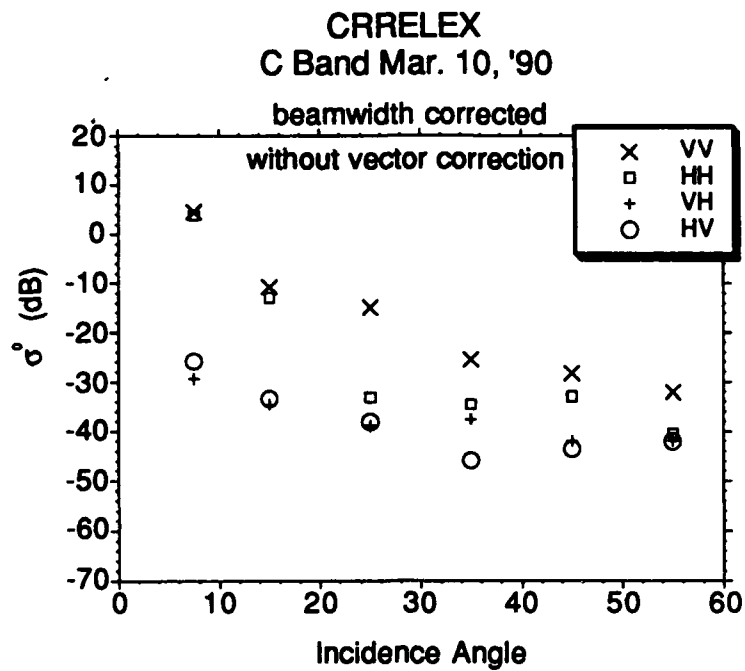


CRRELEX
C Band Mar. 6, '90

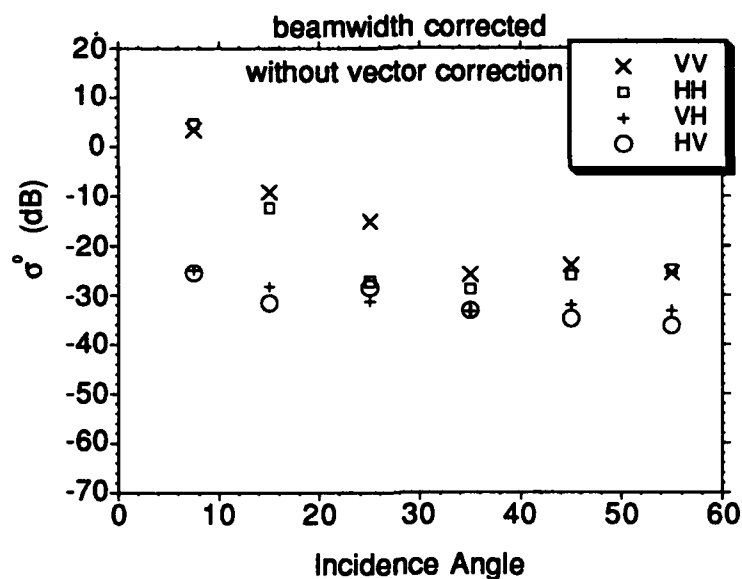


CRRELEX
C Band Mar. 8, '90

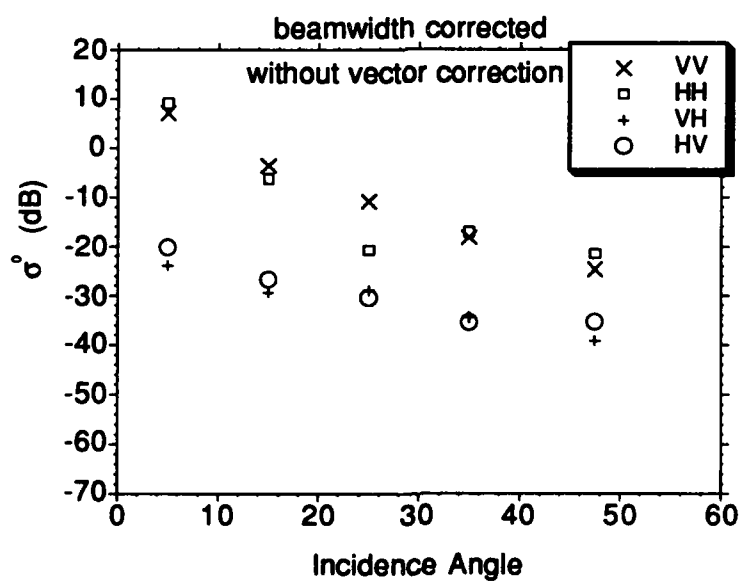




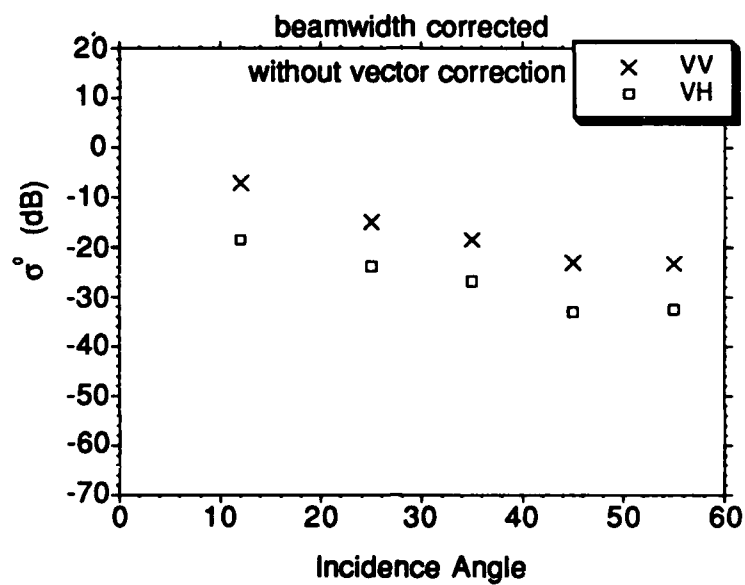
CRRELEX
C Band Mar. 14, '90



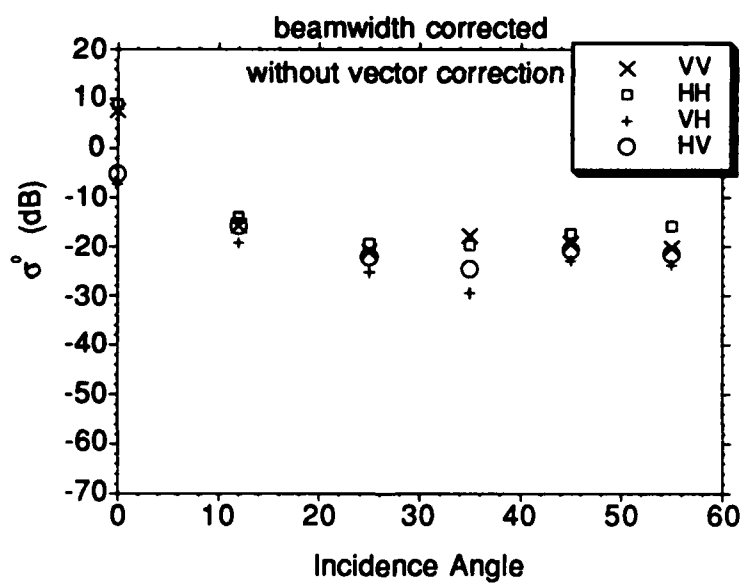
CRRELEX
C Band Mar. 28, '90



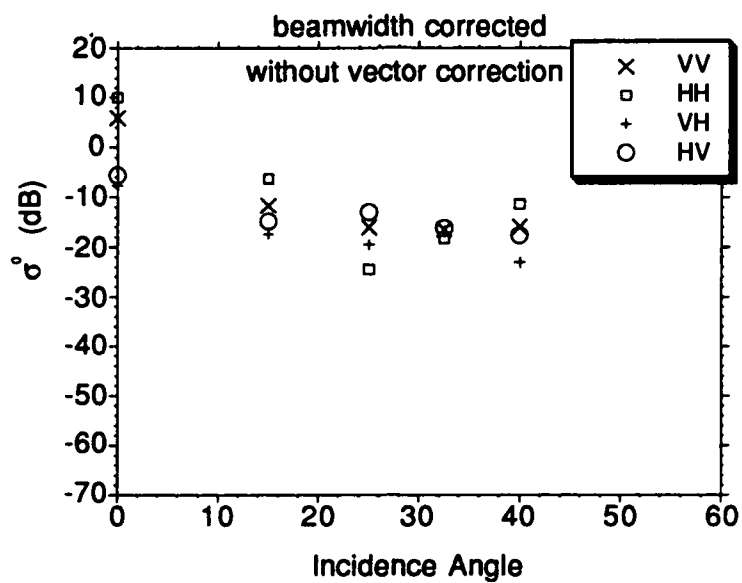
CRRELEX
Ku Band Jan. 7, '90



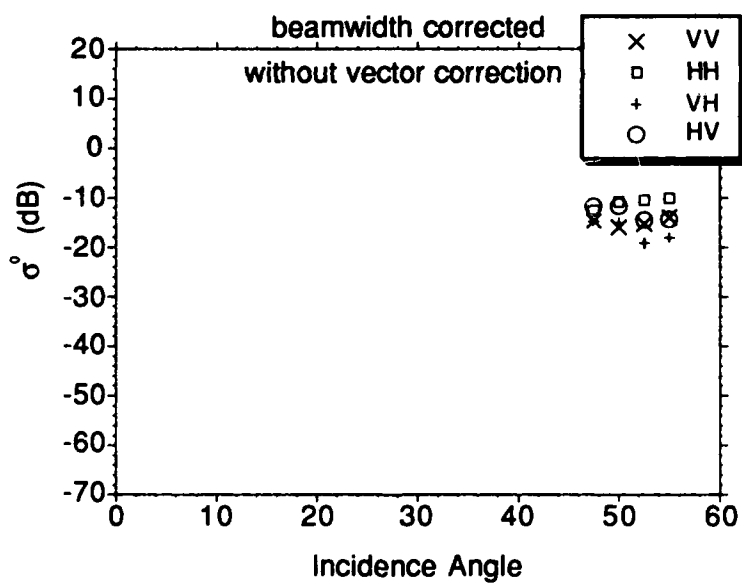
CRRELEX
Ku Band Jan. 9, '90

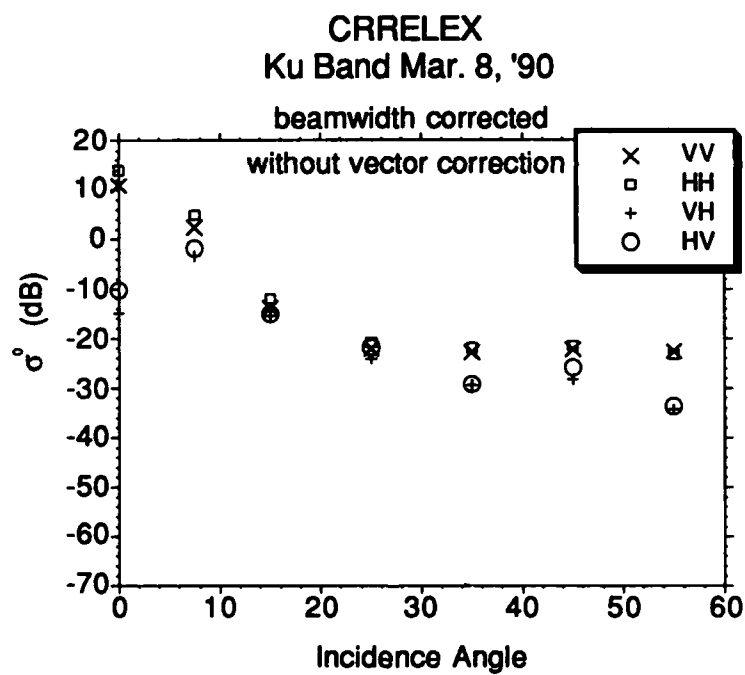
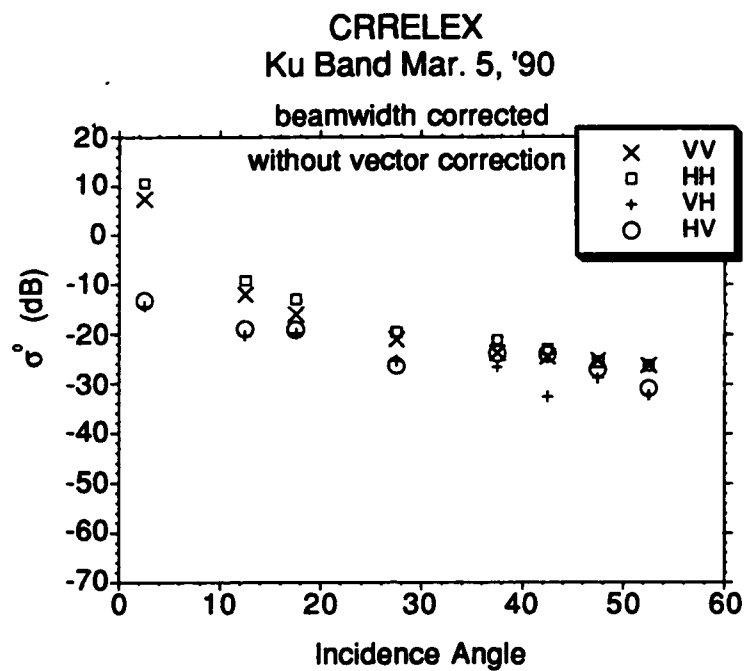


CRRELEX
Ku Band Jan. 24, '90

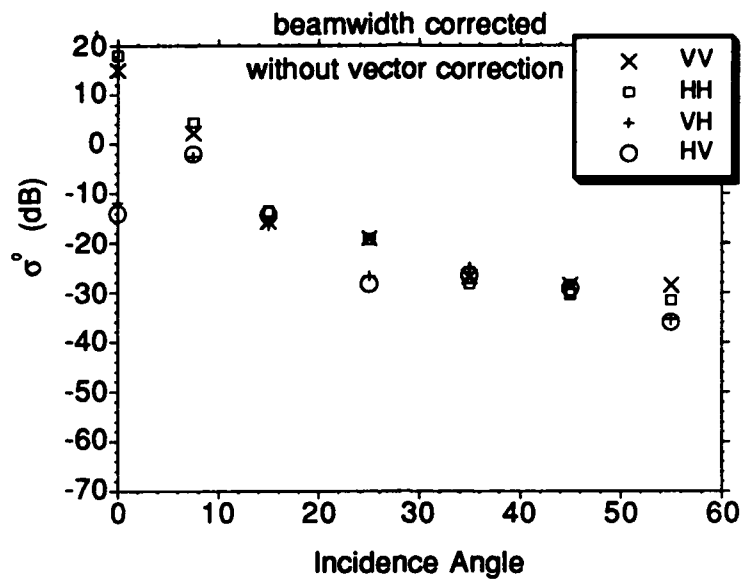


CRRELEX
Ku Band Jan. 29, '90

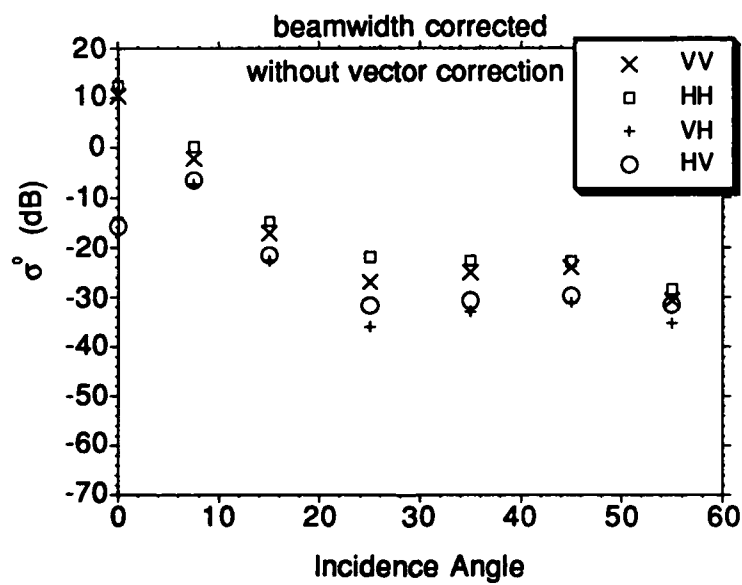




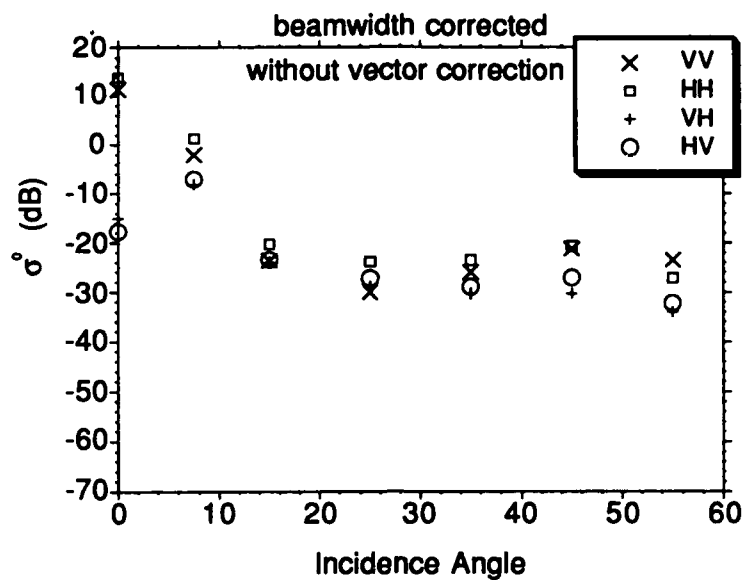
CRRELEX Ku Band Mar. 10, '90



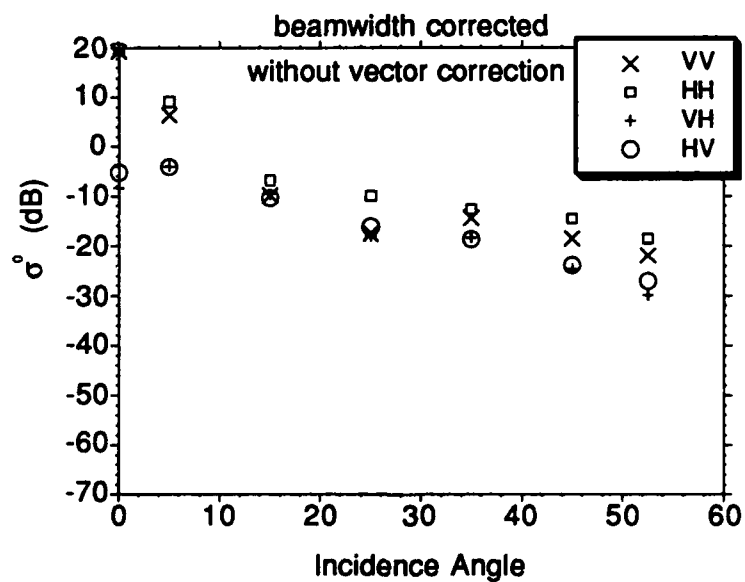
CRRELEX Ku Band Mar. 11, '90



CRRELEX
Ku Band Mar. 14, '90



CRRELEX
Ku Band Mar. 28, '90



Appendix D

**CRRELEX'90 VECTOR calibrated results of scattering from simulated sea
ice with beamwidth correction for both C band and Ku band**

